



THE UNIVERSITY  
*of* ADELAIDE

SCHOOL OF EARTH AND  
ENVIRONMENTAL SCIENCES



# Characterisation of gold mineralisation, Oberon prospect, Tanami region, N.T.

Dennis Meria

1180592

Supervisor  
Nigel J. Cook

Co-supervisor  
Cristiana L. Ciobanu

Centre for Tectonics, Resources and Exploration  
Department of Geology and Geophysics  
School of Earth and Environmental sciences  
University of Adelaide, South Australia  
[dennis.meria@student.adelaide.edu.au](mailto:dennis.meria@student.adelaide.edu.au)

## ABSTRACT

Oberon is a relatively recently discovered gold prospect in the Tanami district approximately 600 km NW of Alice Springs, N.T. Petrographic, mineralogical and mineral chemical analysis of the gold-bearing horizons in drillhole TID0065 has characterised the mineralisation with particular emphasis on gold distribution.

Two mineralised horizons are identified. The 'Upper' zone contains semi-massive pyrite within a characteristic 'Boudin Chert' lithology and adjacent graphite schists. The 'main' mineralisation, towards the bottom of the drillhole, occurs within relatively low-sulphide calcareous turbidites of the 'Puck' sequence. The mineralogy of the gold mineralisation is simple. Arsenopyrite, pyrite and pyrrhotite are the dominant sulphides and occur both within multiple generations of quartz-carbonate veins and as disseminations in adjacent wallrock. There is widespread evidence for late sulphide recrystallization. Gold occurs as native gold. A population of fine-grained gold (1-10 microns) is seen within arsenopyrite, and more rarely in pyrite. 'Exotic' Au-bearing minerals such as Au-(Ag)-tellurides are not present.

Laser-Ablation ICP-MS analysis has established that invisible gold in sulphides plays a negligible role in terms of overall gold balance. 'Residual' gold concentrations in the central parts of arsenopyrite grains are no more than a few ppm; Au concentrations in pyrite are an order of magnitude lower still. There is, however, a marked enrichment in Au concentrations around the margins of arsenopyrite and in areas of intense fracturing and brecciation, with individual LA-ICP-MS spot analyses giving up to several thousand ppm. This enrichment can be readily linked to grain-scale gold remobilisation and reconcentration of lattice-bound gold during sulphide recrystallization. Using high-resolution Focussed Ion Beam – SEM imaging, this gold is revealed to occur as microfracture fillings and as fine particles and nanoparticles. This study is the first to demonstrate the presence of gold nanoparticles in an orogenic gold deposit.

The Oberon deposit is metamorphosed at middle greenschist facies and displays both lithological and structural control. Mineralisation at Oberon shows broad similarities with that at Callie, but also a number of differences. Pyrite chemistry in the 'Upper' mineralisation is subtly different to that in the "Main' mineralised level, leading to the conclusion that the former may represent authigenic (bacterially-mediated?) pyrite that formed in a euxenic or oxygen-starved environment. Such carbon- and iron-rich horizons provide a ready mechanism for gold precipitation from fluid via redox reaction. This contrasts with the clearly hydrothermal sulphide assemblage and associated chlorite alteration in the 'main' mineralised zone.

## INTRODUCTION

The Tanami region, straddling the N.T. – W.A. border, hosts a number of major ore deposits. Despite extensive exploration throughout the gold-prospective stratigraphy of the district, discovery and development and of new resources are hampered by the scarcity of exposed outcrops and isolation of these terranes. Despite extensive exploration, a comprehensive understanding of the geology of the Tanami region is lacking. Investigation of the numerous deposits across the Tanami region has allowed genetic models to be constrained; these have evolved over the last two decades as additional evidence is found.

The most significant discovery in the district, Callie, led to numerous exploration campaigns. The Oberon prospect lies 40km north of the world-class Callie deposits which has an estimated resource of 22.0 Mt @6.1g/t with a total of 188 tonnes gold (6.03 MOz) (Huston *et al.* 2007). The Oberon orebody consists of Au-bearing quartz-K-feldspar-carbonate-pyrite veins with associated chlorite-bearing wallrock alteration zones (Huston *et al.* 2007). Similar to Callie, gold mineralisation at Oberon is predominantly within an axial zone of a pre-existing anticline.

The aim of this project was to investigate the mineralogy and petrography of the gold-bearing lithologies at Oberon, to assess the relationship of gold mineralisation to veining and associated mineralisation and to address the mineralogy of the gold-bearing paragenesis. The aim is to refine a genetic model for Oberon and to compare and contrast the results with observations on gold mineralisation elsewhere in the Tanami orefield. The trace element composition of key minerals such as arsenopyrite and pyrite has also been investigated. The resultant quantitative data provides information of relevance to both exploration models and ore processing. Similarly, compositional data for sulphides such as arsenopyrite and pyrrhotite allows geothermobarometry to be applied, placing additional constraints on the metamorphic history of the deposit and its host rocks. The resultant data allow existing genetic models for Oberon and the Tanami orefield in general, as well as the geological evolution of the district, to be tested and developed further.

The investigation was conducted on drillcore from a single drillhole (TDI0065) that intersects the deep mineralisation at Oberon. Because exploration of the deep mineralisation of the Oberon prospect is still at an early stage, the stratigraphy and lithologies of the rock package deposit hosting the deposit remains poorly defined. Most of the mineralised zones are within lithological units which are very similar to those hosting the Callie deposit, even if they cannot, at present, be directly correlated with one another. The present project, in conjunction with a second project specifically addressing the host rock stratigraphy (Silcock 2011) is thus a valuable contribution to an exploration and genetic model for the Oberon deposit.



## GEOLOGICAL SETTING

### Regional Geology

The Tanami region is situated in northwest central Australia, straddling the N.T. – W.A. border and forms part of the Paleoproterozoic basement of the North Australian Craton (Myers *et al.* 1996). Page *et al.* (1995) infer the basement in the Tanami Region to be Neoproterozoic of age, consisting of granitic gneisses of the Billabong Complex which are extensive at depth. These high metamorphic grade meta-arkose rocks and leucogranites are overlaid by Paleoproterozoic rocks, the oldest known being the Stubbins Formation which yields maximum depositional ages of  $1,870 \pm 6$  Ma and  $1,864 \pm 3$  Ma provided by two SHRIMP U-Pb zircon dates (Bagas *et al.* 2006). The Stubbins Formation is fault-bounded on all margins, resulting in a significant gap in knowledge about its relationship with the remainder of the Tanami region. The Tanami Group is the other Paleoproterozoic sequence in the region. This consists of the Dead Bullock Formation, and the conformably overlying Killi Killi Formation from which it is geochemically distinct (Lambeck *et al.* 2010). The Dead Bullock Formation contains unusual Fe-rich mafic sediments compared to global Paleoproterozoic non-iron rich sediments (Lambeck *et al.* 2008 (Figure 1, 2).

Lambeck *et al.* (2008) have subdivided the basal Dead Bullock Formation into (i) the Ferdies Lower Callie sequence which hosts the majority of gold mineralisation at the Callie deposit and (ii) the overlying Callie Member. The Ferdies Lower Callie sequence consists of feldspathic sandstone commonly interbedded with siltstone fining upwards into graphitic units and banded iron formations of the Callie Member (Lambeck *et al.* 2008). These sequences were deposited between ca. 1860 Ma and 1840 Ma during a time of low sediment input into the Tanami Basin. The overlying Callie Member is a ~600 m-thick sequence which consists of mudstone and carbonaceous siltstone-hemipelagic claystone (Lambeck *et al.* 2008; Bouma 1962) with a depositional age of  $1838 \pm 6$  Ma (Cross & Crispe 2007). Units of iron-rich sedimentary rock are interpreted to have been deposited during a time of low rates of clastic sedimentation (Lambeck *et al.* 2008).

The Killi Killi Formation is the most widely spatially distributed lithostratigraphic unit in the Tanami and northern Arunta regions. Cross & Crispe (2007) reported a maximum depositional age of the Killi Killi Formation between 1870 and 1860 Ma. The formation is composed of turbiditic siliciclastic rocks (micaceous sandstone, lithic sandstone interbedded with siltstones and carbonaceous mudstones). These coarse-grained rocks are geochemically distinct from the turbidite unit, suggesting a marked change in sedimentary source in contrast to the conformably underlying unit Dead Bullock Formation. Lambeck *et al.* (2010) integrated the geochemical data from the Killi Killi Formation to conclude the varied  $\epsilon_{Nd}$  values can be interpreted to indicate deposition in localised basins. The basinward shift in facies and lowstand deposits are interpreted by Lambeck *et al.* (2010) as due to the development of separate rift shoulders with poor mixing among canyon slope systems. Killi Killi Formation deposition ceased prior to the major regional deformational Tanami Event at approximately 1840 Ma to 1825 Ma (Lambeck *et al.* 2008).

Granitic suites intruded the Tanami Group by 1825 Ma to 1790 Ma (Huston *et al.* 2007) and were accompanied by numerous dolerite sills. Although the age constraints of the sills are unclear, foliations are a deformational indicator that can be interpreted to pre-date the major deformational event.

## Local Setting

There is little detailed documentation of the Oberon deposit and its immediate host rocks. Although the Callie deposit has been rigorously investigated over a number of years, there still lies a significant gap in the current knowledge regarding whether these two deposits may be similar or differ with respect to ore distribution, genesis and stratigraphic position. There has been virtually no previous work done on the petrography and structural geology at Oberon, although several workers have written papers which state that Oberon has characteristics that show similarities with Callie. Inferences concerning the stratigraphy have been dependent on whole rock geochemical data (Lambeck *et al.* 2008) in combination with the interpretation of its structural setting given by Wygralak *et al.* (2005). A reassessment of the stratigraphy at Oberon is given by Silcock (2011).

According to Huston *et al.* (2007), a significant proportion of the mineralized rock at Oberon is hosted within the axial zone of a pre-existing (D<sub>2</sub>) anticline. Mineralisation within the Callie deposit also exhibits a strong preference for anticlinal hinges where there is a high-angle intersection between quartz veins and bedding planes (Mernagh *et al.* 2007). Decarbonisation fronts are also exhibited in both the Oberon and Callie orebodies. Resemblances with respect to vein paragenesis, mineralisation and structures at the Oberon prospect and Callie deposit have been repeatedly referred in literature.

Low-grade, near surface mineralisation at Oberon was discovered about ten years ago. Wygralak *et al.* (2001) suggested at the time that the estimated resource of the Oberon prospect was 0.48 Moz Au. A genetic model implied that this mineralisation is located within an extensively folded shallow turbidite sequence belonging to the lower greenschist facies Killi Killi Formation, although the exact position within the stratigraphy remained ill-constrained.

Recently established drilling programs at the Oberon deposit in 2009-2010 led to the discovery of higher-grade mineralisation at depth. The present project addresses mineralisation in the 'Discovery hole'. Ongoing exploration during the progress of this project has allowed Newmont to identify the basis of a new resource. Drilling at Oberon continues with intersections of high-grade gold (commonly also visible gold) within a mineralised zone which lies within the informally named "Puck Group" – or 'ROCK X (Figure 3).

This main mineralised zone is comprised of sandstones, located beneath the turbiditic sequence which continuously grades into an underlying chloritised sequence. The ores are structurally controlled by D<sub>5</sub> structures and are localised in anticlinal closure. Similar to Callie, mineralisation appears to be controlled by the amount of carbon in the host rocks, and the main

ore minerals are arsenopyrite, pyrite and visible gold (Wygralak *et al.* 2001). Samples studied derive from drillhole TID0065.

A schematic drillcore log of the mineralised intervals of the drillhole is shown as Appendix 1, with sample locations marked and key macroscopic fabrics illustrated. An index of all samples is given as Table 1. Sampling strategy is described in more detail below.

## **APPROACH**

Field work was conducted during July 2011 at the Tanami Exploration site and consisted of drillcore logging and sampling of drillhole TID0065. Logging also included compilation of a stratigraphic log across the mineralised intervals, to give a context in terms of lithology and structure for the sampled intervals. Forty-three selected samples were prepared as one-inch polished blocks to be examined by optical microscopy and micro-analytical methods. The objective of the optical work was to ascertain the main mineralogical and petrographic characteristics of the samples. Selected samples were then imaged at high resolution by scanning electron microscopy (SEM). Particular attention was given to gold grains and the associated sulphides. SEM-EDAX analysis aided identification of accessory minerals of interest such as gersdorffite and cobaltite.

Selected samples were then analysed by electron probe microanalysis (EPMA) to obtain quantitative mineral compositional data for selected sulphide species. Laser-ablation inductively-coupled spectroscopy (LA-ICP-MS) was carried out to determine concentrations of trace elements within the sulphides. The LA-ICP-MS work targeted only arsenopyrite and pyrite, since these were considered the most likely hosts for invisible gold. Lastly, limited examination using high-resolution Focussed Ion Beam – Scanning Electron Microscopy (FIB-SEM) was undertaken to obtain finest-scale information on gold mineralogy.

## **Sample Suite**

The Oberon drill hole TID0065 was the only suitable core that could be sampled for analytical work. Previous drilling within the area had been restricted to shallow depths, only extending as deep as the Killi Killi Formation (Madigan beds). A deep diamond drilling campaign was initiated when Oberon was considered to be prospective for deeper-lying gold mineralisation. The first drillhole, however, failed after only 500 m due to mechanical difficulties and did not intersect mineralisation. The second drillhole (TID0065) intersected significant gold mineralization with individual assay results as high as 96.5 g/t over 1 m.

Since all the samples were selected from a single drillcore (TID0065) selection criteria for sampling focussed on identification of key textures and relationships of the sulphides with the associated lithology. The aim was to collect samples that were visibly enriched in sulphides, but irrespective of assayed ore grade. Significant mesoscopic sulphide mineralisation was observed

within two distinct intervals: an upper pyrite-dominant sequence (407-476 m) within fine-grained, graphite-bearing boudin chert; and a lower arsenopyrite-pyrrhotite-pyrite-bearing sequence (>645 m); higher Au assays are reported from this lower sequence. No visible gold was observed in the remaining drillcore that was logged and sampled; visible gold-bearing intersections having been removed prior to the present study.

## **METHODOLOGY**

### **Optical Microscopy**

Polished blocks were observed using a Nikon petrographic microscope in reflected light mode. The microscope was equipped with a digital camera and objectives allowing up to 50X magnification. The aim was to characterise each sample with respect to ore textures, to correlate relationships between sulphides and visible gold grains and document whether textures and relationships between minerals vary with lithology, type of veining or depth in the hole.

### **Scanning Electron Microscopy**

Reflected light microscopy was conducted using a Phillips XL-30 Scanning Electron Microscope (SEM) at Adelaide Microscopy, University of Adelaide. This instrument was equipped with an Energy-Dispersive X-ray Spectrometer (EDAX) and a Back-Scattered Electron (BSE) detector. The SEM was operated at an accelerating voltage of 20 eV. BSE imaging coupled with semi-quantitative EDAX analysis allowed the identification of trace minerals within sulphides and other minerals down to the microscale (1-2 micron).

### **Electron Microprobe Analysis**

Twelve samples were selected for quantitative compositional analysis using the CAMECA SX-51 electron microprobe (EPMA) at Adelaide Microscopy, University of Adelaide. The instrument is equipped with wavelength dispersion spectrometers which enabled quantitative compositional data to be obtained for arsenopyrite, pyrite, pyrrhotite, sphalerite, galena and gold/electrum. An acceleration voltage of 20 kV was used with a beam current of 19.5 nA. The following X-ray lines and standards were used: Au (Au M $\alpha$ ), Bi<sub>2</sub>Se<sub>3</sub> (Bi M $\alpha$ , Se L $\alpha$ ), PbS (Pb M $\alpha$ ), Ag<sub>2</sub>Te (Ag L $\alpha$ , Te L $\alpha$ ), Sb<sub>2</sub>S<sub>3</sub> (Sb L $\alpha$ ), CoAsS (Co K $\alpha$ , As L $\alpha$ ), Ni (Ni K $\alpha$ ), CuFeS<sub>2</sub> (Cu K $\alpha$ ), HgS (Hg M $\alpha$ ) and FeS<sub>2</sub> (Fe K $\alpha$ , S K $\alpha$ ). The minimum detection limits and count times are given as footnotes in the respective result tables.



## Laser Ablation Inductively Coupled Mass Spectrometry

LA-ICP-MS analysis of pyrite and arsenopyrite was made using the Agilent HP-7500 Quadupole ICPMS instrument at Adelaide Microscopy. This instrument is equipped with a rapid performance New Wave UP-213 Nd:YAG laser ablation system equipped with MeoLaser 213 software and a He collision cell for removal of matrix interferences. Glitter software (<http://www.glitter-gemoc.com/>) was used for data reduction.

A total of 159 spots from fourteen samples were ablated. Each sample had been inspected by SEM inspection prior to ablation to avoid inclusions or textures that may hinder the quality of the trace element data. The laser system was operated at constant 5 Hz pulse rates and 75% power level; laser energy was typically 5-6 J cm<sup>-2</sup> with a provided ablation rate of approximately 1.5 µm/sec. Pre defined areas of the polished blocks were ablated, with a spot size diameter of 30 µm.

Calibration was performed using an in-house USGS sulphide standard MASS-1. This is a sulphide matrix, trace element-doped precipitated powder fused to a glass disc that has specially developed for trace element analysis of sulphides with an analytical accuracy above 20% (Wilson *et al.* 2002). The monitored isotopes are as follows: <sup>23</sup>Na, <sup>29</sup>Si, <sup>33</sup>S, <sup>34</sup>S, <sup>43</sup>Ca, <sup>51</sup>V, <sup>52</sup>Cr, <sup>55</sup>Mn, <sup>57</sup>Fe, <sup>59</sup>Co, <sup>60</sup>Ni, <sup>65</sup>Cu, <sup>66</sup>Zn, <sup>69</sup>Ga, <sup>75</sup>As, <sup>82</sup>Se, <sup>95</sup>Mo, <sup>107</sup>Ag, <sup>111</sup>Cd, <sup>115</sup>In, <sup>118</sup>Sn, <sup>121</sup>Sb, <sup>125</sup>Te, <sup>137</sup>Ba, <sup>184</sup>W, <sup>193</sup>Ir, <sup>197</sup>Au, <sup>202</sup>Hg, <sup>205</sup>Tl, <sup>208</sup>Pb, <sup>209</sup>Bi. Analysis time for each sample was 90 s, comprising a 30 s measurement of background with laser off, and 60 s second analysis with laser-on. Data reduction was undertaken using Fe as the internal standard. The raw analytical data in each spot analysis is plotted as a time-resolved depth spectrum and the integration times for back and sample signal selected. Standards were run before and after each set of spots on a given sample. To account for the error cause by the instrument drift the counts are corrected and converted to concentration values using known values of Fe in the analysed mineral.

## Dual Focused Ion Beam – Scanning electron Microscopy (FIB-SEM)

FIB-SEM methods were used for high-resolution cross-section imaging of sub-micron-sized gold particles in arsenopyrite. A FEI-Helios nanoLab DualBeam system at Adelaide Microscopy was used, following the methodology described by Ciobanu *et al.* (2011). Standard operating conditions are 30kV for ion milling and 20kV and 5kV for normal and immersion mode imaging, respectively, using the electron beam.

## RESULTS

### Mineralogy and Petrography

#### LITHOLOGY AND DISTRIBUTION OF ORE MINERALS

As introduced above, the stratigraphy of the Oberon drill core has been re-assessed. A simplified stratigraphic column representing the distribution of the ore minerals is given below. The samples suite consists of 43 polished blocks from drillhole TID0065 Oberon. This project has aims to present various types of microanalytical data in order to establish the character of, and differences among the ore minerals with special emphasis on gold behaviour and distribution.

Ores in the Callie deposit have been recognised to be positioned within a stratigraphic unit called the Blake Beds. The anticlinal closure that hosts economic mineralisation within the Blake Beds contains folds, forming the Callie and Lantin anticlines, with mineralisation occurring within the Wilson Shoot and Lantin West Shoot respectively. Gold mineralisation at Dead Bullock Soak (DBS) occurs in two distinct types: Callie-style and Villa-style. Callie-style mineralisation is characterised by coarse and readily visible gold occurring in quartz veins, whereas Villa-style mineralisation is associated with sulphides and is generally fine-grained.

Similar alteration assemblages were seen at Oberon, with widespread chlorite alteration in the mineralised part of the rock sequence. Other visible alteration features included a later calcite alteration evident from calcite veining at the margins of vein quartz; calcite 'pods' are also commonly seen (Figure 5B). Chlorite alteration was more extensive within the lower sequence of the drillcore with most mineralisation occurring within variations of the Puck Group sequence. Variations within the sequence were recognised from the compositions of the whole rock geochemical data, with minor visual differences from the core itself. The 'Puck Group' was subsequently differentiated into two groups (Silcock 2011), with a sandstone unit which was less chlorite-altered grading into an underlying 'grey siltstone' unit with the highest degree of chlorite alteration.

The TID0065 drillcore is 898 m in length. Vein quartz is a dominant feature throughout the main mineralised zone (~675 - 800 m) and is seen within a variety of lithologies. The deep lower sequence (>800 m) consisted of vein quartz networks crosscutting the dolomitic mudstone with chlorite alteration (Figure 4B). Whole rock geochemical data recognised this as the Ca-rich segment of the 'Puck unit'. Heavily reworked veins were predominantly composed of clastic quartz interlayered with fine- and coarse-grained matrices. Carbonaceous veins were prominent, crosscutting vein quartz and along micro-shears within the matrix.

The carbonaceous dolomitic mudstone unit hosts quartz veins with sizes from <5 mm to 30 cm in width, frequently exhibiting crosscutting textures. Vein fabric consistently changes from elongate grains (<2 mm across) to anhedral ~10 mm-sized pods of carbonate minerals. Pyrite is commonly present within microfractures and at the selvages of vein quartz. The majority of arsenopyrite grains display idiomorphic textures within the vein quartz and are often seen straddling the selvege and extending into the fine-grained matrix (Figure 5E). This suggests substantial (re-)crystallisation of arsenopyrite after veining. Arsenopyrite varies in size from <1 mm to as much as 5 mm. Arsenopyrite is generally more prominent than pyrite throughout the deeper sequences. Below 600 m, arsenopyrite is markedly brecciated idomorphic textures, as well as idiomorphic growth within veins and disseminations. Chloritic alteration is evident as alteration haloes surrounding many pervasive quartz veins (Figure 5E).

Clots of sulphides containing elongate crystals of arsenopyrite often crosscut early vein quartz and microshears. A “splaying effect” of arsenopyrite is relatively common, with disseminated crystals developed from the edges of reworked vein quartz into the fine-grained matrix. A heavily deformed and crenulated rock (~714 m) is observed to contain pyrrhotite within vein quartz. There was little variation in the size of these pyrrhotite-dominant veins (typically 1-2 mm-thick) (Figure 5F). In such veins, arsenopyrite is common but pyrite is rare. They may represent a latest generation of sulphide-bearing veins relating to sulphide remobilisation during the waning stages of metamorphism.

Overlying the sedimentary ‘Puck’ sequence is a sandstone unit with chlorite alteration that grades downwards (Appendix 1). The unit is coarse-grained with large clastic quartz grains. Arsenopyrite and pyrite are abundant within this sequence (~670m – 615m); much of the macroscopic pyrrhotite observed is also confined within this unit.

A turbidite sequence lies above the sandstone unit and consists of interlayered fine- and coarse grained material. The overlying sandstone unit can be inferred to be part of the turbidite sequence. Crosscutting carbonate-quartz veining is present; some veins contain calcite pods (Figure 4A). Ore minerals are rare in this unit, even where crosscut by later vein quartz. A coarse-grained sandstone unit lies above a major fault where no ore minerals were observed.

The Boudin Chert unit consisted of brittle and heavily deformed rock containing diagenic, boudinaged quartz ranging between 20-40 mm in size (Figure 5C). These cherty rocks are interlayered with graphite-rich beds. Pyrite is very abundant, occurring as veins, filling microshears and within laminated bands (Figure 5D). Idiomorphic crystals of pyrite are however seldom seen. Minor chalcopyrite is also present in this ‘Upper’ mineralisation but arsenopyrite is absent. No ore minerals are seen higher up in the sequence than the Boudin Chert, which is considered as representing sedimentation in a euxinic or reduced-oxygen depositional environment. The pyrite in this unit may be authigenic and possibly biologically-mediated rather than hydrothermal.

Gold mineralisation is predominantly hosted within the Puck Group, fine-grained rocks containing the assemblage chlorite-muscovite-quartz-dolomite-feldspars-rutile  $\pm$  ilmenite. Local faults which post-date alteration and gold mineralisation represent the last stage of deformation. The Fe-rich phyllite zones host majority of the gold in contrast to the Ca-rich layers. This is confirmed from analysis through this study which coincides with previous studies done by workers.

## COMMON SULPHIDES

The dominant ore minerals are pyrite ( $\text{FeS}_2$ ), arsenopyrite (ideally  $\text{FeAsS}$ ), pyrrhotite ( $\text{Fe}_{1-x}\text{S}$ ). Minor ore components include chalcopyrite ( $\text{CuFeS}_2$ ), sphalerite ( $\text{ZnS}$ ), galena ( $\text{PbS}$ ), cobaltite ( $\text{CoAsS}$ ), gersdorffite ( $\text{NiAsS}$ ), native gold and electrum. The main sulphide phases thus represent minerals of the system Fe-As-S and form grains hundreds of microns in size, ranging up to the mm-scale. In most cases, arsenopyrite and pyrite were relatively larger in size than the co-existing pyrrhotite. Cobaltite and gersdorffite were the only Ni- and Co-bearing sulpharsenides identified at a scale of tens of microns (Figure 8D, 9F). The main ore minerals are commonly fractured, but the intensity of superimposed brittle deformation varies depending on the degree of later veining. Larger sulphide and sulpharsenide grains are abundant within the vein quartz, with finer crystals splaying into the adjacent matrix (Figure 5A).

**Pyrite** ( $\text{FeS}$ ) is the most abundant ore mineral which and was observed in two distinct lithologies. Pyrite is the only sulphide present in the nine samples from the upper sulphide-bearing lithologies (407-476 m; DM1-DM10). Pyrite within the upper sequence only occurred as veins within the extremely deformed laminated within the beds (Figure 5D). In the Lower sequence mineralization ( $\sim$ >640 m), pyrite contains two different textures, as euhedral to subhedral crystal with typical cubic nature and as veining (Figure 4F). Microscopic optical observations of pyrite crystals present brecciated textures existing within tiny microspheres and as porous cores with a well crystallised boundary; evidence of core to rim overgrowth (Figure 11D). Commonly, intergrowth and overprinting textures of pyrite are associated with arsenopyrite, chalcopyrite and pyrrhotite with similar grain sizes in varying samples (Figure 6C, 6D).

**Arsenopyrite** ( $\text{FeAsS}$ ) is the second most common ore mineral and co-exists with most of the ore minerals. Arsenopyrite is commonly observed as idiomorphic grains, as coarse grains within vein quartz and finer grains splayed into the adjacent rock matrix. Arsenopyrite is seen together with pyrite in the quartz vein, ranging in size from hundreds of micron to a few mm (Figure 5F & 4F). Visible gold is characteristically seen as inclusions within fractures in the arsenopyrite or at the margins of arsenopyrite crystals (Figure 12A, 7D), more rarely as inclusions within the central parts of arsenopyrite crystals (Figure 10C). SEM BSE images revealed fine (generally  $<1\ \mu\text{m}$ ) aggregates of galena to be contained along the edges of arsenopyrite, within fractures and adjacent to grains (Figure 7E, 12E).

Figure 9B illustrates brecciated textures of recrystallized fine-grained arsenopyrite crystals some lying between two less deformed arsenopyrite grains. Two stages of arsenopyrite crystallisation are recognised, notably in sample DM18. The first stage contains finer grains with high density of gangue inclusions (Fig 10F), whereas the second stage is distinguished by large idiomorphic textures, with fractures propagating through the crystal (Figure 11F). Sphalerite is commonly present as tiny inclusions within fractures of finer (<100 µm) grains of arsenopyrite (Figure 7A).

**Pyrrhotite** ( $\text{Fe}_{1-x}\text{S}$ ) is ubiquitous throughout the samples, typically occurring in moderate amounts as inclusions within arsenopyrite and pyrite. Sample 22DM (Figure 8C) contained larger pyrrhotite crystals (~50 µm to >1 mm) that exhibit anhedral textures within chlorite-altered vein quartz. Pyrrhotite hosts some of the minor ore minerals, including **cobaltite** ( $\text{CoAsS}$ ) and **sphalerite** ( $\text{ZnS}$ ) (Figure 8D, 8E). Cobaltite is preserved as idiomorphic to subhedral crystal shapes intimately associated with pyrrhotite than any other ore mineral, along the margins of angular pyrrhotite grains within sample 22DM (Figure 8D). Occasionally, replacement of arsenopyrite by pyrrhotite is evident although rare, but some intergrowths of pyrrhotite with arsenopyrite are observed (Figure 10E, 10F).

**Chalcopyrite** ( $\text{CuFeS}_2$ ) has a varied grain size (10-100 µm) and is intimately associated with pyrite and arsenopyrite as inclusions or at grain boundaries (Figure 6C). Chalcopyrite inclusions are also observed within coarse-grained arsenopyrite. A rare occurrence of pyrrhotite overprinting a chalcopyrite crystal within a pyrite overgrowth is observed in sample DM41 (Figure 10E). In some rare instances, chalcopyrite is seen overprinting arsenopyrite and intergrowth with pyrrhotite (Figure 7A). Pyrite and arsenopyrite in this case (sample DM30) contained breccia type grains.

## GOLD MINERALS

**Native gold** (Au) was identified by optical microscopy and confirmed by SEM imaging and SEM-EDAX analysis in 7 samples (DM15, DM16, DM23, DM24a DM38, DM41, DM29), where it is commonly associated with arsenopyrite with crystals ranging from <5 µm to 15 µm. These samples all come from the “Puck Group” sequence, characterised by pervasive chlorite alteration zones. ‘Free’ gold was also observed within vein quartz displaying grain sizes of 10 to 50 µm. Native gold is not seen enclosed within pyrite grains, with the exception of sample DM16, where gold is within and around edges of pyrite and arsenopyrite. Partial recrystallization of pyrite and arsenopyrite and release of gold originally locked in the sulphides led to reconcentration of gold at grain margins and in the immediately adjacent matrix (see below).

Gold is consistently seen throughout samples within the mineralised zone as inclusions in pyrite and arsenopyrite, commonly as veins within arsenopyrite fractures and native gold within the matrix. Sample DM16 exhibited gold grains which have remobilised from arsenopyrite and pyrite crystals into the matrix (Figure 7D, 7E). Remobilised grains varied in sizes from ~50 µm to <10 µm containing subhedral-euhedral textures. Individual Au grains within the matrix were only ~5 µm

from pyrite or arsenopyrite. Galena exhibited similar textures as Au, commonly seen near grain boundaries and within fractures of arsenopyrite. Unless grains of either Au or galena were x-rayed using the EDAX it is difficult to distinguish both during back scattered imaging. Figure 7E exhibits galena and Au inclusions identified relatively close together (<10  $\mu\text{m}$ ) near an arsenopyrite grain boundary. Similarly, veins of galena and Au also existed in the same arsenopyrite grain hence using galena as a proxy when searching for Au crystals using optical microscopy.

## OTHER MINERALS OF INTEREST

In the present study, the Fe-Ti oxides (illmenite and rutile) are identified as major components in certain lithologies, particularly within the 'Puck Group'. Rutile is the most abundant Ti-bearing mineral, and commonly occurs together with REE-bearing minerals such as monazite and thorianite, which are observed at the margin of rutile grains (Figure 9E). (Figure 9E) shows anhedral and apparently homogenous thorianite closely associated with monazite and zircon grains displaying sectorial zoning (Figure 10A).

## Electron Microprobe mineral compositional data (EPMA)

Seventeen samples were analysed by EPMA to characterise chemical variation relative to stoichiometry within the major and subordinate ore minerals, as well as gold and associated minerals. The selected suite was primarily chosen to cover the main mineralised zone as well as pyrite from the upper mineralised sequence.

A total of 152 analyses were obtained, covering arsenopyrite, pyrite, pyrrhotite, sphalerite and native gold/ electrum. The full dataset (individual analyses) is given in Appendix 2. Tables 2-6 show selected single analyses and calculated means in terms of wt% values and calculated mineral formulae. The latter are expressed in number of atoms per formula unit (a.p.f.u.), allowing comparison with the ideal formulae of each analysed mineral.

Electron probe datasets of **arsenopyrite** are given in Table 2. The measured stoichiometry of arsenopyrite (ideally  $\text{Fe}_{1.0}\text{As}_{1.0}\text{S}_{1.0}$ ) varies within the ranges of 0.95 to 1.00 a.p.f.u. Fe, 0.82 to 0.95 a.p.f.u. As and 1.04 to 1.22 a.p.f.u. S. Minor detectable concentrations of Co, Ni and Se were observed; other elements were below detection limit. In terms of formulae, Co varies up to 0.001 a.p.f.u., Ni up to 0.012 a.p.f.u. and Se up to 0.013 a.p.f.u.

Figure 14 illustrates the compositional variation in arsenopyrite in terms of a.p.f.u. As(+Sb) versus a.p.f.u. S(+Se+Te). Two negative correlations are given from the plot, the majority of points plotting within the low-S cluster. The S enriched-cluster gives a reasonably strong correlation between the two variables although outliers tend to be highly S-depleted and As-enriched.

Figure 14B shows a portion of the ternary system (As+Sb)-(S+Se+Te)-(M), where M=(Fe+Co+Ni), illustrating compositional variation in arsenopyrite. Samples 19DM (740 m), 38DM (858 m) and 41DM (863m) are slightly depleted in Total M.

Electron probe microanalysis of **pyrrhotite** (Table 3) also shows variation with respect to ideal stoichiometry ( $\text{Fe}_{1-x}\text{S}$ ). If calculated to 2 a.p.f.u., Fe content varies from 0.906 to 0.926 a.p.f.u. and S from 1.069 to 1.089. Among minor elements, consistent concentrations of Ni were measured (0.004 to 0.003 a.p.f.u.). Detectable Se was also noted in some analyses, although most analyses gave values <mdl. Figure 15A illustrates atom. % Total M (Fe+Co+Ni+Cu) vs. S (+Se) for pyrrhotite measuring S-poor pyrrhotite compositions (within the fields of  $\text{Fe}_7\text{S}_8$  and  $\text{Fe}_6\text{S}_5$ ).

EPMA data for **pyrite** are shown in Table 4. The mineral is essentially stoichiometric ( $\text{FeS}_2$ ), with only minor amounts of other elements. Detection limits of As within stoichiometric pyrite vary from 0.000 to 0.019 a.p.f.u.

Microprobe analysis of native gold grains (Table 5) returned consistently high concentrations of Au, typically ranging from 93.3 to 94.9 wt% and accordingly low Ag content (mean 6.43 wt%). Among the other elements, only Bi gave values above mdl (mean 0.303 wt%). Supplementary data on 13 additional gold grains (by SEM-EDAX) confirmed the limited range of gold composition in the analysed samples (ca. 87-93 wt% Au). Figure 15C binary plot of Au vs. Ag atom% verifies that majority of EPMA analysed grains are native Au except one rare pure Ag grain that was not identified prior to EPMA analysis.

The microanalytical dataset for **sphalerite** (Table 6) shows all analysed grains to be close to end-member ZnS. Trace amounts of Cu, Ag, Cd, In and Sn were, however, measured, attaining maxima of 0.245, 0.039, 0.117 and 0.032 wt%, respectively. Re-calculation of results as mol% ZnS, CdS and FeS are shown in the table. Calculated mean values of mol% ZnS, CdS and FeS are 89.8, 0.1 9.8 mol%, respectively.

Figure 15C shows a histogram of mol% FeS in sphalerite. The mol% FeS content of sphalerite can potentially be applied as a geobarometer if the sphalerite was equilibrated with both pyrite and/or hexagonal pyrrhotite during cooling (Scott *et al.* 1976). The pressure is temperature-independent up to at least 5 kbar over a very wide range of temperatures encompassing greenschist to upper amphibolite facies of regional metamorphism. The majority of the sphalerite grains at Oberon analysed by EPMA were intimately associated only with pyrrhotite, limiting the applicability of the geobarometer as it does not fully meet the required criteria. Indeed, taking the mean 9.8 mol% FeS from the EPMA analyses gives an unrealistically high (6-8 kbar) inferred pressure T-X projection onto the FeS-ZnS join of sphalerite from Scott *et al.* 1976; Figure X). The relatively mild metamorphism at Oberon suggests that peak pressures were significantly lower than 6-8 kbar.

## LA-ICPMS trace element geochemistry

A total of fourteen selected samples from drillhole TID0065 were analysed by laser-ablation inductively-coupled mass spectrometry (LA-ICPMS) to assess the variation of trace-element distribution within arsenopyrite and pyrite. Prior to laser ablation, each sample was investigated by SEM to capture and document high-resolution images of the grains to be ablated.

The dataset resultant includes 159 individual analyses (113 from arsenopyrite, 46 from pyrite). The results are presented as ppm values in Tables 7 and 8, each organised by sample number in order of increasing depth from drillhole TID0065. The mean concentrations for each sample set are presented below the data columns of each element.

### PYRITE

LA-CPMS analysis of 46 spots (Table 7) in 4 samples shows significant variation of trace elements from sample to sample. **Gold** concentrations in pyrite were very low: the highest individual spot analysis gave 4.6 ppm, and the means for the different samples ranged between 0.11 ppm and 1.1 ppm. These values are low considering that (a) very fine inclusions of Au were identified within pyrite by SEM and (b) the pyrite is As-bearing, normally a pre-requisite for Au enrichment. As vs. Au plot shows two separate trends; majority lie within a cluster depleted in As in contrast to As enriched trend (Figure 17A) Nevertheless, the dataset does confirm that the pyrite contains measurable concentrations of gold, but that these concentrations carry little economic significance. **Silver** concentrations were similarly low. Despite these low concentrations, (Figure 17C) depicts the strong positive correlation between Au and Ag in pyrite from the mineralised zones (DM10, DM28 and DM30).

Concentrations of **cobalt** and **nickel** were identified. The wide range of values within each sample suggest extensive zonation with respect to Co and Ni, even if this was not seen by SEM. Cobalt and Ni concentrations in pyrite from sample DM3 ('upper' zone) were considerably lower than those in the mineralised zone, offering a potential geochemical discriminator. Other elements present at significant concentrations in pyrite include **lead** and **bismuth**. **Lead** concentrations peak at 779 ppm in sample DM30 (Table 7), with a total sample average of 103 ppm. Lead enrichment in pyrite is unusual and is probably related to microscopic inclusions of galena. A moderate positive correlation is observed between Pb and Bi (Figure 17E), except in sample DM3, again supporting that pyrite from the 'Upper' sulphide zone is genetically distinct.

Of note is the consistent enrichment in **antimony** (highest mean value of 48 ppm in sample DM10 with variation from 1.6 to 94 ppm). **Copper** concentrations were highest in sample DM3 (mean 583 ppm, highest single analysis 4600 ppm (Table 7)). **Thallium** is generally observed in minor amounts, with little variation. **Selenium** content is low and fairly consistent throughout the dataset. **Zinc** values were generally low or below detection limit with the exception of sample



DM30 which recorded an anomalous 445 ppm (micro-inclusions of sphalerite?). Other elements including Hg, Te and V were consistently close to, or below detection limit.

## ARSENOPYRITE

Ten different samples were ablated, which consisting of significant concentrations of a range of trace elements which include As, Au, Ag, Bi, Pb, Sn, Te, Tl, Zn, Ni, Co, V, Se, Sb, Mn and Hg (Table 8). Element concentrations within targeted arsenopyrite grains in the different samples have implications for understanding ore genesis.

Arsenopyrite is enriched in Au, Ag, Co, Pb, Ni, Mn and Sb (Table 8). Figure 18 is a series of histograms showing the distributions of Au, Ag, Te, Pb, and Bi. Note the distribution of some elements have similar close to regular Gaussian distributions. Tellurium demonstrates a negatively skewed distribution.

**Gold** concentrations show extreme variance with the highest concentrations being from sample DM26, where one spot analysis gives 4464 ppm and the mean for the sample is 338 ppm. These high and widely ranging concentrations are taken to indicate the presence of gold nanoparticles within the arsenopyrite. The main target areas for ablation were fractured zones of arsenopyrite grains which generally gave significantly elevated values of Au.

Figure 20, 21 represents the variation in gold concentration from LA-ICP-MS analysis in different textural sub-types of arsenopyrite. Analysis for sample DM38 gave minimum and maximum spot values of 0.53 ppm and 227 ppm Au, respectively. Sample DM16 gave one of the highest individual spot analyses (1200 ppm Au) within a grain boundary between pyrite and arsenopyrite. Figure 22E, 22F clearly show that higher Au concentrations are favoured in areas of fracturing and brecciation.

Flat time-resolved depth profiles (Figure 22) indicate that some trace elements are in solid solution within the arsenopyrite. In contrast, spectra for spots where high Au concentrations are noted (e.g. DM16, spot 7; Figure 22D) are very noisy Au, with the spectra giving clear evidence for fine particles or nanoparticles of gold within the arsenopyrite. Some spectra are, however, more equivocal. The time-resolved depth profile for DM38 spot 10 (Figure 22E) shows similar noisy signals for Au and Ag in the second half of the spectra, but otherwise the signals are remarkably flat. This can be interpreted in terms of the presence of solid solution Au and Ag as well as the presence of inclusions of electrum.

**Nickel** concentrations are reasonably constant, having a low mean of 192 ppm (DM13) and a highest of 875 ppm (DM16) (Table 8). **Cobalt** varied remarkably with high spot analysis recorded at 4450 ppm and total mean sample 441 (DM18) in contrast to spot analysis below detection limit (DM23) and lowest mean value at 37 ppm (DM13). Majority of samples contained variable

amounts of **lead** such as DM16 (Table 8) recording a high 1006 ppm and a low 8.5 ppm. **Bismuth** remained constant having no recorded concentrations >100 ppm and none below detection limit.

**Silver** concentrations are consistently low in arsenopyrite and pyrite, having a total sample mean of 3.8 ppm in arsenopyrite and 1.1 ppm in pyrite. Pyrite samples attributed a higher total sample mean of Ag than Au. Spot analysis in which recorded highest Au anomaly at 4464 ppm also recorded the highest Ag anomaly at 216 ppm (Table 8).

Other trace metals detected in arsenopyrite include **mercury, zinc, copper manganese, vanadium** and **thallium**. There is a low degree of variance within the sample means for these metals, excluding Mn which gave minima and maxima from 7 ppm and 228 ppm respectively (Table 8). Mercury and Tl concentrations are extremely low. All analysed grains displayed detectable concentrations of antimony. Tellurium is deficient throughout the dataset with the exception of sample DM13.

Trends in trace element distribution can be seen on Figure 16. Silver and gold are in solid solution, and display a very strong positive correlation (Figure 16A). The corresponding  $r^2$  is given at 0.8007. Similarly, Pb vs. Au, Pb vs. Ag, Pb vs. Bi and Bi vs. Au plots illustrate a number of positive inter-element correlations. Just as there are very small Au inclusions there are also inclusions of galena of similar size (Figure 16C). The trends indicate a combination of such semi-regularly distributed inclusions of various sizes plus some solid solution.

### **Focussed ion beam – scanning electron microscope (FIB-SEM) study**

The FIB-SEM study was intended to identify whether fine particles (150-2000 nm) and/or nanoparticles (<150 nm) of gold were present in arsenopyrite as suggested by the LA-ICP-MS data. Specific target areas for high-resolution imaging and 3-D tomography were the heavily fractured and brecciated sub-textures in arsenopyrite. Trenches were dug out where tiny inclusions or microveins of Au were present.

High-resolution secondary electron FIB-SEM imaging illustrates that fine particles and nanoparticles of gold occur adjacent to the gold microveinlets (Figure 13). The images show how gold has been remobilised into fractures within the arsenopyrite. The angular symmetry of the fractures implies that fracturing has followed cleavage domains in the sulphide. A conspicuous feature is that the microveinlets also contain voids adjacent to the gold grains (Figure 13D). Increased porosity is a common feature associated with grain-scale remobilisation of gold. Interestingly, imaging shows not only confirms that Au is present as fine/nanoparticles but also that the gold grains are aggregates of multiple grains and that they are twinned down to the smallest scale (Figure 13F, 13G). FIB-EDAX analysis also confirmed the earlier hypothesis that both galena and gold exist as finest-scale particles and that galena can also occur as sub-microscopic veinlets (Figure F). The identification of aggregate and twinned gold may indicate that

remobilisation and subsequent reconcentration took place in a localised stress field, presumably within the waning stages of metamorphism.

## DISCUSSION AND CONCLUSIONS

The present study has focussed on various aspect of gold mineralisation at Oberon. The study has aimed at determining the distribution of Au within the main ore minerals, arsenopyrite and pyrite, as well as identifying information of genetic importance in the host lithologies. This information bridges the previous gap in knowledge between understanding the style of gold mineralization at Oberon in comparison with Callie.

Understanding relationships and variation among trace element distributions, macroscopic and microscopic textures and crystal chemistry are valuable tools for constructing a sustainable model for ore genesis. The new data collected in the study allow refinement of a genetic model for Oberon and comparison with observations elsewhere in the Tanami orefield. Moreover, the recognition of grain-scale gold remobilisation associated with arsenopyrite deformation and recrystallization provide valuable new evidence for the microscopic and sub-microscopic processes governing gold distributions in orogenic-style gold ores in general.

### Ore Genesis

#### LITHOLOGICAL CONTROLS

Figure 2 (after Huston *et al.* 2007) illustrates important features of the Tanami mineral system, highlighting the interplay between igneous, metamorphic, structural deformation and mineralising processes that contributed to formation of the Tanami lode-gold deposits. The figure connects a series of governing factors, including elevated heat flow, emplacement of synorogenic granites and associated release of hydrothermal magmatic fluids, a deep-seated structural corridor that taps the mid crust and acts as the main fluid pathway, and the presence of granitic buttresses which agitate the stress field and play a role in determining the geometry of the orefield-scale structural architecture. Locally, essential factors are the second-order structural arrays or dilational jogs which were also controlled by smaller granitic intrusions having perturbed the stress field(s). Many deposits occur where tensional vein arrays crosscut local anticlines or structurally complex/thickened zones in carbonaceous sediment rocks or iron formation (Huston *et al.* 2007). Oberon lies within a pre-existing anticline, where mineralisation is hosted within competent units such as sandstones, turbidites, phyllites and boudined cherts of the Killi Killi Formation.

Models created by previous workers are based broadly on reflection seismic data (Goleby *et al.* 2006) and on inversion and forward modelling of potential field data (Meixner & Lane 2005;

Vandenberg & Meixner 2003), but also on geochemical data (e.g. Lambeck *et al.* 2011). The new data introduced in the present study has not addressed broad-scale aspects of gold distribution within the Oberon deposit, but has instead allowed an understanding of the distribution and behaviour of Au within lithologies in the mineralised zone.

The study of sequence stratigraphy at Callie by Lambeck (2004) suggests that an anoxic environment represented by a condensed interval within well-bedded carbonaceous horizons hosts the highest grade Au. The graphitic beds within the 'Upper' sequence at Oberon represent a period of anoxic deep seawater deposition. This is supported by the distinctive geochemistry of the contained pyrite. The 'upper' zone pyrite is notably depleted in As. Arsenopyrite exists exclusively within the main mineralised zone and is not seen in the 'upper' sequence. Arsenic assimilation into forming sulphides commonly occurs as sediment is buried below the suboxic and sulphidic redox boundary (Lowers *et al.* 2007).

The main mineralisation occurs, however, within rocks that are not markedly carbon-rich. The whole rock geochemical assay data provided by Newmont confirms the high As content of these rocks. This As was presumably introduced during the hydrothermal episode. It is interesting to note however that Au concentrations in the 'upper' and 'main' sequences are essentially undistinguishable and therefore the inference about distinct depositional and hydrothermal processes in the two Au-bearing horizons is purely speculative.

## GEOLOGICAL EVOLUTION

Prior to metamorphism and establishment of the structural architecture, the Tanami Group was deposited, consisting of the Dead Bullock Formation and the conformably overlying Killi Killi formation. These are interpreted as a deep-water transgressive-regressive package consisting of DBF fine grained sediments which accumulated in relatively deep water beneath storm wave base and thicker bedded coarser grained sediments of the Killi Killi Formation providing evidence of marine regression. Following the intrusion of dolerite sills, the Tanami orogenic event metamorphosed the sequence at greenschist to lower amphibolites facies. Gold mineralisation can be considered as syn-metamorphic (Huston *et al.* 2007). Final structural events in the region, coupled with emplacement of granitic suites (Huston *et al.* 2007) were also critical for localisation of gold throughout the Tanami region.

The metasedimentary units which host the Oberon mineralisation consist of a package of chlorite-altered phyllites which vary between Fe-rich and the lower Ca rich units. The Fe-rich sedimentary units of the 'Puck Group' (Figure 3) host the majority of the mineralisation at Oberon. These probably correlate with high-grade ore-hosting Fe-rich sedimentary rocks elsewhere in the Tanami region (Lambeck *et al.* 2011).

## ARSENOPYRITE GEOTHERMOMETRY

Most of the lower sequence (>550 m) shows a chlorite-dominant lithology, with relatively rare biotite (Figure 6). This suggests that metamorphism was not higher than lower amphibolite facies. No minerals such as garnet or staurolite, indicative of higher metamorphic facies were recognised.

Analytical data for arsenopyrite show a variety of compositions that have implications for understanding ore evolution. Application of the arsenopyrite geothermometer (Kretschmar & Scott 1976) is based upon non-stoichiometric variation in the As:Fe:S ratio in this mineral, offering a potential constraint on the metamorphic conditions at which arsenopyrite crystallized. Sharp *et al.* (1985) emphasise that arsenopyrite geothermometry should not be applied to samples formed under conditions other than greenschist and amphibolites facies.

Representative mean EPMA compositions are plotted on the pseudobinary T-X section as atom% As against temperature (T) on the Asp + Py = Po line, following the calibration of Kretschmar & Scott (1976). A selection of samples with variable a.p.f.u. values give temperatures that range from ~300 °C (DM 24b), ~360 °C (DM18) ~380 °C (DM37), up to a maximum of ~430 °C (DM19). Such temperatures are consistent with the metamorphic evolution of the Tanami region, which grades from greenschist to mid-amphibolite facies with highest grades to the southeast region (Huston *et al.* 2007). The temperatures obtained are also consistent with those obtained from chlorite geothermometry by Silcock (2011).

## Gold distribution

Both arsenopyrite and pyrite can host invisible Au (lattice-bound Au and particles <10 Å; Cook & Chryssoulis 1990), but arsenopyrite is generally known to be the better host for Au. Higher Au concentrations in pyrite are generally facilitated by As incorporation. The EPMA data for pyrite from Oberon data showed that variable amounts of As are incorporated into the lattice, commonly over 1000 ppm (Table X). Despite this, the Au concentrations in pyrite are very low. This suggests that if pyrite had significant Au, this was released during recrystallization. Such a hypothesis is supported by the observation of micron-sized gold grains on the margins of pyrite.

Although analysed concentrations are at least an order of magnitude higher than pyrite, arsenopyrite is also a relatively poor host for invisible gold. Elevated concentrations are restricted to areas of arsenopyrite grains characterised by fracturing and deformation. Gold concentrations outside such areas are typically only a couple of ppm. The extreme variability in absolute concentrations and the noisy time-resolved LA-ICP-MS depth profiles for Au (Figure 22) suggest that nanoparticulate gold can best explain the data, rather than lattice-bound (solid solution) gold. Taken together with the observation of abundant micron-sized inclusions of gold, this suggests that the size range of gold grains extends down from the µm to nm-scale. Evidence for the

presence of smallest-scale nanoparticles (<100 nm) has been found during high-resolution FIB-SEM imaging (Figure 13E, 13F ).

The significance of these observations is two-fold. Firstly, although nanoparticulate gold is widely reported from epithermal and Carlin-type ores (e.g. Palenik *et al.* 2004, Hough *et al.* 2011), it has never been previously observed in an orogenic-style gold deposit. Secondly, the observation of gold that has been clearly remobilised during arsenopyrite recrystallization and subsequently reconcentrated within fractures and as adjacent nanoparticulate inclusions (Figure 13E) offers a valuable insight into grain-scale processes of gold redistribution that operate during metamorphism. The identification of twinning within the remobilised gold (Figure 13G) is an important observation constraining the remobilisation process to the waning stages of the metamorphic event.

In epithermal and Carlin-type ore systems, formation of gold nanoparticles is attributed to (i) the solubility of Au in sulphides is exceeded during sulphide crystallisation resulting in deposition of elemental Au or (ii) exsolution of Au from a metastable sulphide during later stages in the evolution of the deposit (Palenik *et al.* 2004). Since the LA-ICP-MS data suggest that, except where fractured and brecciated, residual Au in arsenopyrite is at best only a few ppm, it is reasonable to assume that condition (i) is not met and that exsolution from a metastable sulphide is the favoured mechanism. Whether the grain-scale remobilisation has taken place via solid-state diffusion or by coupled dissolution-reprecipitation reaction (CDRR, e.g. Cook *et al.* 2009) can only be speculated upon at present.

## Implications

### IMPLICATIONS FOR EXPLORATION

The integrated macro and micro-analytical approach employed in this study reinforces the broad similarities between the mineralisation style at Callie and Oberon. The major distinction lies in the different host rocks and somewhat lower metamorphic grade (Oberon is probably below the garnet isograd). Otherwise, the Oberon gold mineralisation is essentially very similar to that at Callie. Comparable exploration models can thus be applied in the search for other deposits in the immediate vicinity.

The LA-ICP-MS work has revealed that pyrite from the lower (main) mineralised zone differs substantially from that in the 'upper' zone. The latter, which may possibly be syn-sedimentary rather than hydrothermal in origin, could potentially be a geochemical marker horizon of use in further correlation of ore-hosting strata across the region. The intimate association of gold with arsenopyrite and pyrite is conclusive from the petrographic observations and analytical data. Arsenopyrite is the primary host for microscopic and sub-microscopic gold.

## IMPLICATIONS FOR ORE PROCESSING

This study has shown that the ore mineralogy of the Oberon ores is relatively simple, with remarkably few 'exotic' species present. The study has found no evidence for gold in other mineralogical forms, such as Au-(Ag)-tellurides, or alloys such as maldonite ( $\text{Au}_2\text{Bi}$ ), which are reported from other orogenic gold systems in Australia.

Invisible gold, in either pyrite or arsenopyrite, contributes only negligibly to the overall gold budget at Oberon. This is because of (i) the modest concentrations of Au in the sulphides, and (ii) the rather low amount of sulphides in the ore (<5 vol%). Arsenopyrite is clearly the predominant gold hosting sulphide although additional penalties which may compensate for arsenic contamination from tailings will have a marginal effect on the production budget.

The study has shown that the gold grains are, as in Callie, of high fineness. The study has shown, however, that a portion of the gold is fine-grained, commonly <10  $\mu\text{m}$ , and that much of this fine-grained gold occurs as inclusions in the common sulphides. There is thus a risk that this gold will not be liberated and thus recovered if grinding is insufficiently fine. The fine-grained gold extends down to the invisible nanoparticle scale. Although of considerable interest in understanding processes of syn-metamorphic gold release and reconcentration, the nanoparticulate gold is also unlikely to contribute to the overall gold budget at Oberon

## ACKNOWLEDGEMENTS

The support of Newmont (Tanami operations) team is gratefully acknowledged. Particular mention goes to Pascal Hill for his helpful discussions and suggestions when on site. Special thanks to my supervisor Nigel Cook for his guidance, tireless support, enthusiasm and direction which has been enormously helpful through the course of this study. My FIB-SEM work at Adelaide Microscopy was greatly assisted by my co-supervisor Cristiana Ciobanu and her suggestions to improve my work. Finally I would like to express my gratitude to Adelaide Microscopy for the use of their world-class research facility with particular thanks to Angus Netting and Ben Wade for their assistance in microanalytical techniques.

## REFERENCES

- ADAMS G. J., BOTH R. A. & JAMES P. 2007. The Granites gold deposits, Northern Territory, Australia: evidence for an early syn-tectonic ore genesis. *Mineralium Deposita* **42**, 89-105.
- BAGAS L., ANDERSON J. A. C. & BIERLEIN F. P. 2009. Paleoproterozoic evolution of the Killi Killi Formation and orogenic gold mineralization in the Granites-Tanami Orogen, Western Australia. *Ore Geology Reviews* **35**, 47-67.
- BAGAS L., BIERLEIN F. P., ENGLISH L., ANDERSON J. A. C., MAIDMENT D. & HUSTON D. L. 2008. An example of a Palaeoproterozoic back-arc basin: Petrology and geochemistry of the ca. 1864 Ma Stubbins Formation as an aid towards an improved understanding of the Granites-Tanami Orogen, Western Australia. *Precambrian Research* **166**, 168-184.
- BAYLISS P. 1982. A further crystal structure refinement of gersdoffite. *American Mineralogist* **67**, 1058-1064.
- CLARK L. A. 1960. The Fe-As-S system: Phase relations and applications <sup>1</sup>. *Economic Geology* **55**, 1345-1381.
- COOK N. J., CIOBANU C. L. & MAO J. 2009. Textural control on gold distribution in As-free pyrite from the Dongping, Huangtuliang and Hougou gold deposits, North China Craton (Hebei Province, China). *Chemical Geology* **264**, 101-121.
- CRISPE A., VANDENBERG L. & SCRIMGEOUR I. R. 2007. Geological framework of the Archean and Paleoproterozoic Tanami Region, Northern territory. *Mineralium Deposita* **42**, 3-26.
- GIESSE R. F. J. & KERR P. F. 1965. The crystal structures of ordered and disordered cobaltite. *American Mineralogist* **50**, 1002-1014.
- GROVES D. I., GOLDFARB R. J., GEBRE-MARIAM M., HAGEMANN S. G. & ROBERT F. 1998. Orogenic gold deposits: A proposed classification in the context of their crustal distribution and relationship to other gold deposit types. *Ore Geology Reviews* **13**, 7-27.
- HOUGH R. M., NOBLE R. R. P., HITCHEN G. J., HART R., REDDY S. M., SAUNDERS M., CLODE P., VAUGHAN D., LOWE J., GRAY D. J., ANAND R. R., BUTT C. R. M. & VERRALL M. 2008. Naturally occurring gold nanoparticles and nanoplates. *Geology* **36**, 571-574.
- HUSTON D. L., VANDENBERG L., WYGRALAK A. S., MERNAGH T. P., BAGAS L., CRISPE A., LAMBECK A., CROSS A., FRASER G., WILLIAMS N., WORDEN K., MEIXNER T., GOLEBY B., JONES L., LYONS P. & MAIDMENT D. 2006. Lode-gold mineralization in the Tanami region, northern Australia. *Mineralium Deposita* **42**, 175-204.
- KRETSCHMAR U. & SCOTT S. D. 1976. Phase relations involving arsenopyrite in the system Fe-As-S and their application. *Canadian Mineralogist* **14**, 364-386.
- LAMBECK A., HUSTON D. L. & BAROVICH K. 2010. Typecasting prospective Au-bearing sedimentary lithologies using sedimentary geochemistry and Nd isotopes in poorly exposed Proterozoic basin of the Tanami region, Northern Australia. *Mineralium Deposita* **45**, 497-515.
- LAMBECK A., HUSTON D. L., MAIDMENT D. & SOUTHGATE P. 2008. Sedimentary geochemistry, geochronology and sequence stratigraphy as tools to typecast stratigraphic units and constrain basin evolution in the gold mineralised Paleoproterozoic Tanami Region, Northern Australia. *Precambrian Research* **166**, 185-203.
- LAMBECK A., MERNAGH T. P. & WYBORN L. A. I. 2011. Are iron-rich sedimentary rocks the key to the spike in orogenic gold mineralization in the Paleoproterozoic? *Economic Geology* **106**, 321-330.
- MERNAGH T. P., BASTRAKOV E. N., ZAW K., WYGRALAK A. S. & WYBORN L. A. I. 2007. Comparison of fluid inclusion data and mineralization processes for Australian orogenic gold and intrusion related gold systems. *Acta Petrologica Sinica* **23**, 21-32.



- PALENIK C. S., UTSUNOMIYA S., REICH M., KESLER S. E. & EWING R. C. 2004. Invisible gold revealed: direct imaging of gold nanoparticles in a Carlin-type deposit. *American Mineralogist* **89**, 1359-1366.
- RAMSDELL L. S. 1925. The crystal structure of some metallic sulfides. *American Mineralogist*, 281-304.
- SCOTT S. D. 1976. Application of the sphalerite geobarometer to regionally metamorphosed terrains. *American Mineralogist* **61**, 661-670.
- SHARP Z. D., ESSENE E. J. & KELLY W. C. 1985. A re-examination of the arsenopyrite geothermometer: Pressure considerations and applications to natural assemblages\*. *Canadian Mineralogist* **23**, 517-534.
- WYGRALAK A. S., MERNAGH T. P., FRASER G., HUSTON D. L., DENTON G., MCINNES B., CRISPE A. & VANDENBERG L. 2001. Gold mineral systems in the Tanami region: New insights from NTGS-AGSO research. *AGSO Research Newsletter*, 2-9.

## FIGURE CAPTIONS

**Figure 1. (a)** Map showing major crustal elements of the North Australian Craton; illustrating the distribution of Proterozoic sedimentary basins and Archean domains. (Huston *et al.* 2007). **(b)** Solid geology of the Tanami region, representing Proterozoic units including the major mining prospects and gold deposits. Major structures active during preliminary D<sub>5</sub> structural event include NE-trending oblique thrust (dextral) faults and ESE-trending (sinistral) faults that curve into N- to NNW- trending reverse faults localized in supercrustal belts between and around granite complexes (Huston *et al.* 2007).

**Figure 2. (a)** Regional schematic diagram of the Tanami District showing supracrustal, metasedimentary and granitic rocks and their associating structures which host gold mineral systems. Large structural corridors act as the major permeable pathways of hydrothermal fluids which in some cases are localised within anticlinal closures. **(b)** Highlighted in black is the location of Tanami district in Australia. **(c)** Metamorphic facies map of the region showing the location of Oberon in the lower to middle greenschist facies, as interpreted by Huston *et al.* (2007).

**Figure 3.** Simplified stratigraphic column for drillhole TID0065, Oberon. Gold mineralisation is predominantly hosted by the Blake Beds and phyllite units.

**Figure 4.** Macroscopic images taken from Oberon drillhole TID0065 **(a)** Primary dolomite within sandstone unit consisting of calcite pods (625 m) **(b)** Dolomite mudstone within the 'Puck Group' sequence consisting of elongate pods and **(c)** rounded pods with cream rims (dolomite) and green centred aggregates (chlorite) **(d)** Pyrite veining within crosscutting vein quartz within fine grained rock of 'Puck Group' sequence **(e)** Pyrite veining within vein quartz and arsenopyrite disseminations within fine grained sedimentary puck sequence **(f)** Coarse arsenopyrite grains within pervasive quartz veins with sericitic alteration haloes.

**Figure 5.** Macroscopic images taken from Oberon dirllhole TID0065 **(a)** Re-crystallised idiomorphic arsenopyrite grains within vein quartz and disseminations in the matrix **(b)** Reworked quartz and calcite veins within fine grained sedimentary pack sequence **(c)** Boudin chert with mud laminated layers and pyrite bands **(d)** Pyrite veins within microfractures and bands within graphite-rich beds **(e)** Pervasive quartz vein with sericite alteration envelopes and arsenopyrite disseminations within fine grained sedimentary sequence (843 m) **(f)** Re-crystallised pyrite and pyrrhotite veins within sedimentary pack sequence (745 m).

**Figure 6.** Oberon dirllcore photographs illustrating **(a)** Dolomitic mudstone with chlorite alteration consisting of vein quartz within the Ca-rich sedimentary pack sequence **(b)** Fine grained rock within the sedimentary pack sequencing with a large clastic quartz vein and smaller pervasive vein quartz, with arsenopyrite disseminations **(c)** Graphite-rich beds of the Boudin Chert sequence intersected by a major fault zone **(d)** Boudin chert sequence exhibiting pyrite laminated bands, with crosscutting quartz vein. The graphite beds are grading up into fine grained laminated beds of the 'Zebra Rock' sequence. **(e)** Sedimentary pack beds exhibiting pervasive quartz veins with rounded dolomite pods and dolomite haloes (red tinge). Arsenopyrite is also present, within the vein quartz and disseminations. **(f)** Boudin chert exhibiting iron-rich mudstone laminations and pyrite banding mimicking laminated beds and microfractures.

**Figure 7. (a)** Photomicrograph in reflected light showing replacement of fine arsenopyrite grain by chalcopyrite, pyrrhotite and sphalerite (DM10). **(b-f)** Back-scattered electron (BSE) images (DM16) **(b)** Galena crystals adjacent porous zones of an arsenopyrite grain. **(c)** Grains of native gold immediately adjacent to pyrite and arsenopyrite. Tiny inclusions of native gold are also observed within the pyrite crystal and its boundary. **(d)** Native gold remobilised within adjacent pyrite and arsenopyrite crystals. **(e)** Galena and gold inclusions adjacent the grain boundary of arsenopyrite (DM16). **(f)** Native gold inclusions within arsenopyrite.

**Figure 8.** BSE images showing **(a)** Gold inclusion and remobilised gold grains adjacent and within pyrite crystal (DM16). **(b)** Coarse-grained arsenopyrite with multiple fractures and a brecciated zone containing an elongate grain of euhedral pyrite (DM18). **(c)** Photomicrograph in reflected light showing anhedral pyrrhotite with multiple inclusions of gangue minerals within vein quartz (DM22). **(d)** Sphalerite in contact with later pyrrhotite within vein quartz (DM22). **(e)** Photomicrograph in reflected light showing inclusion of native gold within arsenopyrite and adjacent pyrite (DM23). **(f)** Intensely-fractured arsenopyrite grains intergrown with anhedral porous pyrite (DM24B).

**Figure 9. (a)** Laser ablation target area within the fractured zone of an arsenopyrite grain (DM26, spot 13, which gave 4464 ppm Au). **(b)** BSE images showing overgrowth textures of arsenopyrite between two coarse euhedral arsenopyrite crystals. **(c-d)** Photomicrograph in reflected light illustrating **(c)** intergrowth of pyrite around fractured arsenopyrite. Dotted margin resembles area of focus with higher magnification in **(d)** Chalcopyrite intergrowth around pyrite margin; both are included within arsenopyrite (DM30). **(e-f)** BSE images showing **(e)** intergrown monazite and

thorianite at the margin of elongate crystals of rutile, and **(f)** Gersdorffite intergrown with very fine-grained pyrite.

**Figure 10.** **(a)** BSE image of zircon displaying sectorial zoning. Adjacent is a grain of monazite intergrown within tiny inclusions and fractures of the zircon (DM38). **(b-c)** Photomicrograph in reflected light showing **(b)** high-relief arsenopyrite adjacent to intergrown pyrite (DM40), and **(c)** remobilised native gold grain within a gangue inclusion in porous arsenopyrite (DM40). **(d)** BSE image illustrating chlorite crystallizing within void spaces in a fractured grain of rutile (DM41). **(e)** Photomicrograph in reflected light showing arsenopyrite replacing pyrite. Intergrowth detail of pyrrhotite and chalcopyrite adjacent to pyrite and arsenopyrite (DM41). **(f)** BSE image of galena and monazite within a recrystallized grain of pyrite. Pyrrhotite is seen adjacent to the pyrite grain boundary (DM41).

**Figure 11.** **(a)** BSE image of galena and monazite inclusions of pyrite overgrowth and pyrrhotite intergrowth. **(b-e)** Photomicrographs in reflected light illustrating **(b)** Pyrite intergrowth with arsenopyrite grain consisting of Au inclusion. **(c)** Chalcopyrite overprint of arsenopyrite and intergrowing with anhedral coarse grain pyrite. **(d)** Overgrowth pyrite grains with typical cubic textures. **(e)** Porous arsenopyrite grain overprinting pyrite overgrowth. **(f)** BSE image showing **(f)** Fractured coarse arsenopyrite grain with adjacent euhedral pyrite grain with galena inclusions.

**Figure 12.** **(a)** BSE images showing **(a)** Gold veining within arsenopyrite fractures; the area marked by the dotted line is shown at higher magnification in **(b)**. **(c)** Gold within a brecciated zone of arsenopyrite. **(d)** Microvein of galena in arsenopyrite. **(e)** Grain-scale remobilised gold within a fracture in arsenopyrite and at the mutual boundary between pyrite and arsenopyrite. **(f)** Remobilised gold forming a narrow vein within fractures and voids in arsenopyrite.

**Figure 13.** **(a)** High-resolution Focussed Ion Beam (FIB)-SEM secondary electron (SE) images illustrating **(a)** FIB cuts within brecciated arsenopyrite close to a LA-ICP-MS crater. **(b)** FIB-SEM trench crosscutting a micron-sized gold grain within arsenopyrite. **(c)** FIB-SEM trenches intersecting microveinlets carrying remobilised gold within fractured arsenopyrite. The trench identified by the red dotted line is magnified in **(d)** and **(e)**, and the trench identified by the blue dotted line is magnified in **(f)** and **(g)**. **(d)** Microveinlets of gold within fractured zones of arsenopyrite. **(e)** Further magnification showing nanoparticles and fine particles of gold. Note that the gold displays different shades in the image suggesting this is an aggregate of different gold grains. **(f)** Gold microveining with marked boundaries illustrating an aggregate of gold crystals amalgamated together. Note the fine particles adjacent the vein. **(g)** Microveinlet of gold with marked boundaries showing twin lamellae.

**Figure 14.** **(a)** Plot of As(+Sb) vs. S(+Se+Te) plot for arsenopyrite showing compositional variation as determined by EPMA expressed in atoms per formula unit (a.p.f.u.). Only two marked points lie 'above' the ideal FeAsS composition as shown on the vertical axis. Note that the main cluster is slightly depleted in S, whereas the adjacent group of points shows a systematic increase in S. **(b)** Ternary plot of (As+Sb) – (S+Se+Te) – M total (where M= Fe+Co+Ni+Cu) showing the composition

of analysed arsenopyrite in terms of mol% and trends among the dataset. Note the homogenous increase in S from sample (DM 38), resembling S substitution for Fe in the FeAsS site.

**Figure 15. (a)** Binary plot of atom. % Total M (Fe+Co+Ni+Cu) vs. S (+Se) for pyrrhotite as determined by EPMA. Note that all pyrrhotite compositions are S-poor (within the fields of Fe<sub>7</sub>S<sub>8</sub> and Fe<sub>6</sub>S<sub>5</sub> only). **(b)** Native Au vs. Ag binary plot determined by EPMA analysis measure by atom% clearly showing majority of grains analysed are Au with the exception of the Ag outlier. **(c)** Mol% FeS histogram of sphalerite with adjusted log axis on horizontal axis measured by EPMA. Note that the population varies with a mean of 9.8 mol% FeS, which gives unrealistically high inferred pressures in contrast to the mild metamorphism at Oberon.

**Figure 16. (a)** Binary element plots illustrating trends and regression lines in the trace element data obtained by LA-ICP-MS for arsenopyrite. **(a)** Strong positive correlation of Au vs. Ag as expected between the two precious metals. **(b)** Pb vs. Bi plot showing a positive correlation; both metals may be incorporated into the arsenopyrite crystal lattice in solid solution. **(c)** Pb vs. Au plot shows a consistent but rather weak positive correlation; outliers are strongly enriched in both metals, presumably as nanoparticulate galena and native gold. **(d)** Pb vs. Ag plot showing a similar but slightly stronger positive correlation (higher  $r^2$ ). **(e)** Ni vs. Co plot shows that both metals have a weak positive correlation, although arsenopyrite is far more enriched in Ni than Co. **(f)** Bi vs. Au plot reveals a weak positive correlation (low  $r^2$ ); most outliers are far more enriched with Au than Bi.

**Figure 17. (a)** Binary element plots showing trends in the trace element data obtained by LA-ICP-MS for pyrite. **(a)** As vs. Au plot revealing a large cluster with only a very weak positive correlation between the two elements. Outliers with high As and Au give an exponential and far stronger positive correlation. **(b)** As vs. Ag plot showing negligible correlation, with the exception of some spots in which both elements are high. **(c)** Ag vs. Au plot showing two different trends, no correlation identified with the upper sequence pyrite and relatively strong positive correlation with exception of outliers. Note that Ag is more enriched in pyrite than Au. **(d)** Pb vs. Au plot showing two trends, one with a positive correlation and a second trend lacking any correlation. **(e)** Bi vs. Pb plot showing enrichment of Pb within arsenopyrite and a weak positive correlation between the two metals.

**Figure 18. (a)** Histograms (log 10 axis on horizontal axis) showing the distribution of Te, Bi, Au, Pb, Ag, Ni, Sb and Co concentrations within arsenopyrite as determined by LA-ICP-MS analysis. Note the similarities between trends of precious metals and Ni and Co.

**Figure 19. (a)** Histograms (log 10 axis on horizontal axis) showing the distribution of Au, As, Co, Ag, Ni, Pb, Bi and Sb concentrations within pyrite as determined by LA-ICP-MS analysis. Note the similarities between the sub-populations, except for the Sb trend, showing a relatively positive skew in comparison to the precious metals.

**Figure 20.** Reflected light microscope images assembled to indicate the distribution of grains of pyrite analysed by LA-ICP-MS and the Au concentrations determined. Marks showing the target areas of each spot ablation.

**Figure 21. (a)** Composite reflected-light microscope images showing the distribution of selected LA-ICP-MS spot analyses and Au concentrations within each spot. Note that selection of analysed spots was biased towards fractured and brecciated arsenopyrite to verify that higher Au could be correlated with such textures. **(b)** Time-resolved LA-ICP-MS depth profile of spot 8 (256 ppm) showing inconsistency in Au concentration, with a large peak recorded in the spectra thus indicating the presence of fine particles or nanoparticles of gold.

**Figure 22. (a)** Time-resolved LA-ICP-MS depth profile for arsenopyrite (DM38 spot 2) showing flat spectra, thus suggesting that all elements, with the exception of Sn, are in solid solution. **(b)** Photomicrograph in reflected light showing the ablated area of sample DM38 spot 2, a brecciated zone between two coarser grains of arsenopyrite. **(c)** Time-resolved LA-ICP-MS depth profile for spot 6 (sample DM38) showing flat spectra of elements with exception of Sn. **(d)** Time-resolved LA-ICP-MS depth profile for spot 7 (sample DM16) showing a noisy spectra of Au and Ag explained by the presence of nanoparticles and fine particles of gold. **(e)** Time-resolved LA-ICP-MS depth profile for spot 10 (sample DM38) showing a relatively noisy spectra for Au and Ag. **(f)** Photomicrograph in reflected light of spot 10, sample DM38 at the fractured margin of a giant arsenopyrite grain. **(h)** Time-resolved LA-ICP-MS depth profile for spot 2, sample DM16, showing distinct nanoparticles of Au and Ag near the surface of the ablated arsenopyrite which contrasts with the relatively flat spectra towards the end.

# FIGURE 1

**Figure 1:** (a) Map showing major crustal elements of the North Australian Craton; illustrating the distribution of Proterozoic sedimentary basins and Archean domains. (b) Solid geology of Tanami region, representing Proterozoic units including the major mining prospects and gold deposits. Major structures active during preliminary D<sub>5</sub> structural include NE-trending oblique thrust (dextral) faults and ESE-trending (sinistral) faults that curve into N- to NNW-trending reverse faults localized in supercrustal belts between and around granite complexes (Huston et al. 2007)

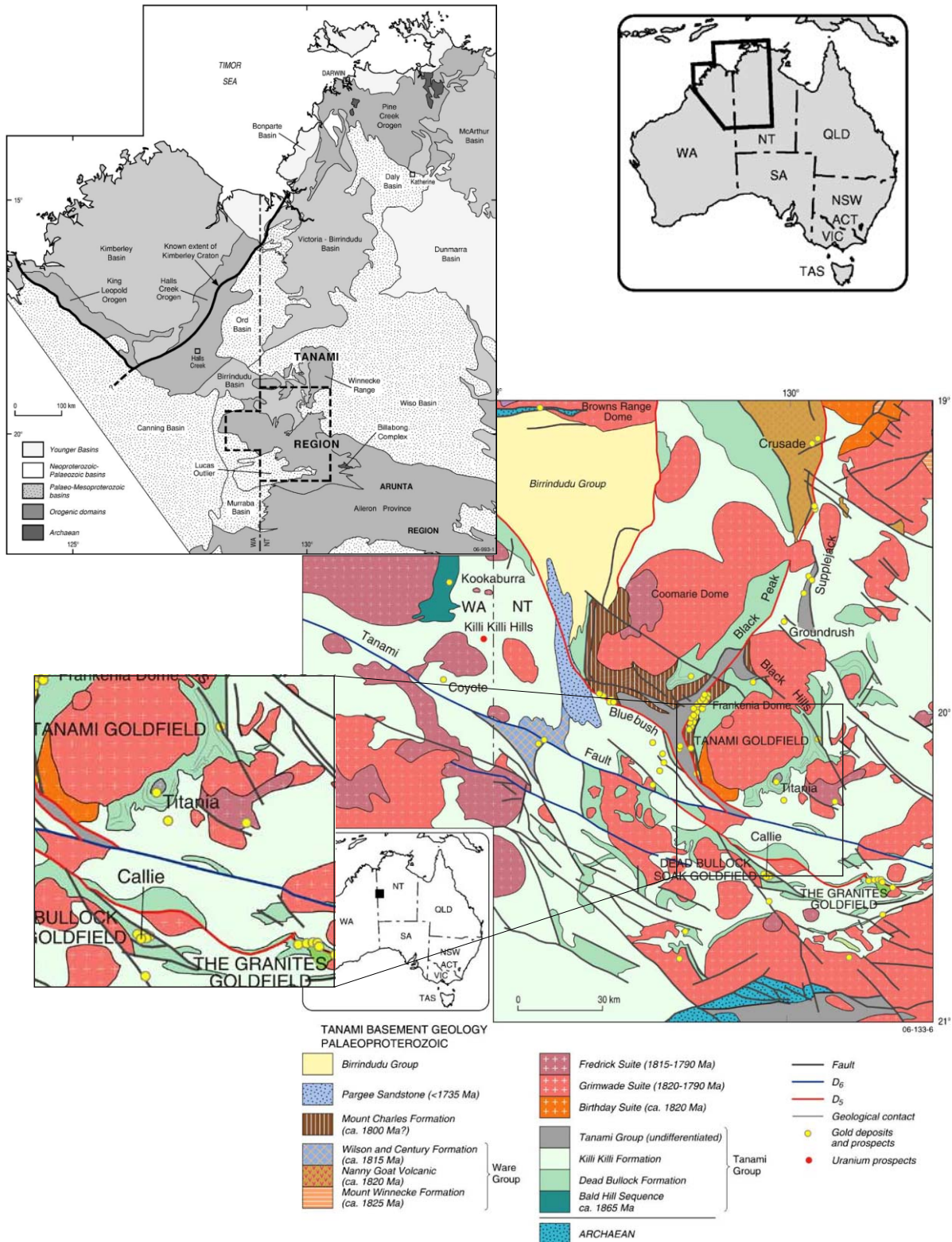


**FIGURE 2**

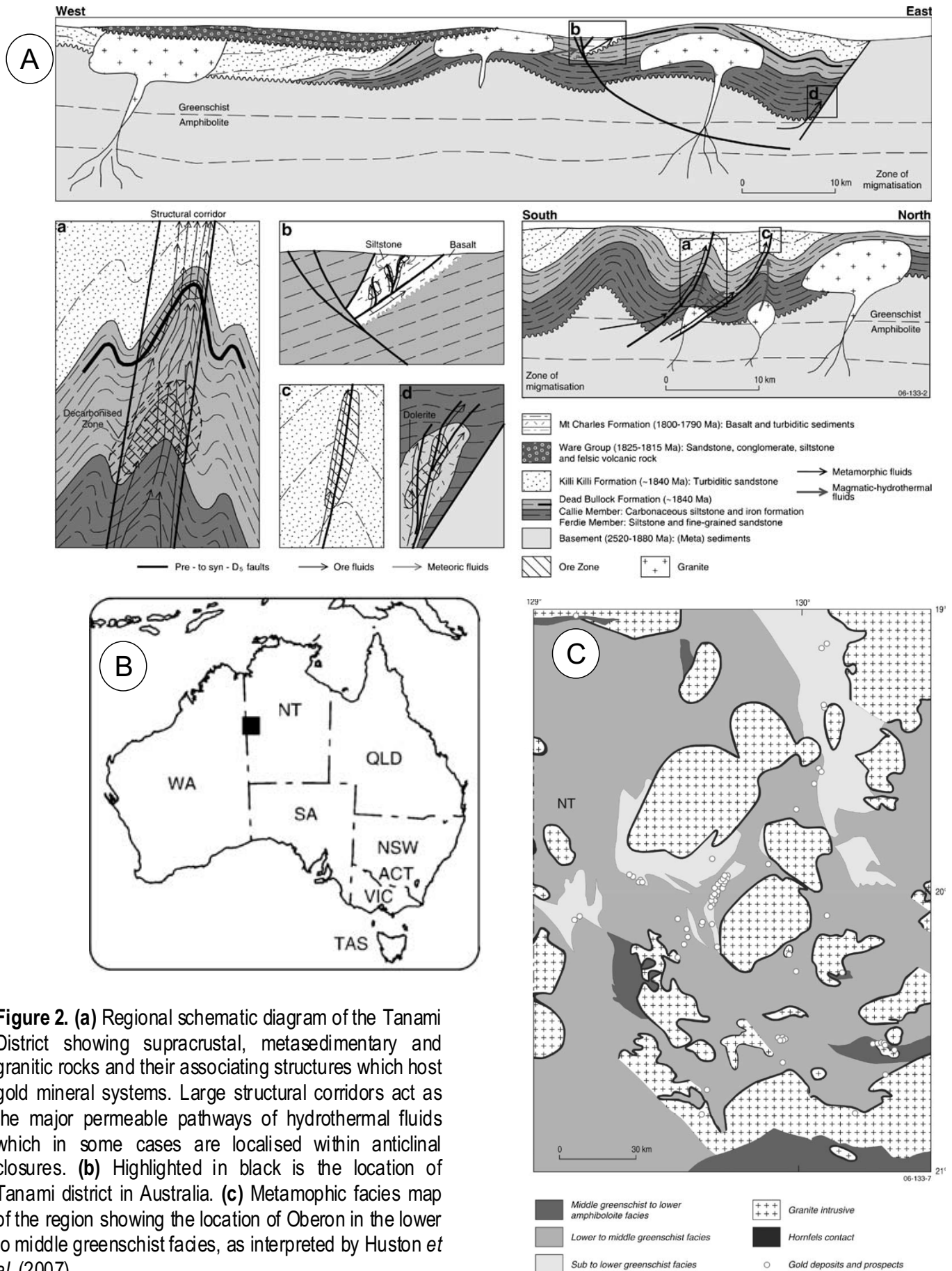


**Figure 2.** (a) Regional schematic diagram of the Tanami District showing supracrustal, metasedimentary and granitic rocks and their associating structures which host gold mineral systems. Large structural corridors act as the major permeable pathways of hydrothermal fluids which in some cases are localised within anticlinal closures. (b) Highlighted in black is the location of Tanami district in Australia. (c) Metamorphic facies map of the region showing the location of Oberon in the lower to middle greenschist facies, as interpreted by Huston *et al.* (2007).

**FIGURE 3**

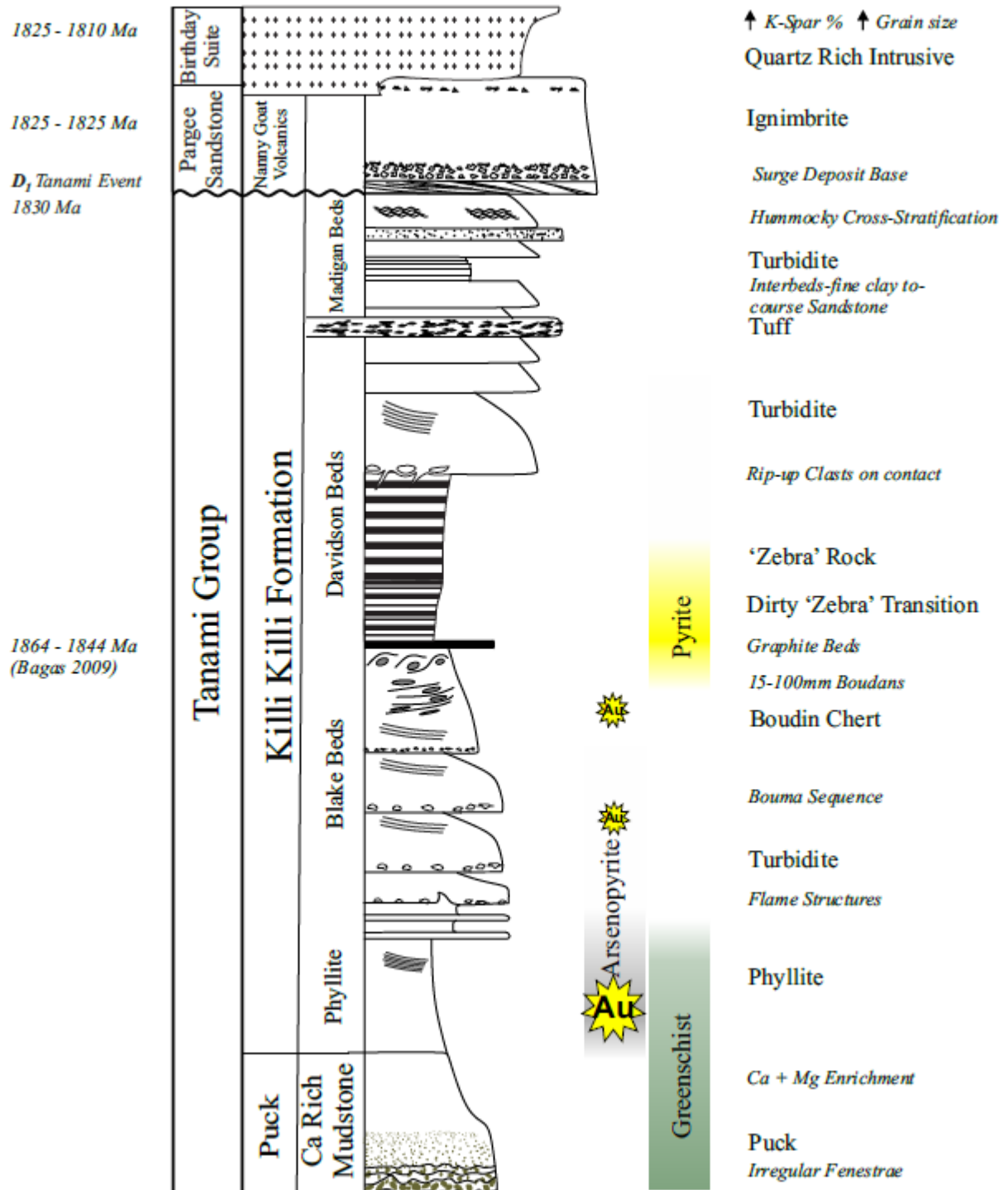


**Figure 3.** Simplified stratigraphic column for drillhole TID0065, Oberon. Gold mineralisation is predominantly hosted by the Blake Beds and phyllite units.



**FIGURE 4**

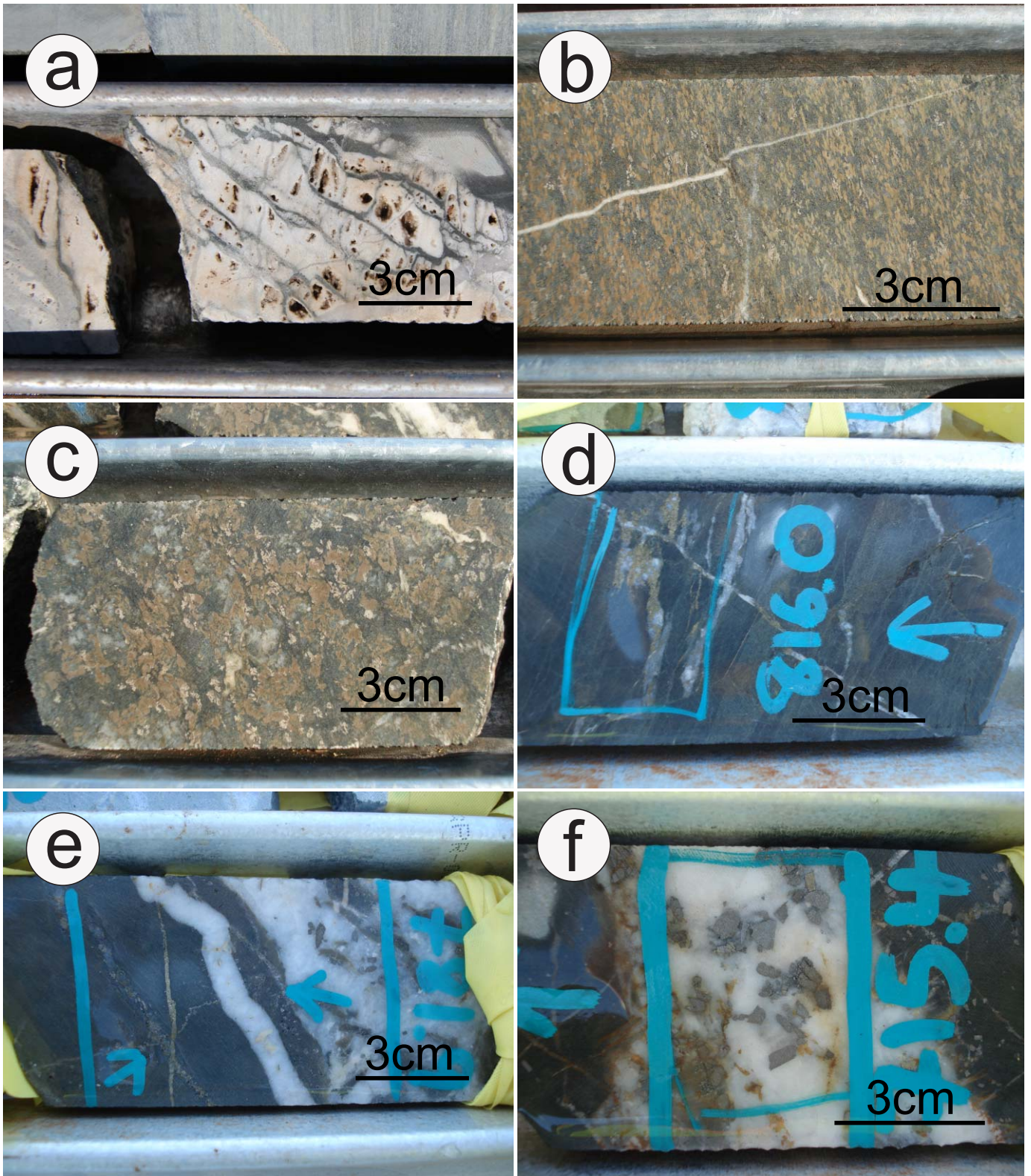


**Figure 4.** Macroscopic images taken from Oberon drillhole TID0065 (a) Primary dolomite within sandstone unit consisting of calcite pods (625 m) (b) Dolomite mudstone within the 'Puck Group' sequence consisting of elongate pods and (c) rounded pods with cream rims (dolomite) and green centred aggregates (chlorite) (d) Pyrite veining within crosscutting vein quartz within fine grained rock of 'Puck Group' sequence (e) Pyrite veining within vein quartz and arsenopyrite disseminations within fine grained sedimentary puck sequence (f) Coarse arsenopyrite grains within pervasive quartz veins with sericitic alteration haloes.

**FIGURE 5**

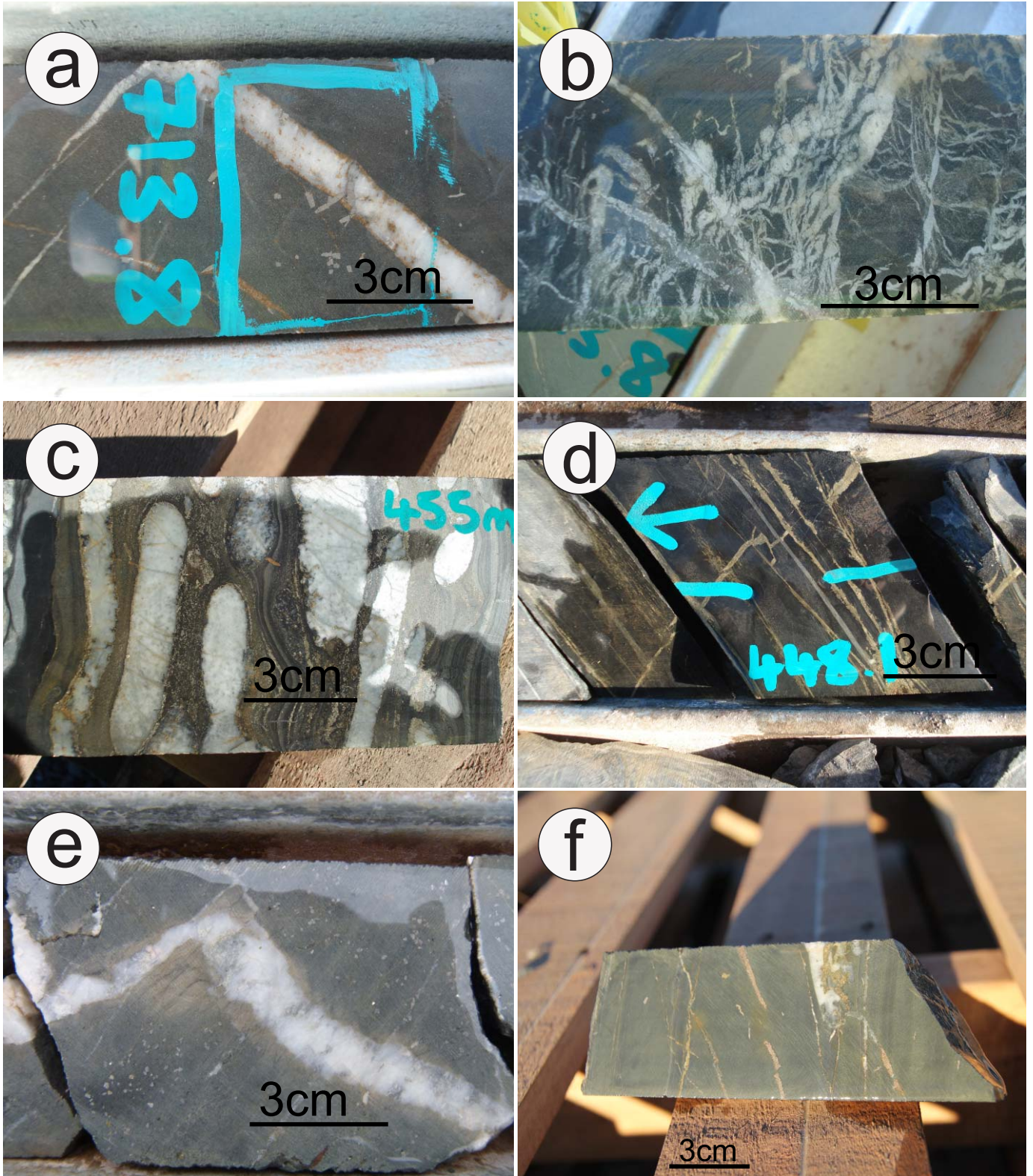


**Figure 5.** Macroscopic images taken from Oberon drillhole TID0065 (a) Re-crystallised idiomorphic arsenopyrite grains within vein quartz and disseminations in the matrix (b) Reworked quartz and calcite veins within fine grained sedimentary rock sequence (c) Boudin chert with mud laminated layers and pyrite bands (d) Pyrite veins within microfractures and bands within graphite-rich beds (e) Pervasive quartz vein with sericite alteration envelopes and arsenopyrite disseminations within fine grained sedimentary sequence (843 m) (f) Re-crystallised pyrite and pyrrhotite veins within sedimentary rock sequence (745 m).

**FIGURE 6**

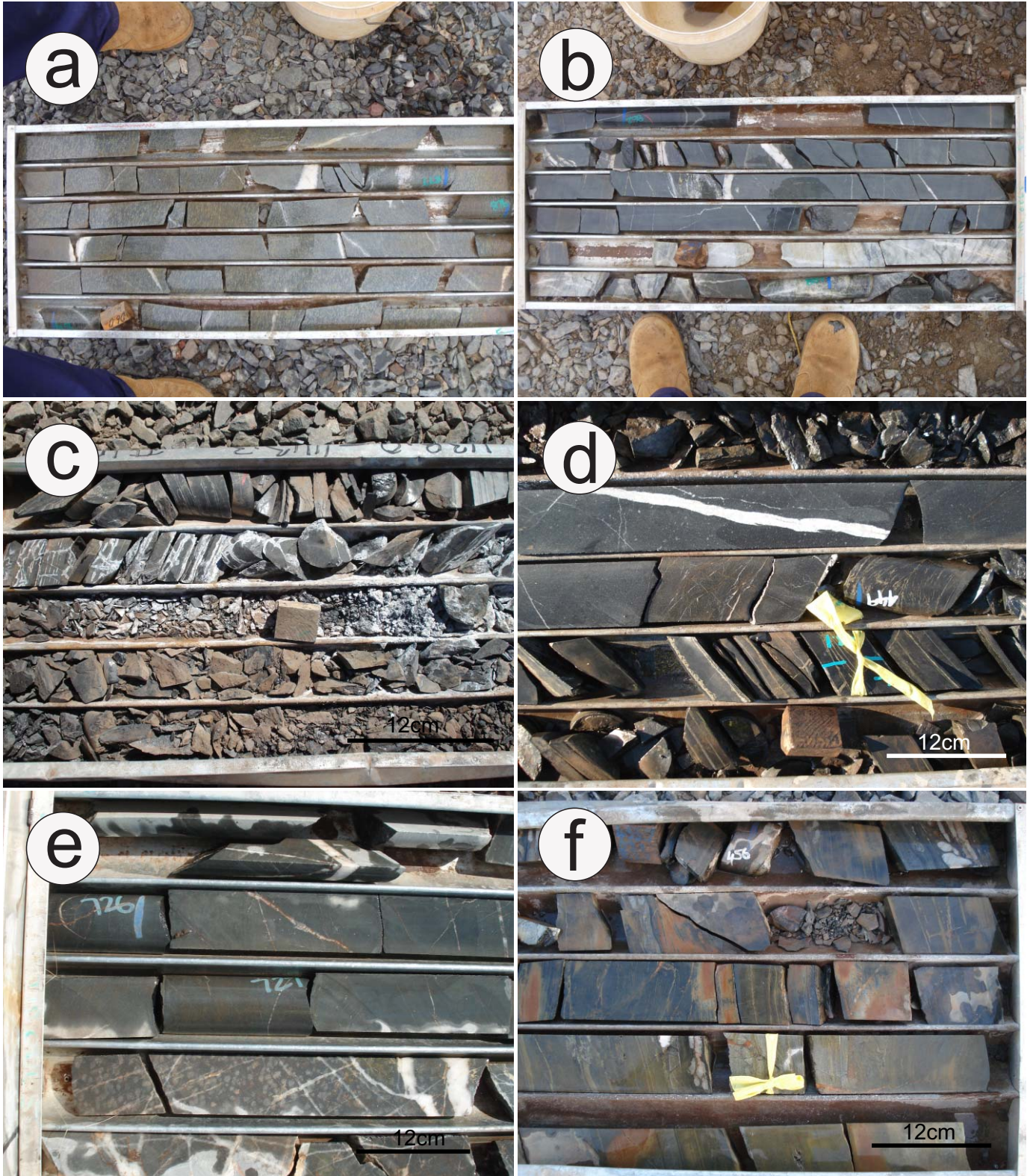


**Figure 6.** Obeorn dirllcore photographs illustrating (a) Dolomitic mudstone with chlorite alteration consisting of vein quartz within the Ca-rich sedimentary puck sequence (b) Fine grained rock within the sedimentary puck sequencing with a large clastic quartz vein and smaller pervasive vein quartz, with arsenopyrite disseminations (c) Graphite- rich beds of the Boudin Chert sequence intersected by a major fault zone (d) Boudin chert sequence exhibiting pyrite laminated bands, with crosscutting quartz vein. The graphitic beds are grading up into fine grained laminated beds of the 'Zebra Rock' sequence. (e) Sedimentary puck beds exhibiting pervasive quartz veins with rounded dolomite pods and dolomite haloes (red tinge). Arsenopyrite is also present, within the vein quartz and disseminations. (f) Boudin chert exhibiting iron-rich mudstone laminations and pyrite banding mimicking laminated beds and microfractures.

**FIGURE 7**

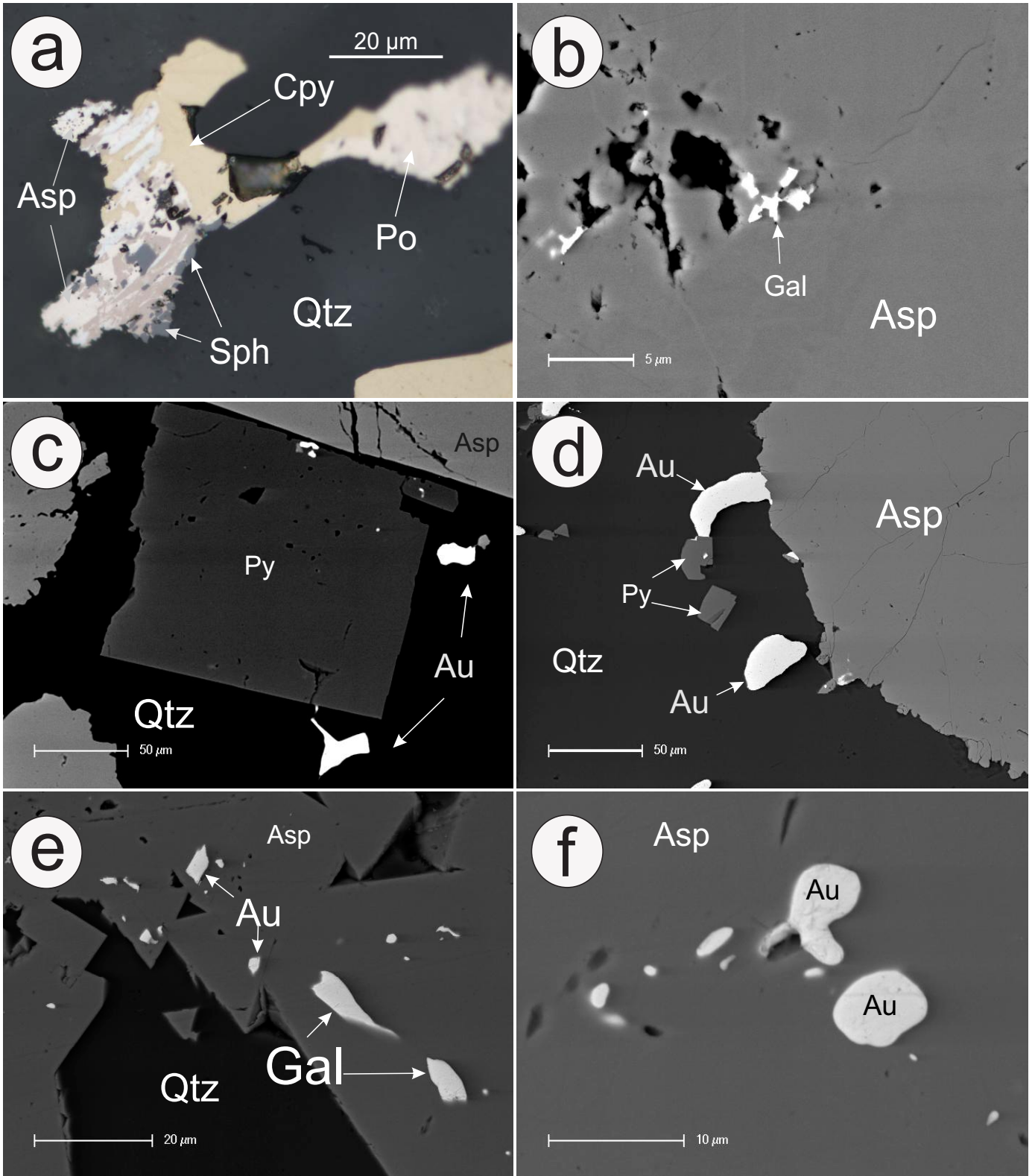


**Figure 7.** (a) Photomicrograph in reflected light showing replacement of fine arsenopyrite grain by chalcopyrite, pyrrhotite and sphalerite (DM10). (b-f) Back-scattered electron (BSE) images (DM16) (b) Galena crystals adjacent porous zones of an arsenopyrite grain. (c) Grains of native gold immediately adjacent to pyrite and arsenopyrite. Tiny inclusions of native gold are also observed within the pyrite crystal and its boundary. (d) Native gold remobilised within adjacent pyrite and arsenopyrite crystals. (e) Galena and gold inclusions adjacent the grain boundary of arsenopyrite (DM16). (f) Native gold inclusions within arsenopyrite.

**FIGURE 8**

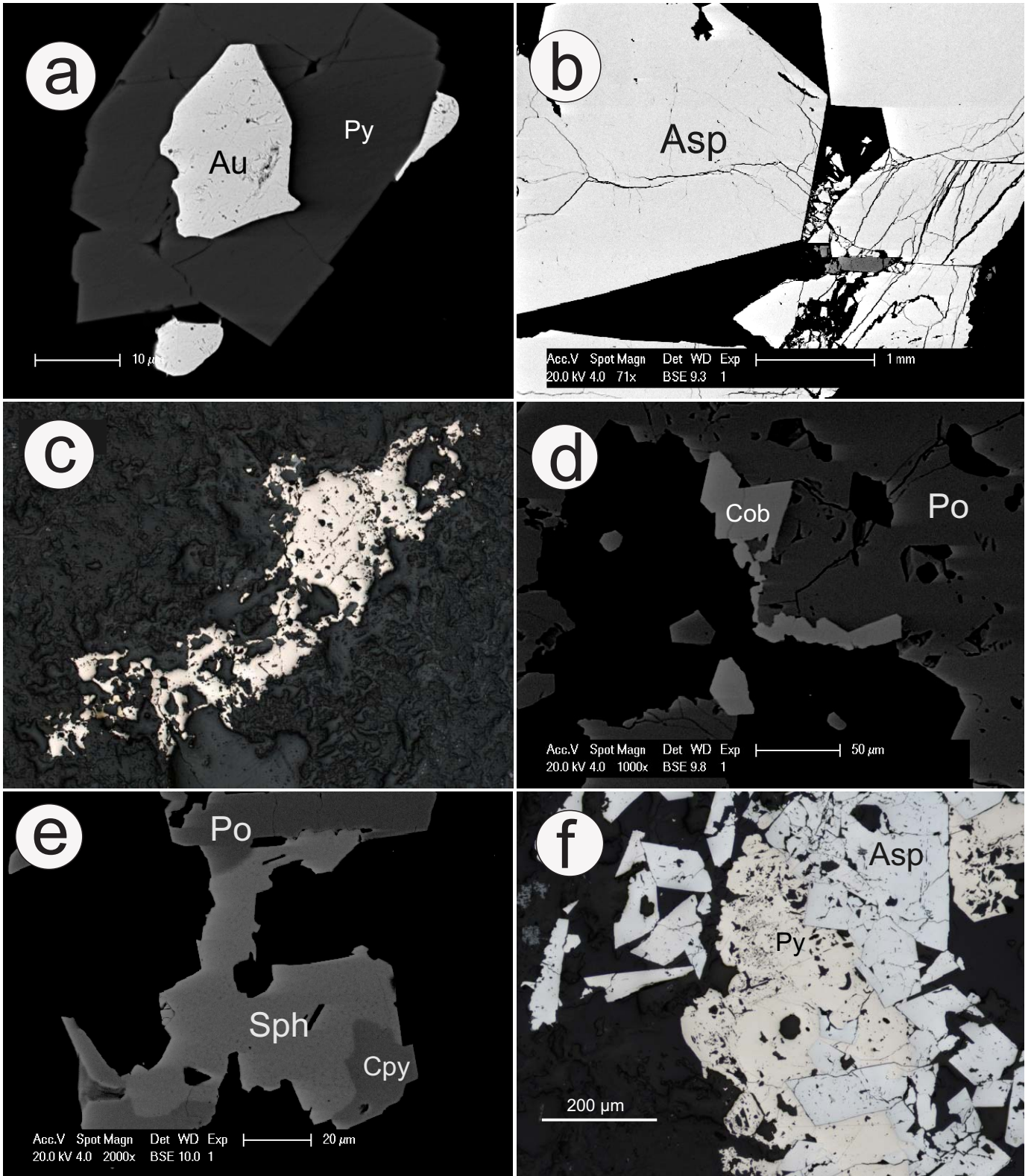


**Figure 8.** BSE images showing (a) Gold inclusion and remobilised gold grains adjacent and within pyrite crystal (DM16). (b) Coarse-grained arsenopyrite with multiple fractures and a brecciated zone containing a elongate grain of euhedral pyrite (DM18). (c) Photomicrograph in reflected light showing anhedral pyrrhotite with multiple inclusions of gangue minerals within vein quartz (DM22). (d) Sphalerite in contact with later pyrrhotite within vein quartz (DM22). (e) Photomicrograph in reflected light showing inclusion of native gold within arsenopyrite and adjacent pyrite (DM23). (f) Intensely-fractured arsenopyrite grains intergrown with anhedral porous pyrite (DM24B).

**FIGURE 9**

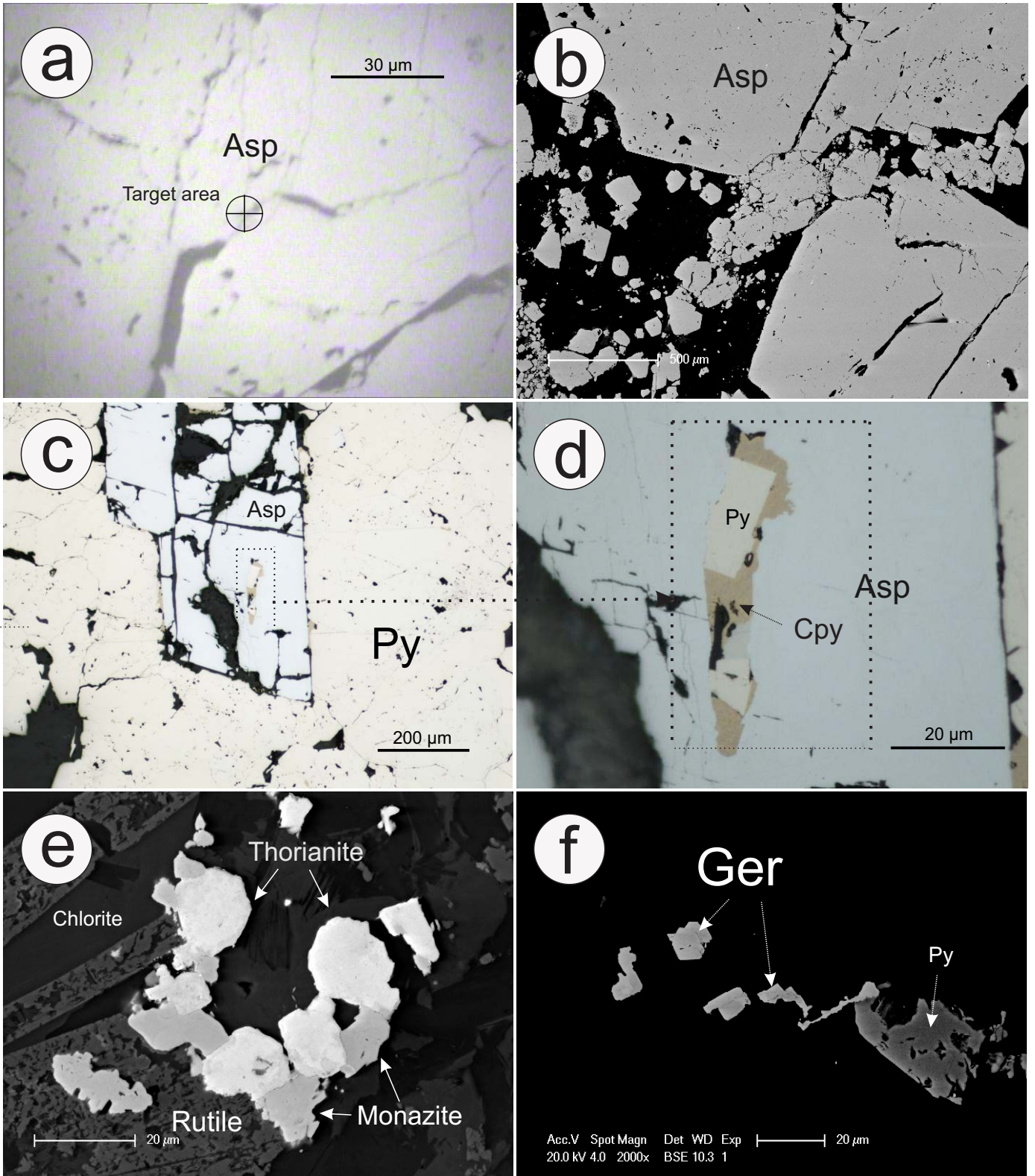


**Figure 9.** (a) Laser ablation target area within the fractured zone of an arsenopyrite grain (DM26, spot 13, which gave 4464 ppm Au). (b) BSE images showing overgrowth textures of arsenopyrite between two coarse euhedral arsenopyrite crystals. (c-d) Photomicrograph in reflected light illustrating (c) intergrowth of pyrite around fractured arsenopyrite. Dotted margin resembles area of focus with higher magnification in (d) Chalcopyrite intergrowth around pyrite margin; both are included within arsenopyrite (DM30). (e-f) BSE images showing (e) intergrown monazite and thorianite at the margin of elongate crystals of rutile, and (f) Gersdorffite intergrown with very fine-grained pyrite.

**FIGURE 10**

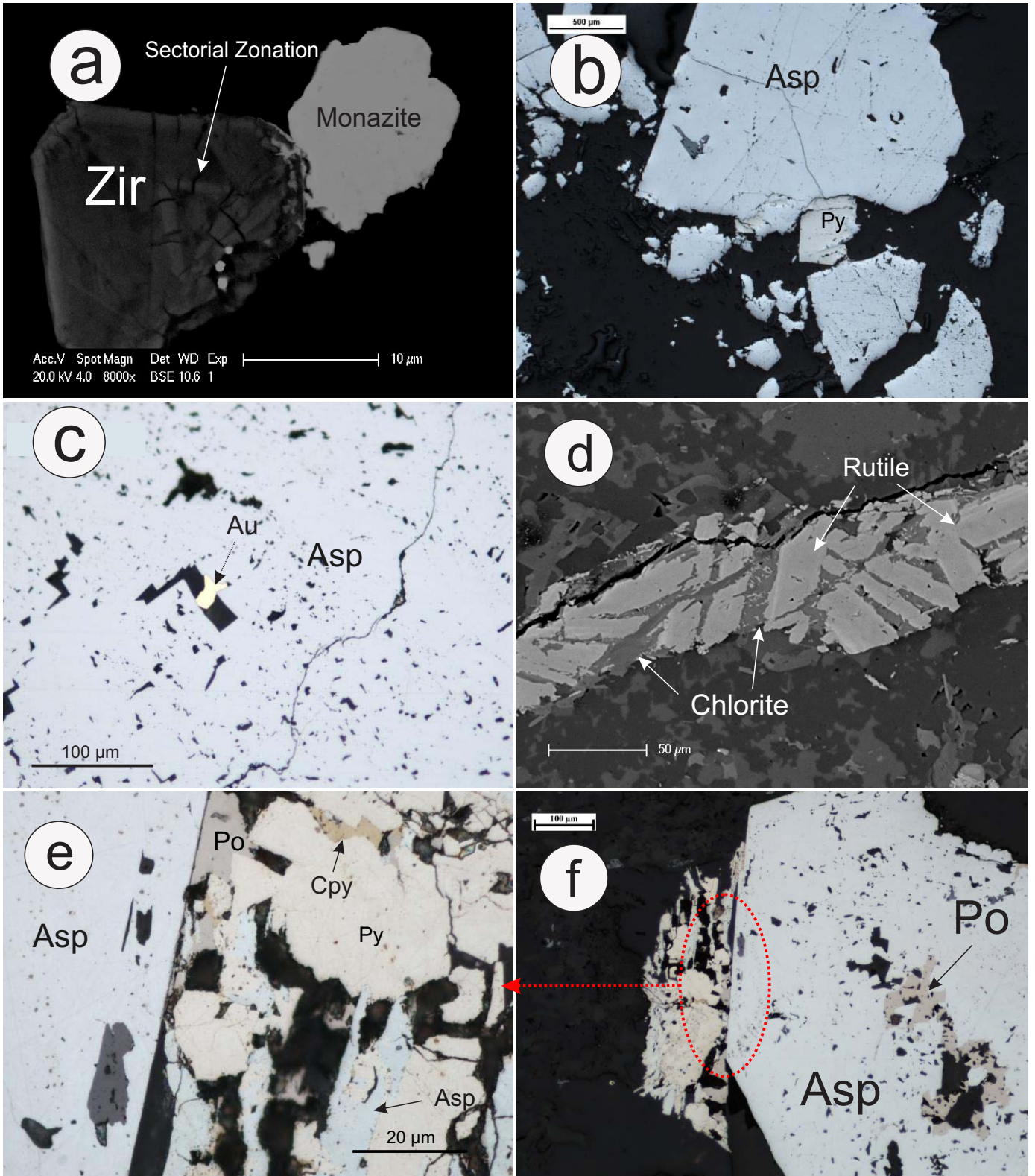


**Figure 10.** (a) BSE image of zircon displaying sectorial zoning. Adjacent is a grain of monazite intergrown within tiny inclusions and fractures of the zircon (DM38). (b-c) Photomicrograph in reflected light showing (b) high-relief arsenopyrite adjacent to intergrown pyrite (DM40), and (c) remobilised native gold grain within a gangue inclusion in porous arsenopyrite (DM40). (d) BSE image illustrating chlorite crystallizing within void spaces in a fractured grain of rutile (DM41). (e) Photomicrograph in reflected light showing arsenopyrite replacing pyrite. Intergrowth detail of pyrrhotite and chalcopyrite adjacent to pyrite and arsenopyrite (DM41). (f) BSE image of galena and monazite within a recrystallized grain of pyrite. Pyrrhotite is seen adjacent to the pyrite grain boundary (DM41).

**FIGURE 11**

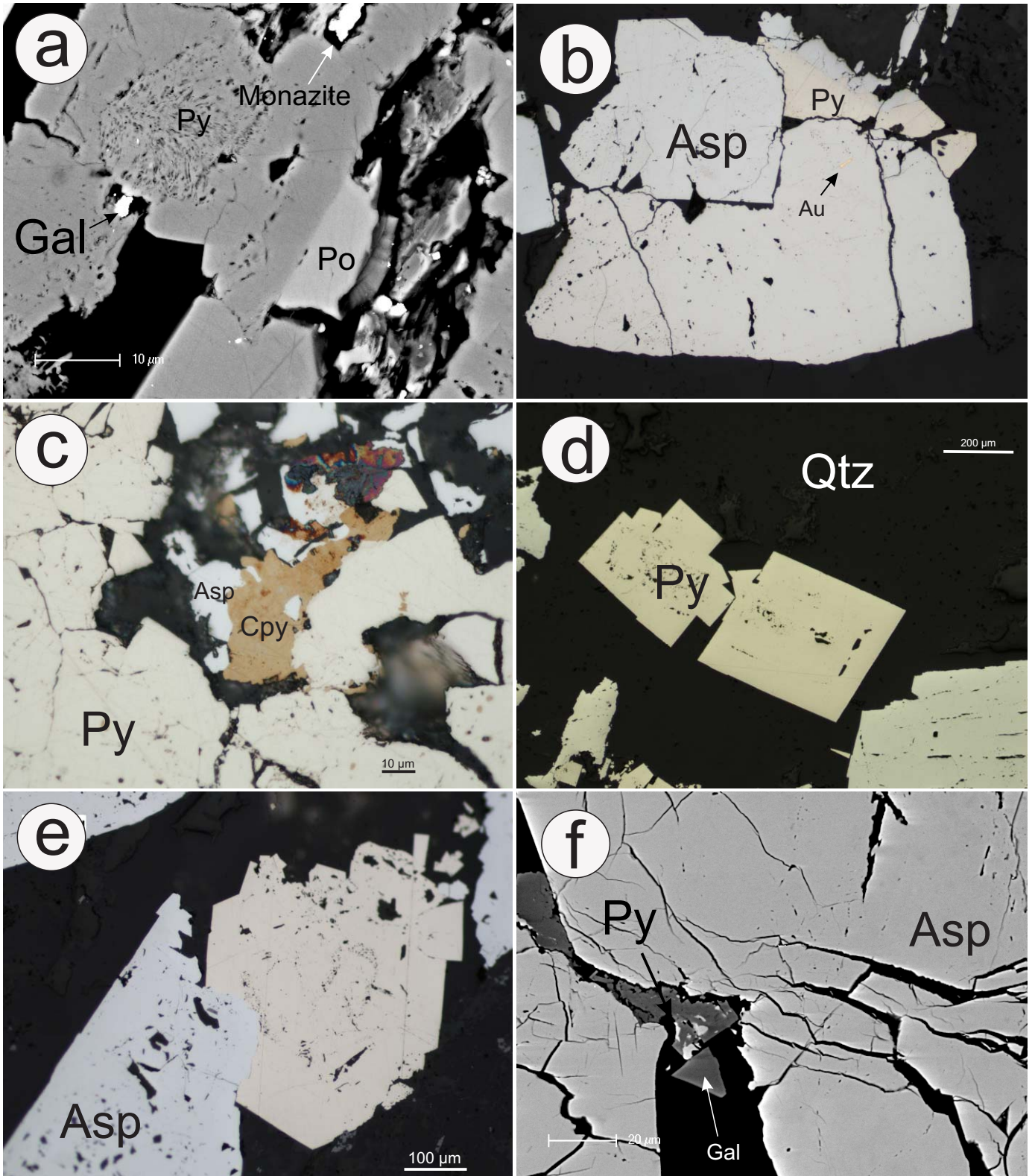


**Figure 11.** (a) BSE image of galena and monazite inclusions of pyrite overgrowth and pyrrhotite intergrowth. (b-e) Photomicrographs in reflected light illustrating (b) Pyrite intergrowth with arsenopyrite grain consisting of Au inclusion. (c) Chalcopyrite overprint of arsenopyrite and intergrowing with anhedral coarse grain pyrite. (d) Overgrowth pyrite grains with typical cubic textures. (e) Porous arsenopyrite grain overprinting pyrite overgrowth. (f) BSE image showing (f) Fractured coarse arsenopyrite grain with adjacent euhedral pyrite grain with galena inclusions.



**FIGURE 12**

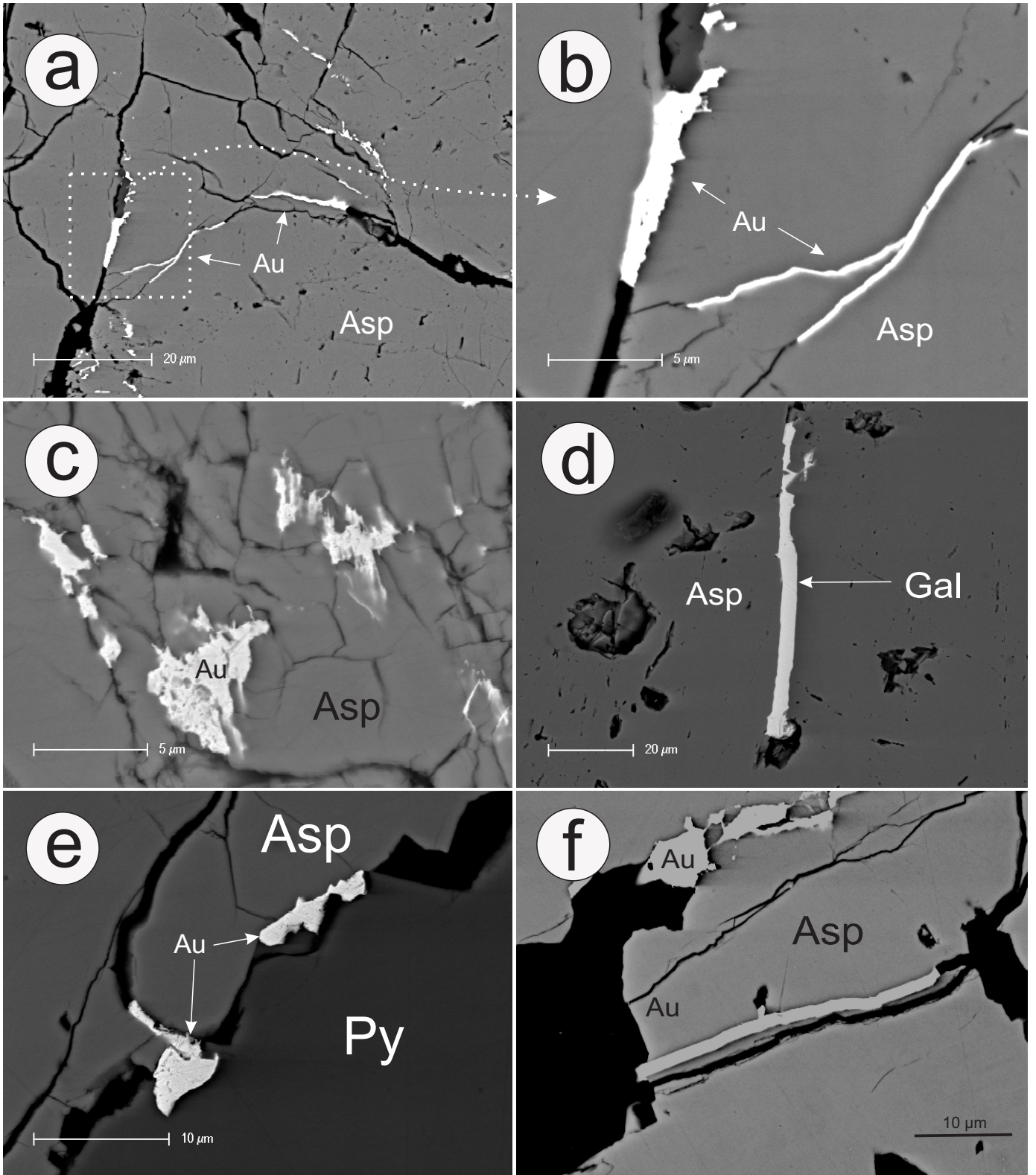


**Figure 12.** (a) BSE images showing (a) Gold veining within arsenopyrite fractures; the area marked by the dotted line is shown at higher magnification in (b). (c) Gold within a brecciated zone of arsenopyrite. (d) Microvein of galena in arsenopyrite. (e) Grain-scale remobilised gold within a fracture in arsenopyrite and at the mutual boundary between pyrite and arsenopyrite. (f) Remobilised gold forming a narrow vein within fractures and voids in arsenopyrite.

**FIGURE 13**

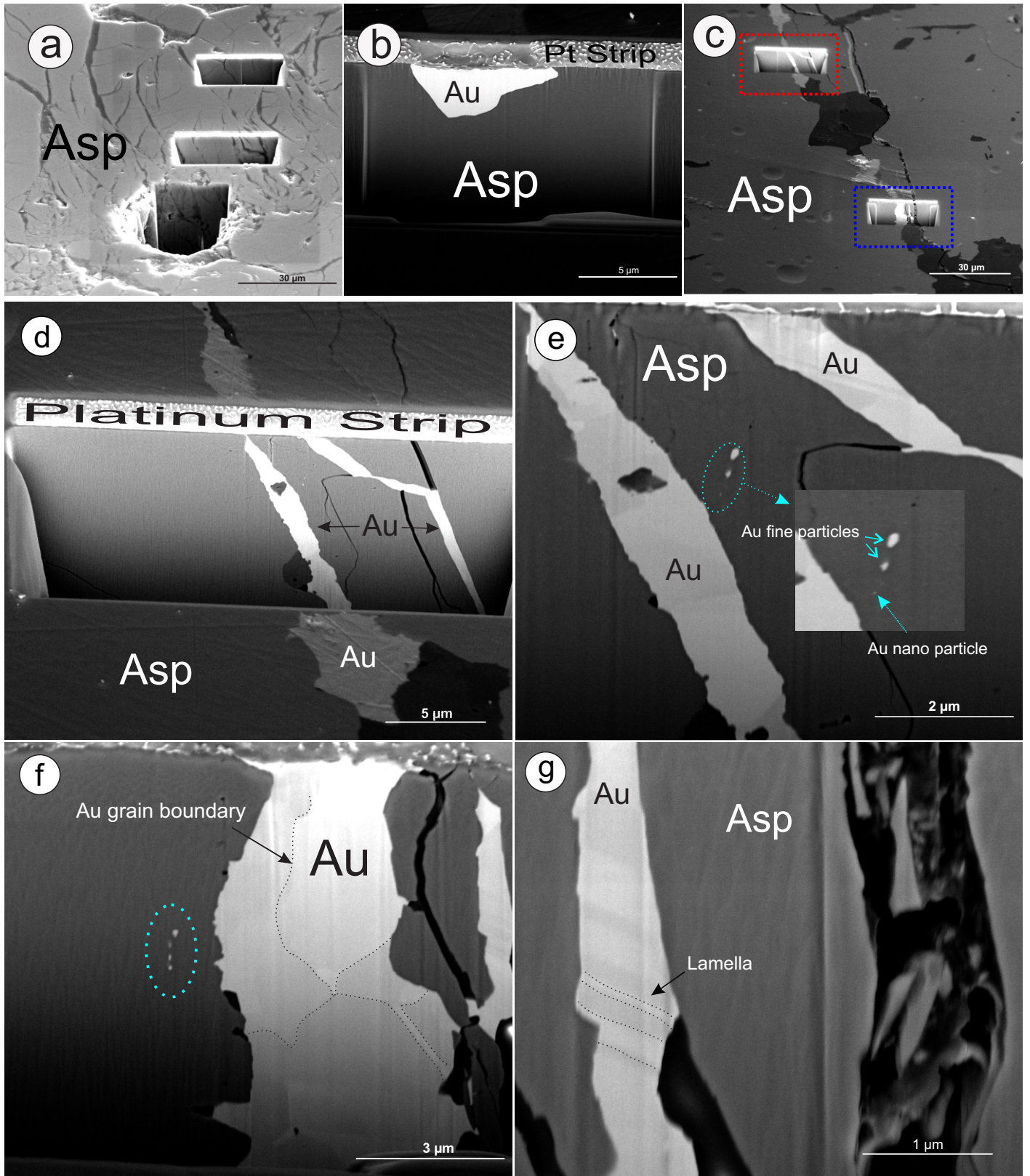
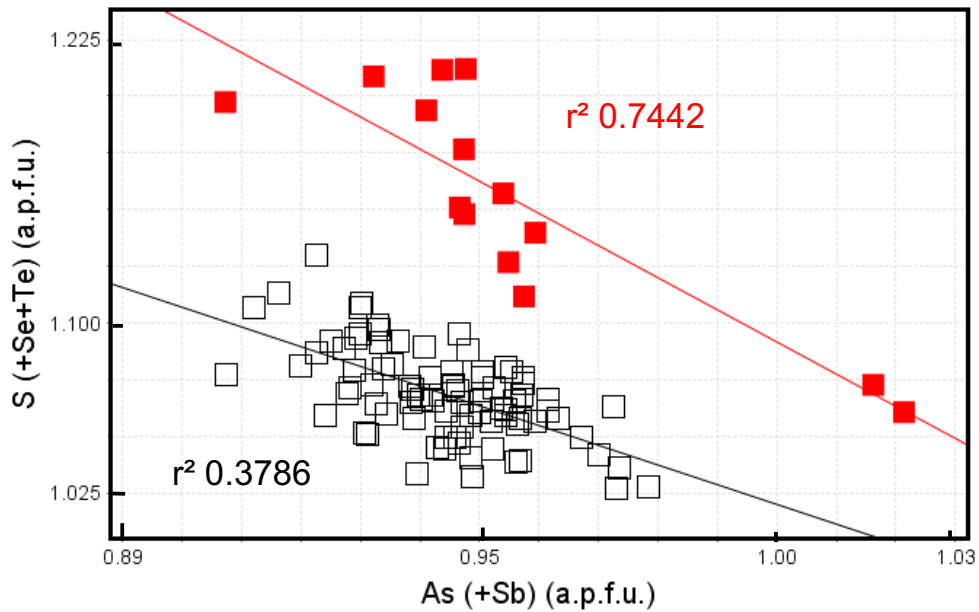


**Figure 13.** (a) High-resolution Focussed Ion Beam (FIB)-SEM secondary electron (SE) images illustrating (a) FIB cuts within brecciated arsenopyrite close to a LA-ICP-MS crater. (b) FIB-SEM trench crosscutting a micron-sized gold grain within arsenopyrite. (c) FIB-SEM trenches intersecting microveinlets carrying remobilised gold within fractured arsenopyrite. The trench identified by the red dotted line is magnified in (d) and (e), and the trench identified by the blue dotted line is magnified in (f) and (g). (d) Microveinlets of gold within fractured zones of arsenopyrite. (e) Further magnification showing nanoparticles and fine particles of gold. Note that the gold displays different shades in the image suggesting this is an aggregate of different gold grains. (f) Gold microveining with marked boundaries illustrating an aggregate of gold crystals amalgamated together. Note the fine particles adjacent the vein. (g) Microveinlet of gold with marked boundaries showing twin lamellae.

**FIGURE 14**

**(A)**



**(B)**

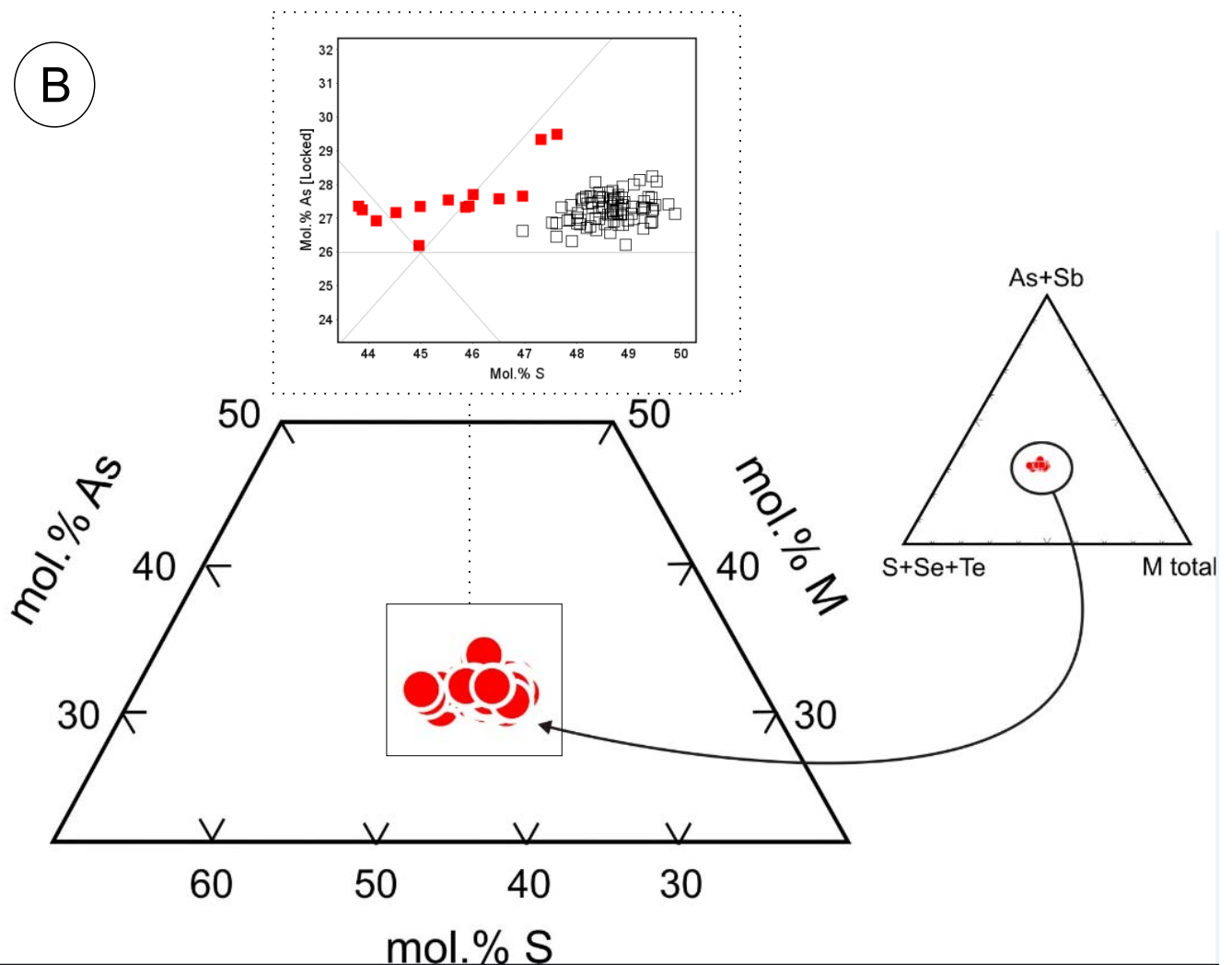


**Figure 14. (a)** Plot of As(+Sb) vs. S(+Se+Te) plot for arsenopyrite showing compositional variation as determined by EPMA expressed in atoms per formula unit (a.p.f.u.). Only two marked points lie 'above' the ideal FeAsS composition as shown on the vertical axis. Note that the main cluster is slightly depleted in S, whereas the adjacent group of points shows a systematic increase in S. **(b)** Ternary plot of (As+Sb) – (S+Se+Te) – M total (where M= Fe+Co+Ni+Cu) showing the composition of analysed arsenopyrite in terms of mol% and trends among the dataset. Note the homogenous increase in S from sample (DM 38), resembling S substitution for Fe in the FeAsS site.

**FIGURE 15**

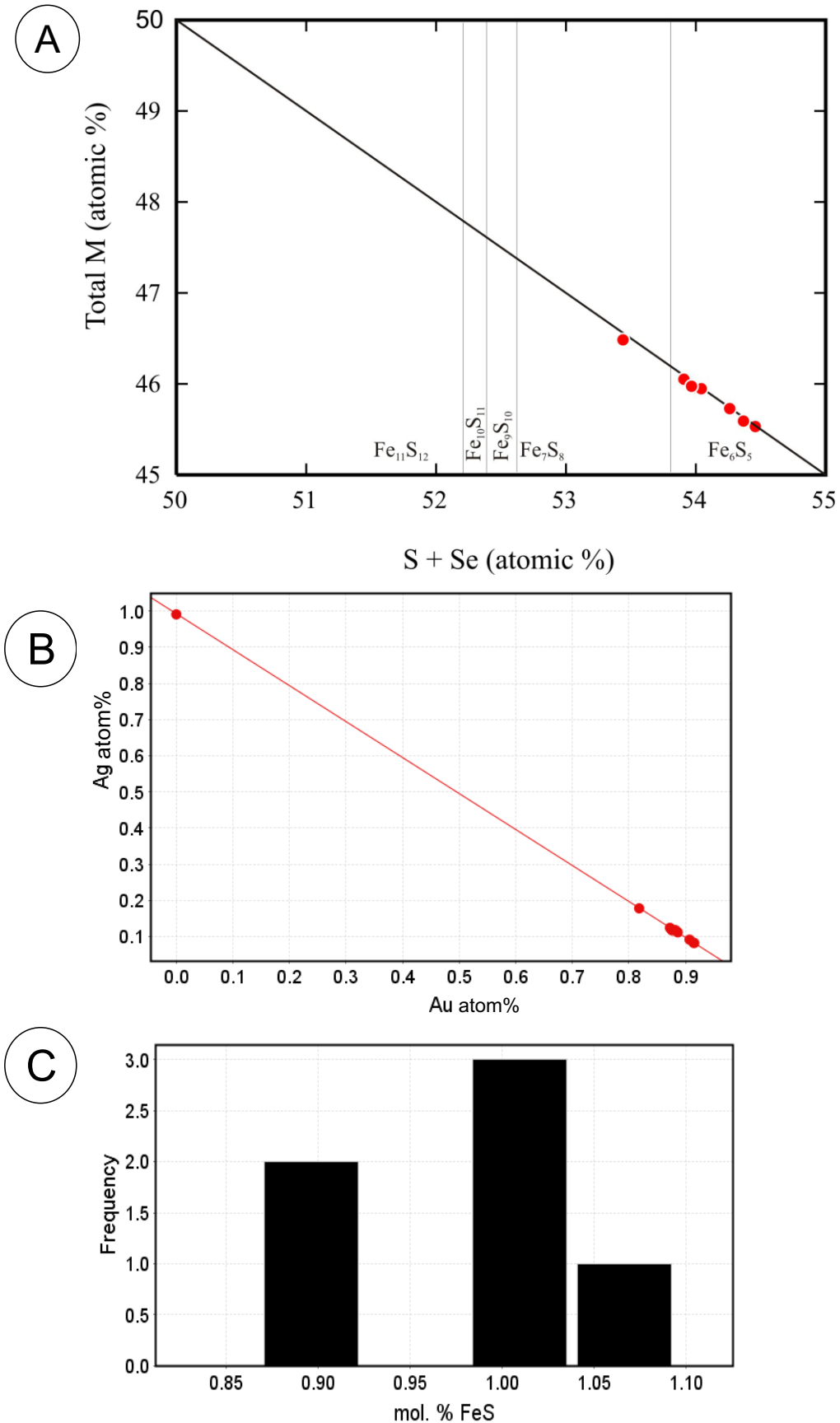


**Figure 15. (a)** Binary plot of atom. % Total M (Fe+Co+Ni+Cu) vs. S (+Se) for pyrrhotite as determined by EPMA. Note that all pyrrhotite compositions are S-poor (within the fields of Fe<sub>7</sub>S<sub>8</sub> and Fe<sub>6</sub>S<sub>5</sub> only). **(b)** Native Au vs. Ag binary plot determined by EPMA analysis measure by atom% clearly showing majority of grains analysed are Au with the exception of the Ag outlier. **(c)** Mol% FeS histogram of sphalerite with adjusted log axis on horizontal axis measured by EPMA. Note that the population varies with a mean of 9.8 mol% FeS, which gives unrealistically high inferred pressures in contrast to the mild metamorphism at Oberon.

**FIGURE 16**

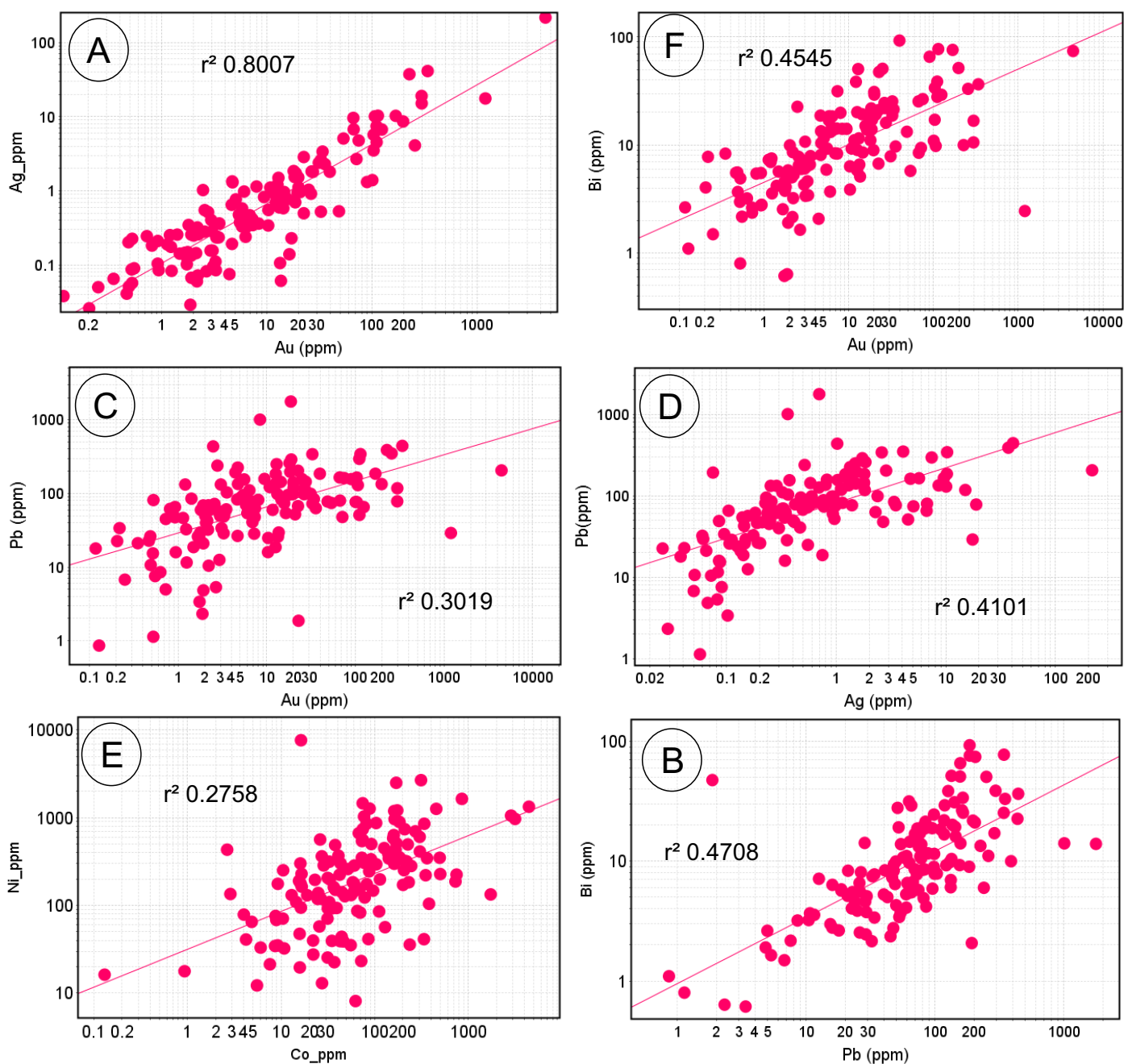


**Figure 16.** (a) Binary element plots illustrating trends and regression lines in the trace element data obtained by LA-ICP-MS for arsenopyrite. (a) Strong positive correlation of Au vs. Ag as expected between the two precious metals. (b) Pb vs. Bi plot showing a positive correlation; both metals may be incorporated into the arsenopyrite crystal lattice in solid solution. (c) Pb vs. Au plot shows a consistent but rather weak positive correlation; outliers are strongly enriched in both metals, presumably as nanoparticulate galena and native gold. (d) Pb vs. Ag plot showing a similar but slightly stronger positive correlation (higher  $r^2$ ). (e) Ni vs. Co plot shows that both metals have a weak positive correlation, although arsenopyrite is far more enriched in Ni than Co. (f) Bi vs. Au plot reveals a weak positive correlation (low  $r^2$ ); most outliers are far more enriched with Au than Bi.

**FIGURE 17**

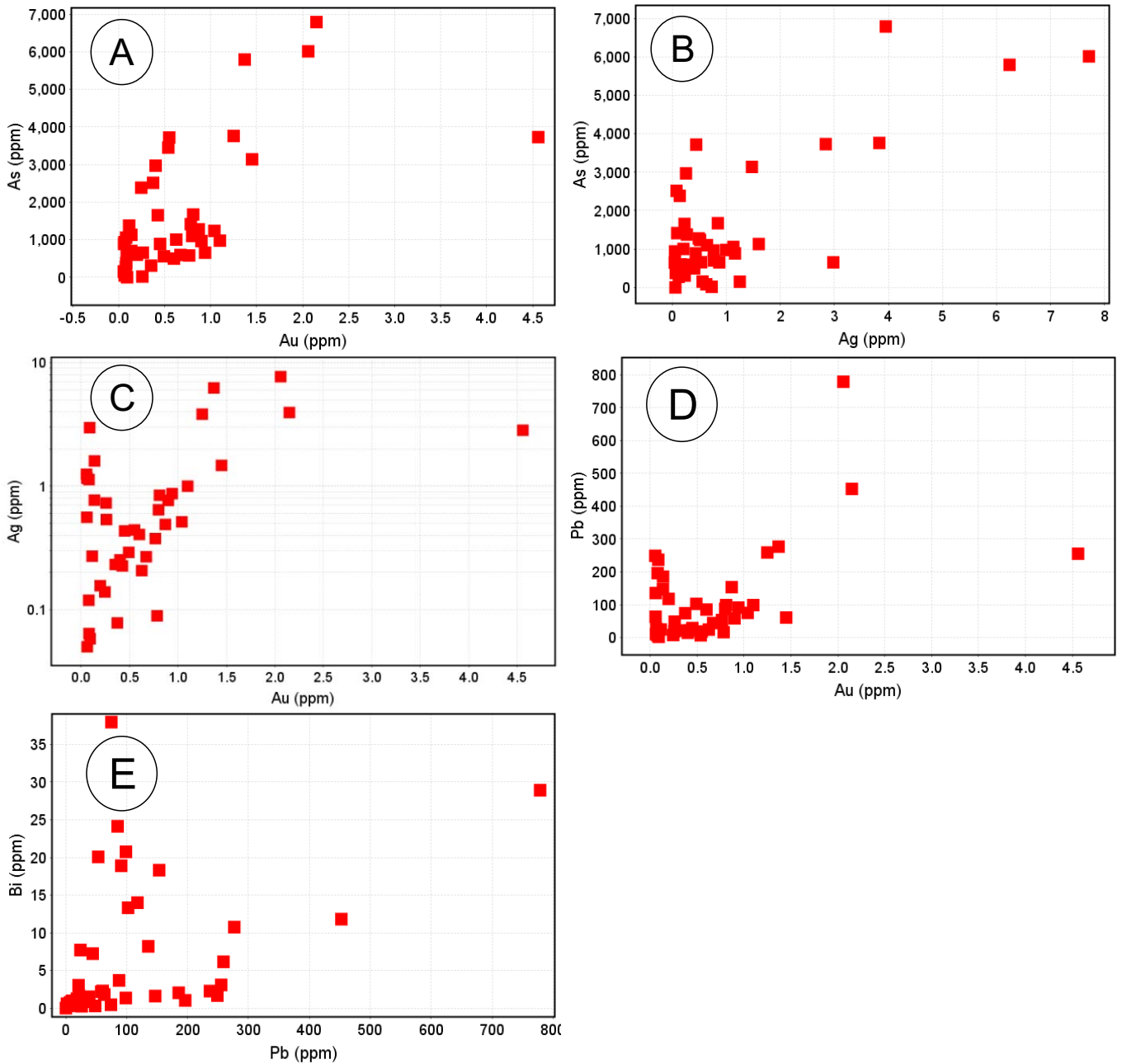


**Figure 17.** (a) Binary element plots showing trends in the trace element data obtained by LA-ICP-MS for pyrite. (a) As vs. Au plot revealing a large cluster with only a very weak positive correlation between the two elements. Outliers with high As and Au give an exponential and far stronger positive correlation. (b) As vs. Ag plot showing negligible correlation, with the exception of some spots in which both elements are high. (c) Ag vs. Au plot showing two different trends, no correlation identified with the upper sequence pyrite and relatively strong positive correlation with exception of outliers. Note that Ag is more enriched in pyrite than Au. (d) Pb vs. Au plot showing two trends, one with a positive correlation and a second trend lacking any correlation. (e) Bi vs. Pb plot showing enrichment of Pb within arsenopyrite and a weak positive correlation between the two metals.

**FIGURE 18**

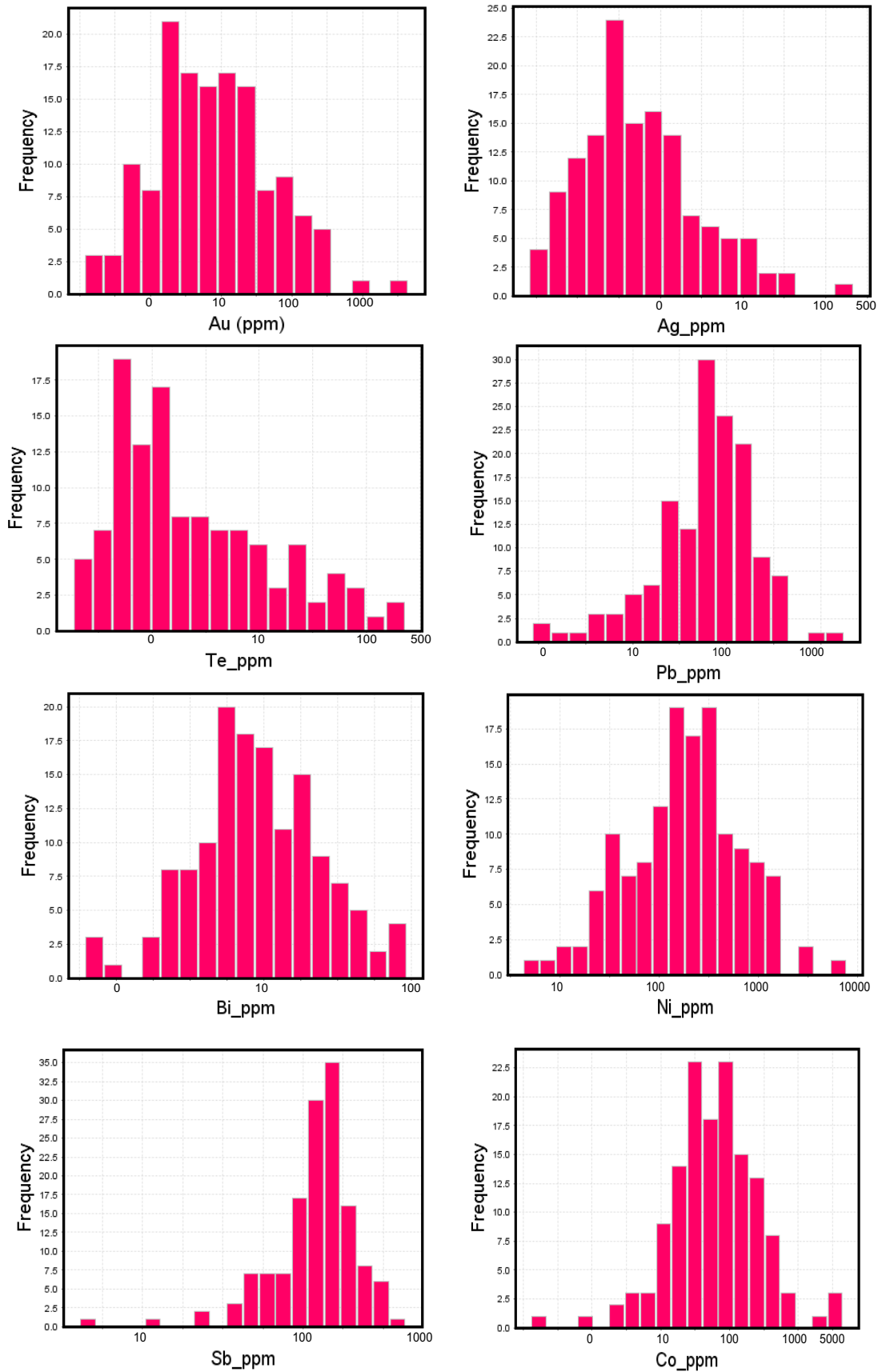


**Figure 18. (a)** Histograms (log 10 axis on horizontal axis) showing the distribution of Te, Bi, Au, Pb, Ag, Ni, Sb and Co concentrations within arsenopyrite as determined by LA-ICP-MS analysis. Note the similarities between trends of precious metals and Ni and Co.

**FIGURE 19**

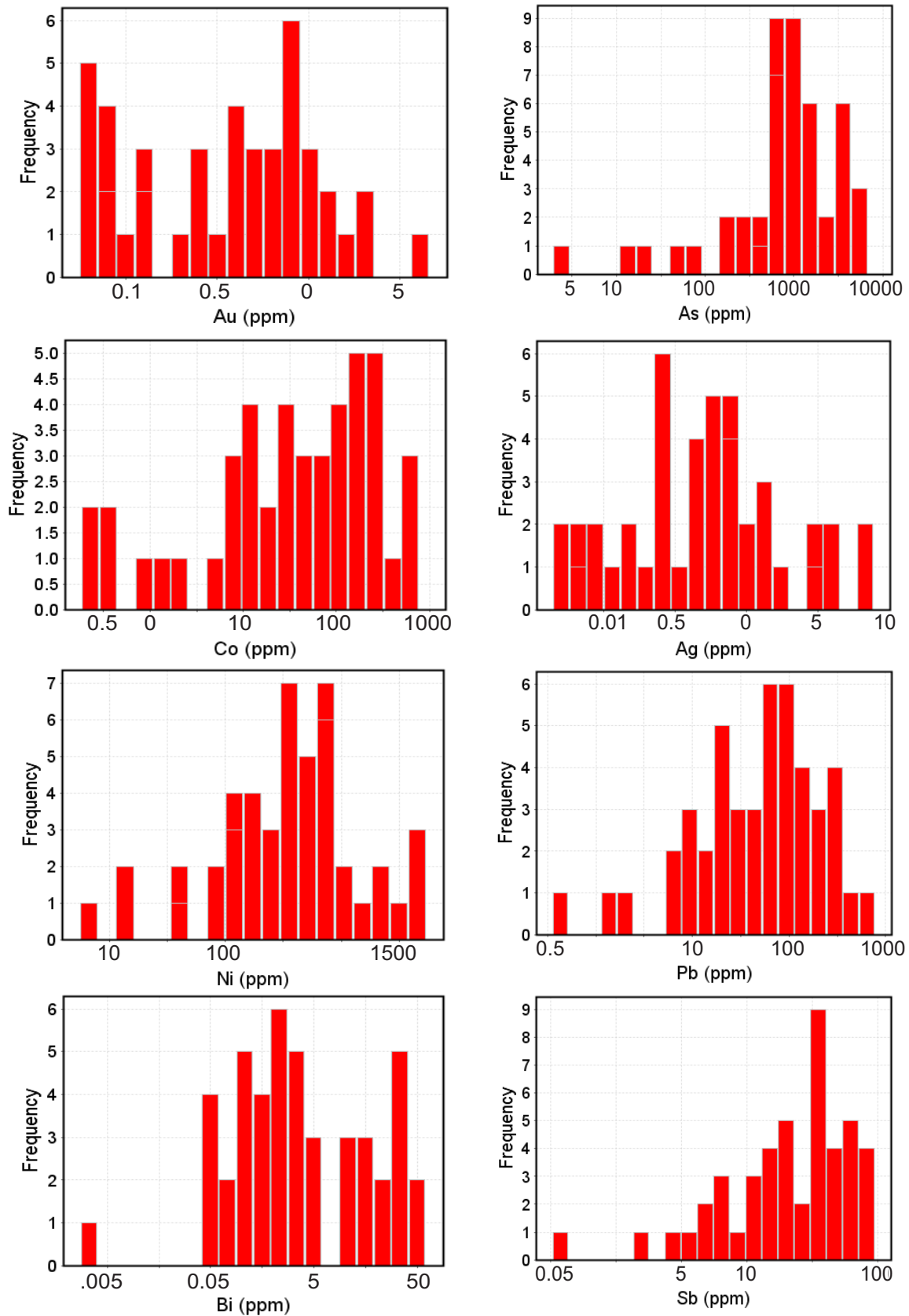


**Figure 19. (a)** Histograms (log 10 axis on horizontal axis) showing the distribution of Au, As, Co, Ag, Ni, Pb, Bi and Sb concentrations within pyrite as determined by LA-ICP-MS analysis. Note the similarities between the sub-populations, except for the Sb trend, showing a relatively positive skew in comparison to the precious metals.



**FIGURE 20**

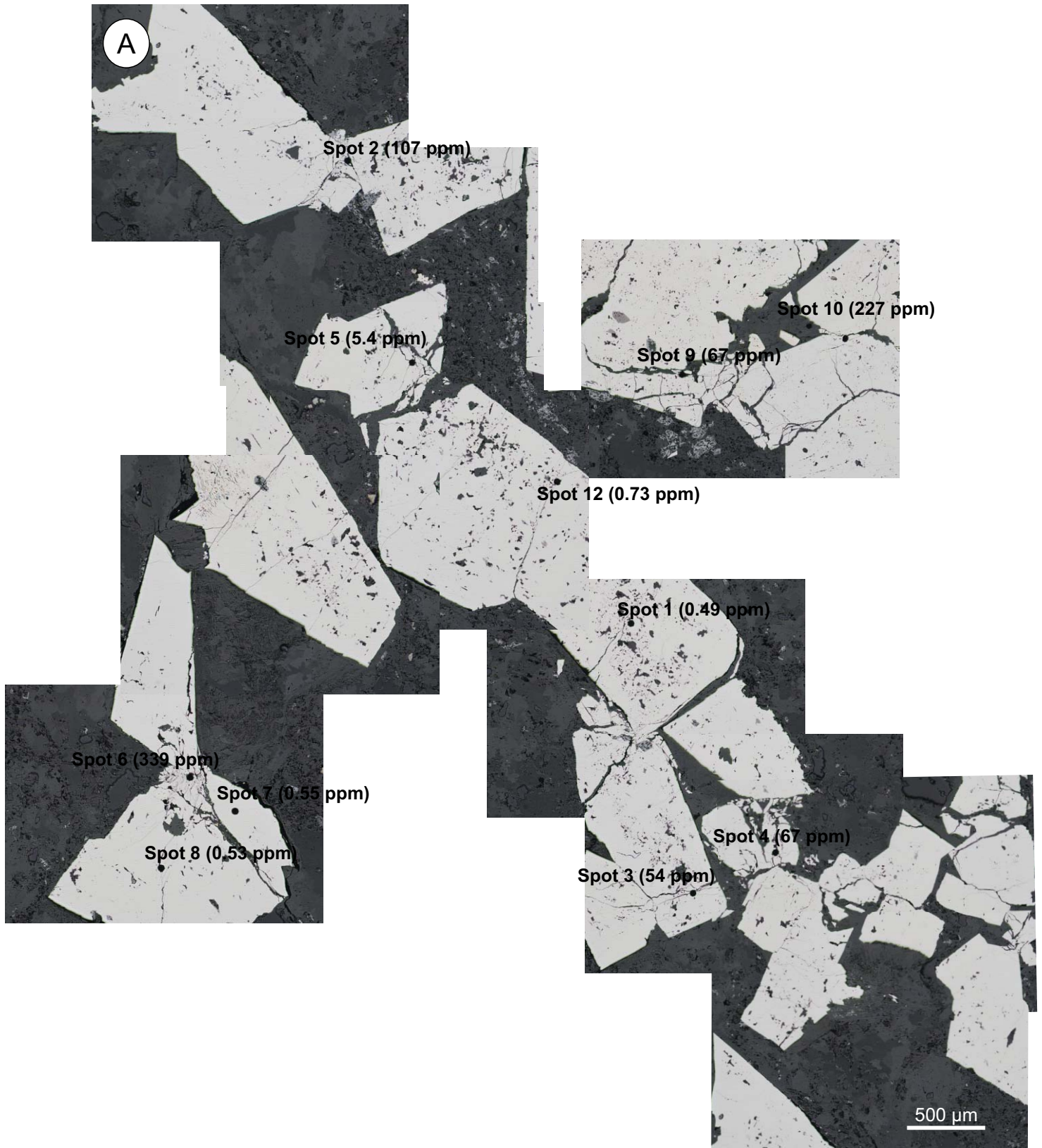
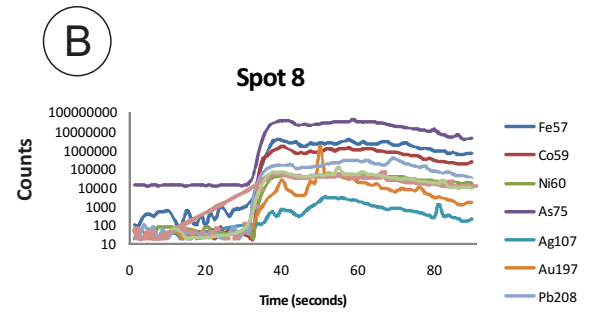
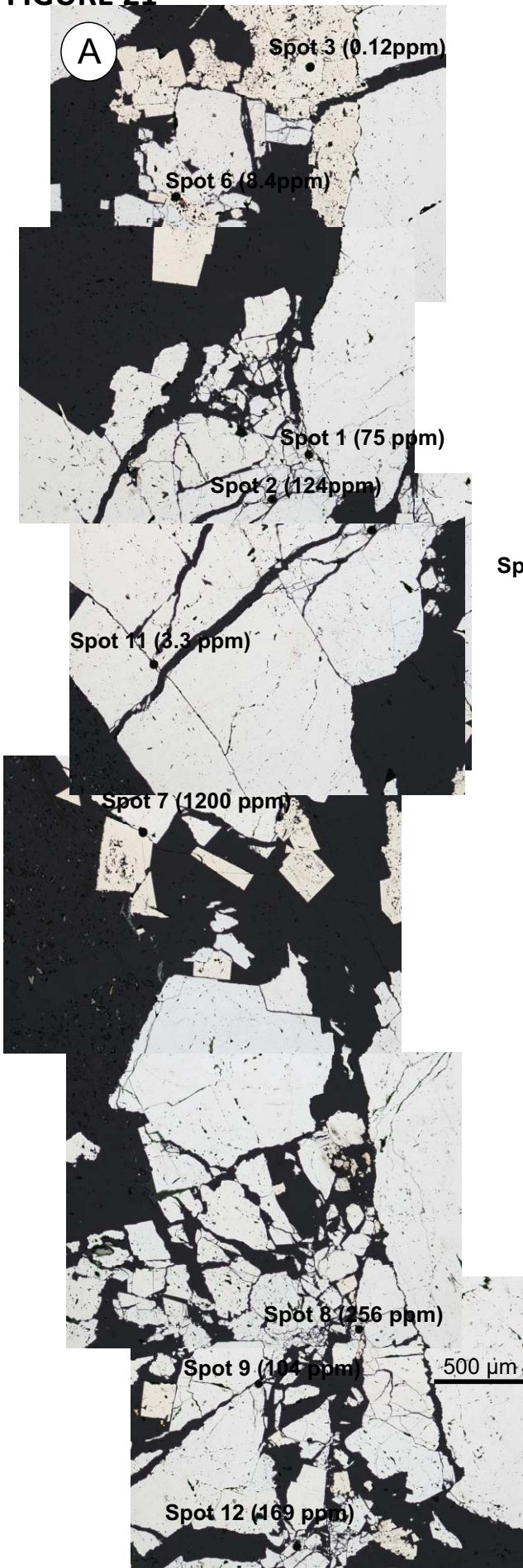


**Figure 20.** Reflected light microscope images assembled to indicate the distribution of grains of pyrite analysed by LA-ICP-MS and the Au concentrations determined. Marks showing the target areas of each spot ablation.

FIGURE 21



Spot 10 (6.4 ppm)

**Figure 21. (a)** Composite reflected-light microscope images showing the distribution of selected LA-ICP-MS spot analyses and Au concentrations within each spot. Note that selection of analysed spots was biased towards fractured and brecciated arsenopyrite to verify that higher Au could be correlated with such textures. **(b)** Time-resolved LA-ICP-MS depth profile of spot 8 (256 ppm) showing inconsistency in Au concentration, with a large peak recorded in the spectra thus indicating the presence of fine particles or nanoparticles of gold.

**FIGURE 22**

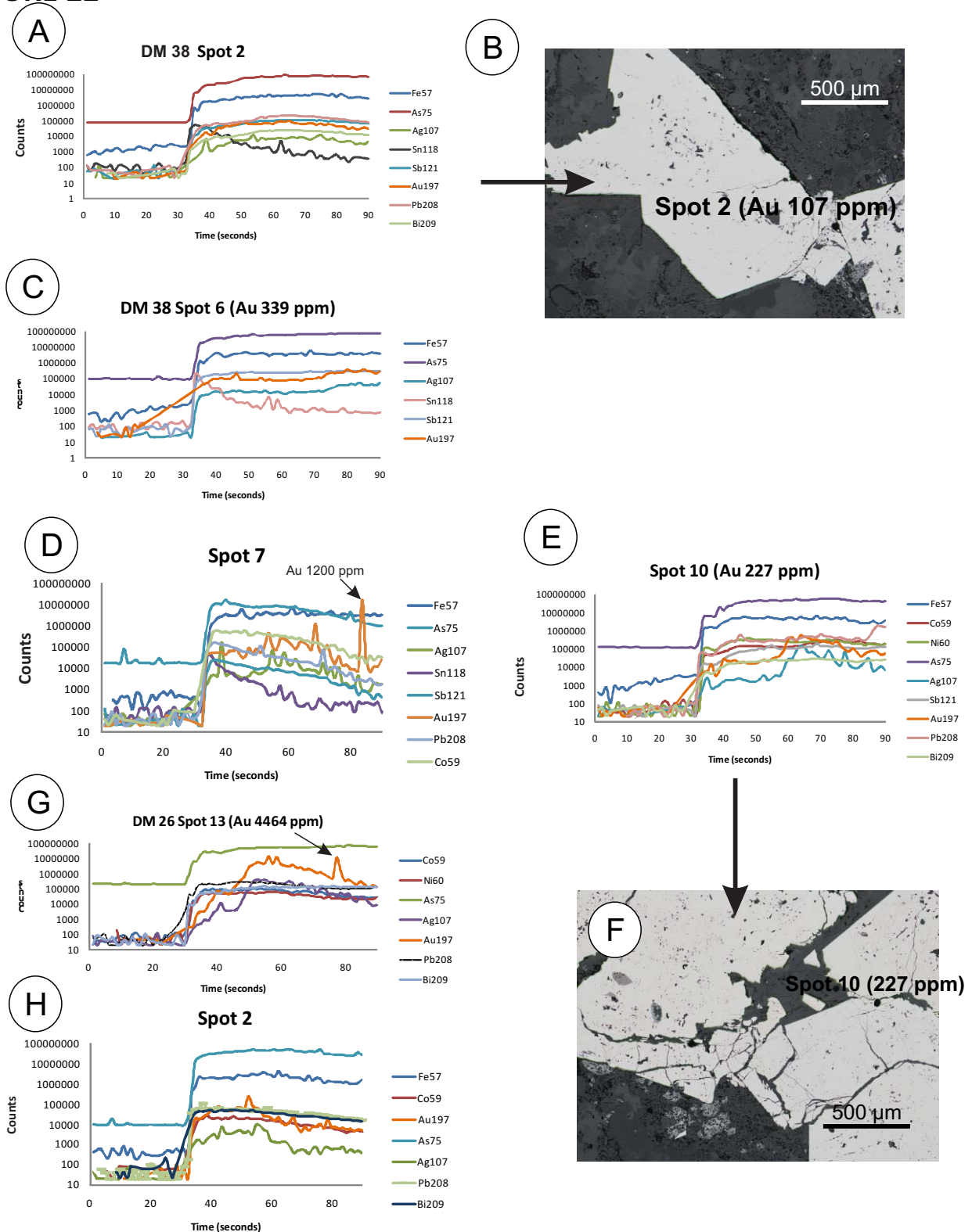


**Figure 22.** (a) Time-resolved LA-ICP-MS depth profile for arsenopyrite (DM38 spot 2) showing flat spectra, thus suggesting that all elements, with the exception of Sn, are in solid solution. (b) Photomicrograph in reflected light showing the ablated area of sample DM38 spot 2, a brecciated zone between two coarser grains of arsenopyrite. (c) Time-resolved LA-ICP-MS depth profile for spot 6 (sample DM38) showing flat spectra of elements with exception of Sn. (d) Time-resolved LA-ICP-MS depth profile for spot 7 (sample DM16) showing a noisy spectra of Au and Ag explained by the presence of nanoparticles and fine particles of gold. (e) Time-resolved LA-ICP-MS depth profile for spot 10 (sample DM38) showing a relatively noisy spectra for Au and Ag. (f) Photomicrograph in reflected light of spot 10, sample DM38 at the fractured margin of a giant arsenopyrite grain. (h) Time-resolved LA-ICP-MS depth profile for spot 2, sample DM16, showing distinct nanoparticles of Au and Ag near the surface of the ablated arsenopyrite which contrast with the relatively flat spectra towards the end.

**Table 1.** Index of samples from drillhole TID0065

Sample	Depth (m)	Description	R.L.	SEM	LAICPMS	FIB	EPMA
DM1	407	Vein quartz within dark sandstone unit with pyrite					
DM2	444	Fine grained graphitic beds with pyrite veining					
DM3	444				✓		
DM4	448	Graphitic beds; pyrite veining within laminated bands and microfractures					
DM5	454	Boudin chert unit with py veining within laminated bands and vein quartz					
DM6	455						
DM7	465	Pyrite abundant within matrix of boudin chert, mimicking chert and schist lenses					
DM8	468	Pyrite veining within microfractures and imitating rock fabric					
DM9	476	Large pyrite veining/overgrowth crystals within sandstone matrix					
DM10	645	Pyrite and pyrrhotite within vein quartz and sandstone matrix	✓		✓		
DM11	669	Arsenopyrite within quartz vein and chlorite altered matrix					
DM12	681	Pyrite veining along fine grained fabric with elongate arsenopyrite crystal against fabric					
DM13	689	Pyrite association within large arsenopyrite crystals within vein quartz			✓		✓
DM14	703	Pyrite and arsenopyrite within vein quartz; pyrrhotite along microfractures					
DM15	713	Arsenopyrite and pyrite within quartz vein nad matrix, pyrrhotite veining within matrix	✓	✓			
DM16	715	Pyrite and arsenopyrite overprinting textures within matrix and vein quartz. Au present	✓	✓	✓		✓
DM17	716	Fine grained pyrite and arsenopyrite within quartz network and matrix					
DM18	739	Coarse arsenopyrite within vein quartz and porous fine grained arsenopyrite within matrix	✓	✓	✓		✓
DM19	740	Coarse grained arsenopyrite with reworked carbonaceous vein quartz	✓		✓		✓
DM20	745	Pyrite abundant within vein quartz within carbonaceous matrix					
DM21	754	Fine grained arsenopyrite within fine grained matrix					
DM22	756	Allotriomorphic pyrrhotite within quartz vein network	✓	✓			✓
DM23	780	Coarse grained arsenopyrite within vein quartz and smaller grains within adjacent fine grained matrix	✓		✓		✓
DM24a	781	Arsenopyrite along margin vein quartz splaying into adjacent matrix	✓		✓		✓
DM24b		Pyrite and arsenopyrite within of vein quartz, some arsenopyrite splaying into matrix	✓				✓
DM25	786	Idiomorphic arsenopyrite grains within vein quartz and matrix					
DM26	793	Arsenopyrite abundant within matrix consisting of interlayers of fine and coarse grained rock			✓		
DM27	797	Pyrite and pyrrhotite veining mimicking mircorfractures within fine grained matrix					
DM28	812	Pyrite overgrowth within vein quartz and arsenopyrite within fine grained matrix and heavily reworked and boudinaged vein quartz network.			✓		
DM29	813	Arsenopyrite within brecciated textures of reworked vein quartz					✓
DM30	814	Discontinuous pyrite veining along carbonaceous vein quartz network	✓	✓	✓		
DM31	816	Pyrite within vein quartz with irregular texture from breccia clasts within the quartz network					
DM32	817	Pyrite within vein quartz with intergrowth textures around tiny quartz clasts					
DM33	817	Pyrite within reworked vein quartz, with irregular grain boundaries					
DM34	853	Arsenopyrite within edges of reworked vein quartz splaying into adjacent matrix					
DM35	853	Pyrite veining along microfracture intersecting coarse grained matrix					
DM36	855	Idiomorphic arsenopyrite grains within re-deformed interlayered fine grained matrix and vein quartz					
DM37	855	Idiomorphic arsenopyrite within deformed brecciated vein quartz and fine grained matrix			✓		✓
DM38	858	Arsenopyrite within reworked deformed and brecciated vein quartz network		✓	✓	✓	✓
DM39	861	Arsenopyrite anhedral grains mimicking clasts within vein quartz and idiomorphic textures within fine grained matrix					
DM40	863	Brecciated arsenopyrite grains within reworked vein quartz network	✓				
DM41	863	Idiomorphic arsenopyrite grains within reworked vein quartz and adjacent fine grained matrix	✓	✓	✓		✓
DM42	881	Idiomorphic pyrite and arsenopyrite grains mimicking coarse grains within re-deformed vein quartz					
DM43	883	Idiomorphic coarse arsenopyrite grains along margin of vein quartz					

**Table 2:** Summary of Electron Microprobe analyses of Arsenopyrite (FeAsS)

<i>Arsenopyrite (FeAsS)</i>																								
wt%	Sample																							
	23DM		18DM		38DM		23DMLine		24bDM		16DM		41DM		37DM		13DM		29DM		24aDM		19DM	
	mean	sd	mean	sd	mean	sd	mean	sd	mean	sd	mean	sd	mean	sd	mean	sd	mean	sd	mean	sd	mean	sd	mean	sd
<b>Cu</b>	0.02	0.03	0.02	0.02	0.02	0.02	0.01	0.02	0.04	0.05	0.06	0.05	0.01	0.02	0.04	0.03	0.04	0.03	0.03	0.03	0.01	0.01	0.02	0.03
<b>Fe</b>	34.90	0.30	34.72	0.75	30.90	3.62	34.27	0.45	33.96	1.03	34.31	0.55	32.18	2.99	34.30	0.41	35.04	0.46	34.65	0.28	34.67	1.04	28.36	3.97
<b>Co</b>	0.00	0.00	0.00	0.01	0.00	0.01	0.00	0.00	0.00	0.00	0.00	0.00	0.00	0.01	0.00	0.00	0.00	0.00	0.00	0.01	0.02	0.04	0.00	0.00
<b>Ni</b>	0.01	0.01	0.03	0.06	0.02	0.03	0.02	0.01	0.01	0.01	0.00	0.00	0.02	0.03	0.02	0.03	0.02	0.02	0.03	0.02	0.09	0.16	0.01	0.01
<b>Sb</b>	0.015	0.018	0.030	0.020	0.013	0.019	0.023	0.022	0.009	0.015	0.002	0.005	0.017	0.021	0.027	0.023	0.018	0.027	0.017	0.019	0.006	0.009	0.014	0.025
<b>As</b>	43.61	0.52	42.80	0.54	41.55	2.99	43.33	0.25	42.61	0.79	43.58	0.53	41.96	2.14	43.80	0.29	44.01	0.34	43.10	0.44	43.19	0.67	39.38	3.45
<b>Sb</b>	20.75	0.26	20.86	0.57	20.40	0.58	21.00	0.34	20.81	0.43	20.73	0.29	20.71	0.64	20.84	0.22	20.48	0.30	21.21	0.35	20.69	0.43	19.30	1.86
<b>Se</b>	0.34	0.05	0.29	0.06	0.39	0.08	0.31	0.11	0.30	0.07	0.29	0.06	0.36	0.06	0.31	0.04	0.32	0.09	0.38	0.04	0.34	0.06	0.31	0.14
<b>Total</b>	<b>99.63</b>	<b>0.31</b>	<b>98.75</b>	<b>1.06</b>	<b>93.29</b>	<b>6.33</b>	<b>98.96</b>	<b>0.59</b>	<b>97.74</b>	<b>1.41</b>	<b>98.97</b>	<b>0.63</b>	<b>95.26</b>	<b>5.54</b>	<b>99.34</b>	<b>0.67</b>	<b>99.94</b>	<b>0.46</b>	<b>99.41</b>	<b>0.58</b>	<b>99.02</b>	<b>1.51</b>	<b>87.40</b>	<b>8.88</b>
Formulae 3 a.p.f.u.																								
<b>Cu</b>	0.000	0.001	0.001	0.000	0.000	0.001	0.000	0.000	0.001	0.001	0.002	0.001	0.000	0.000	0.001	0.001	0.001	0.001	0.001	0.000	0.000	0.001	0.001	0.001
<b>Fe</b>	0.994	0.007	0.995	0.017	0.932	0.059	0.980	0.007	0.978	0.016	0.984	0.011	0.951	0.040	0.980	0.007	0.999	0.010	0.985	0.010	0.993	0.023	0.913	0.045
<b>Co</b>	0.000	0.000	0.000	0.000	0.000	0.000	0.000	0.000	0.000	0.000	0.000	0.000	0.000	0.000	0.000	0.000	0.000	0.000	0.000	0.000	0.001	0.000	0.000	0.000
<b>Ni</b>	0.000	0.000	0.001	0.002	0.001	0.001	0.000	0.000	0.000	0.000	0.000	0.000	0.001	0.001	0.001	0.001	0.001	0.001	0.001	0.001	0.002	0.004	0.000	0.000
<b>M total</b>	0.995	0.007	0.997	0.018	0.933	0.059	0.981	0.007	0.979	0.016	0.985	0.012	0.952	0.039	0.982	0.007	1.000	0.010	0.987	0.010	0.996	0.024	0.914	0.045
<b>As</b>	0.944	0.013	0.932	0.015	0.955	0.022	0.942	0.012	0.833	0.308	0.950	0.013	0.945	0.012	0.951	0.008	0.953	0.010	0.931	0.008	0.940	0.010	0.968	0.032
<b>Sb</b>	0.000	0.000	0.000	0.000	0.000	0.000	0.000	0.000	0.000	0.000	0.000	0.000	0.000	0.000	0.000	0.000	0.000	0.000	0.000	0.000	0.000	0.000	0.000	0.000
<b>As+Sb</b>	0.945	0.013	0.933	0.015	0.955	0.022	0.943	0.011	0.833	0.308	0.950	0.013	0.945	0.012	0.951	0.008	0.954	0.010	0.931	0.008	0.941	0.010	0.968	0.033
<b>S</b>	1.053	0.012	1.065	0.021	1.103	0.075	1.070	0.009	1.182	0.311	1.059	0.015	1.094	0.037	1.060	0.007	1.040	0.012	1.074	0.013	1.056	0.021	1.111	0.058
<b>Se</b>	0.007	0.001	0.006	0.001	0.009	0.002	0.006	0.002	0.006	0.002	0.006	0.001	0.008	0.002	0.007	0.001	0.007	0.002	0.008	0.001	0.007	0.001	0.007	0.003
<b>S+Se+Te</b>	1.060	0.012	1.071	0.021	1.112	0.077	1.076	0.009	1.188	0.309	1.065	0.016	1.102	0.038	1.067	0.007	1.046	0.011	1.082	0.012	1.063	0.021	1.118	0.061
<b>Total</b>	<b>3.000</b>	<b>0.000</b>	<b>3.000</b>	<b>0.000</b>	<b>3.000</b>	<b>0.000</b>	<b>3.000</b>	<b>0.000</b>	<b>3.000</b>	<b>0.000</b>	<b>3.000</b>	<b>0.000</b>	<b>3.000</b>	<b>0.000</b>	<b>3.000</b>	<b>0.000</b>	<b>3.000</b>	<b>0.000</b>	<b>3.000</b>	<b>0.000</b>	<b>3.000</b>	<b>0.000</b>	<b>3.000</b>	<b>0.000</b>
<b>Fe+Co+Ni</b>	0.995	0.007	0.996	0.018	0.933	0.059	0.981	0.007	0.978	0.016	0.984	0.011	0.952	0.039	0.981	0.007	0.999	0.010	0.986	0.009	0.996	0.024	0.913	0.045





**Table 5:** Summary of Electron Microprobe analyses of Native Gold

(wt. %)	<i>Gold-Electrum (Au)</i>							
	<b>Sample</b>				13DM	29DM	24ADM	24ADM
	<b>23DM (n=3)</b>		<b>16DM (n=3)</b>					
	mean	sd	mean	sd				
<b>Ag</b>	4.58	0.18	7.02	0.24	6.45	10.71	6.33	6.00
<b>Te</b>	0.02	0.04	0.07	0.03	0.00	0.00	0.08	0.01
<b>Au</b>	89.49	9.05	94.05	0.59	93.27	89.76	83.77	81.82
<b>Hg</b>	0.00	0.00	0.00	0.00	0.00	0.00	0.00	0.00
<b>Bi</b>	0.23	0.10	0.17	0.20	0.21	0.44	0.51	0.65
<b>Total</b>	94.33	9.29	101.30	0.20	99.92	100.91	90.68	88.49
	<b>Fomula 1 a.p.f.u</b>							
<b>Au</b>	0.912	0.005	0.879	0.006	0.886	0.818	0.874	0.876
<b>Ag</b>	0.086	0.005	0.120	0.004	0.112	0.178	0.121	0.117
<b>Te</b>	<mdl	<mdl	-	-	<mdl	<mdl	<mdl	<mdl
<b>Hg</b>	<mdl	<mdl	-	-	<mdl	<mdl	<mdl	<mdl
<b>Bi</b>	0.002	0.001	0.001	0.002	0.002	0.004	0.005	0.007
<b>Total</b>	1.000	0.000	1.000	0.000	1.000	1.000	1.000	1.000
<b>Au fineness (% sd)</b>	0.912	4.5	0.879	5.6	0.886	0.818	0.874	0.876



**Table 6:** Summary of Electron Microprobe analyses of Sphalerite (ZnS)

	<i>Sphalerite (ZnS)</i>								
	Sample								
<b>wt%</b>	<b>22dmp1</b>	<b>22dmp2</b>	<b>22dmp3</b>	<b>22dmp4</b>	<b>22dmp5</b>	<b>22dmp6</b>	<b>29dmp10</b>	<b>19dmp3</b>	
<b>S</b>	33.11	32.76	32.64	32.62	39.05	38.96	32.98	27.72	
<b>Mn</b>	0.03	0.00	0.01	0.02	0.00	0.00	0.00	0.00	
<b>Fe</b>	6.11	6.05	6.14	4.47	58.69	59.14	6.24	3.09	
<b>Cu</b>	0.08	0.25	0.24	0.06	0.00	0.05	0.08	0.16	
<b>Zn</b>	58.94	59.14	59.19	60.75	0.00	0.00	58.80	45.05	
<b>Ag</b>	0.00	0.00	0.07	0.02	0.00	0.04	0.04	0.14	
<b>Cd</b>	0.12	0.09	0.02	0.06	0.00	0.00	0.09	0.10	
<b>In</b>	0.00	0.04	0.04	0.03	0.00	0.01	0.03	0.23	
<b>Sn</b>	0.00	0.00	0.00	0.03	0.07	0.04	0.03	0.00	
<b>Total</b>	<b>98.39</b>	<b>98.31</b>	<b>98.34</b>	<b>98.05</b>	<b>97.81</b>	<b>98.23</b>	<b>98.29</b>	<b>76.49</b>	
				<b>Formulae 2 a.p.f.u.</b>					
<b>Mn</b>	0.000	0.000	0.000	0.000	0.000	0.000	0.000	0.000	
<b>Fe</b>	0.107	0.106	0.108	0.079	0.926	0.931	0.109	0.069	
<b>Cu</b>	0.001	0.004	0.004	0.001	0.000	0.001	0.001	0.003	
<b>Zn</b>	0.881	0.887	0.888	0.916	0.000	0.000	0.881	0.854	
<b>Cd</b>	0.001	0.001	0.000	0.001	0.000	0.000	0.001	0.001	
<b>In</b>	0.000	0.000	0.000	0.000	0.000	0.000	0.000	0.002	
<b>Sn</b>	<b>0.000</b>	<b>0.000</b>	<b>0.000</b>	<b>0.000</b>	<b>0.000</b>	<b>0.000</b>	<b>0.000</b>	<b>0.000</b>	
<b>S</b>	<b>1.009</b>	<b>1.002</b>	<b>0.999</b>	<b>1.003</b>	<b>1.073</b>	<b>1.068</b>	<b>1.007</b>	<b>1.071</b>	
<b>Total M</b>	<b>0.991</b>	<b>0.998</b>	<b>1.001</b>	<b>0.997</b>	<b>0.927</b>	<b>0.932</b>	<b>0.993</b>	<b>0.929</b>	
<b>mol.%ZnS</b>	88.9	88.9	88.8	91.9	0.0	0.0	88.7	91.9	
<b>mol.%CdS</b>	0.1	0.1	0.0	0.1	0.0	0.0	0.1	0.1	
<b>mol.%FeS</b>	10.8	10.6	10.8	7.9	99.9	99.9	11.0	7.4	

**Table 7:** LA-ICPMS trace element data for pyrite

Element	As	V	Mn	Co	Ni	Cu	Zn	Se	Ag	Sb	Te	Au	Hg	Tl	Pb	Bi
<b>444m</b>																
DM3py1	151	0.37	11	0.86	37	44.2	16	38	1.3	44	<0.31	<b>0.06</b>	<0.12	0.28	249	1.7
DM3py2	19	2.5	17	0.20	5.5	7.2	6.3	46	0.73	21	<0.28	<b>0.26</b>	<0.10	1.01	19	0.4
DM3py3	82	1.7	7	10	12	70	3.3	38	0.63	13	<0.27	<b>&lt;0.04</b>	0.15	0.1	39	1.5
DM3py4	153	5.8	19	5.1	133	106	4.6	36	0.56	14	<0.29	<b>0.06</b>	0.12	0.22	63	1.8
DM3py5	654	9.3	22	8.4	44	4600	20	48	3.0	33	0.34	<b>0.09</b>	0.15	0.14	237	2.3
DM3py6	1056	0.15	8	0.37	14	22	1.0	25	1.1	40	0.29	<b>0.08</b>	0.12	0.15	196	1.0
DM3py7	1132	12	30	27	99	161	13	23	1.6	39	0.30	<b>0.14</b>	0.19	0.37	186	2.0
DM3py8	702	21	44	103	143	32	12	35	0.77	26	<0.32	<b>0.14</b>	0.27	0.27	147	1.6
DM3py9	887	19	32	27	234	201	23	28	1.2	33	0.91	<b>0.06</b>	0.22	0.52	136	8.2
<b>mean n=9</b>	537	8	21	20	80	583	11	35	1.2	29	-	<b>0.11</b>	0.18	0.34	141	2.3
<b>654m</b>																
DM10py1	16	0.14	2.1	310	135	<0.83	<1.3	4.3	<0.04	1.6	<0.27	<b>&lt;0.05</b>	0.21	<0.01	1.5	<0.01
DM10py2	582	<0.15	1.9	273	162	8	<2.2	3.9	0.38	67	<0.45	<b>0.77</b>	<0.26	<0.02	53	20
DM10py3	977	<0.14	3.6	606	707	60	<2.6	8.2	1.0	92	<0.44	<b>1.1</b>	0.27	0.41	99	21
DM10py4	1237	<0.11	2.7	595	610	33	2.1	8.7	0.51	65	<0.33	<b>1.0</b>	<0.18	0.03	75	38
DM10py5	594	<0.13	2.1	187	215	13	<0.93	8.9	0.27	50	<0.44	<b>0.67</b>	<0.20	0.03	44	7.2
DM10py6	1003	0.16	2.1	175	564	13	0.99	8.2	0.21	37	<0.37	<b>0.63</b>	0.31	<0.01	24	7.7
DM10py7	2	0.17	1.5	20	428	1.8	0.88	4.4	0.06	3.6	<0.32	<b>0.09</b>	<0.13	<0.01	2.0	0.58
DM10py8	600	1.13	2321	232	440	12	4.1	3.9	0.16	12	<0.35	<b>0.20</b>	0.18	0.05	118	14
DM10py9	1277	<0.21	3.6	775	617	49	1.9	12	0.49	94	0.87	<b>0.87</b>	0.35	0.06	154	18
DM10py10	559	0.14	2.3	399	129	15	<0.78	6.8	0.29	60	<0.37	<b>0.49</b>	<0.16	<0.02	103	13
DM10py11	498	0.12	3.7	276	303	24	1.6	9.7	0.41	45	<0.31	<b>0.60</b>	0.18	0.10	85	24
DM10py12	655	0.23	9.2	266	420	39	1.5	5.0	0.87	49	<0.35	<b>0.94</b>	0.31	0.60	91	19
<b>mean n=12</b>	667	0.3	196	343	394	24	1.9	7.0	0.42	48	-	<b>1</b>	0.26	0.18	71	17
<b>812m</b>																
DM28py1	3451	0.70	10	15	83	3.8	<1.8	9.7	<0.03	4.2	<0.22	<b>0.54</b>	<0.11	0.05	6.9	0.7
DM28py2	3137	7.0	52	78	1174	56	17	8.8	1.47	54	<0.30	<b>1.5</b>	<0.13	2.8	61	2.3
DM28py3	1100	4.0	20	98	199	116	41	7.1	0.64	30	<0.25	<b>0.8</b>	0.19	3.2	88	3.7
DM28py4	1672	50	332	21	308	37	12	12	0.84	37	0.54	<b>0.81</b>	0.17	3.2	99	1.4
DM28py5	1652	25	51	87	302	20	23	10	0.23	10	<0.33	<b>0.43</b>	<0.14	0.14	21	3.0
DM28py6	3717	7.4	45	26	145	28	9.6	7.8	0.44	10	<0.30	<b>0.55</b>	<0.14	1.11	18	1.3
DM28py7	1377	7.0	36	39	803	625	4.6	8.9	0.27	7.5	<0.26	<b>0.11</b>	<0.12	0.24	25	1.0
DM28py8	2384	<0.08	12	42	2061	139	<0.65	8.9	0.14	5.9	0.26	<b>0.25</b>	<0.09	<0.01	7.8	0.78
DM28py9	2969	1.7	11	61	469	260	6.5	14	0.25	7.0	<0.24	<b>0.40</b>	<0.11	0.98	14	0.74
DM28py10	964	1.4	10	34	173	37	5.7	9.9	0.77	32	<0.34	<b>0.9</b>	0.27	4.4	58	2.2
DM28py11	886	14	105	56	741	84	15	6.6	0.43	15	<0.36	<b>0.45</b>	0.17	2.4	29	0.87
DM28py12	277	1.9	18	12	625	26	2.5	11	0.12	4.6	<0.24	<b>0.08</b>	0.15	0.13	7.7	0.39
<b>mean n=12</b>	1966	11	58	47	590	119	14	10	0.5	18	-	<b>0.6</b>	0.19	1.7	36	1.5

**Table 7:** LA-ICPMS trace element data for pyrite (continued)

<b>814m</b>	<b>As</b>	<b>V</b>	<b>Mn</b>	<b>Co</b>	<b>Ni</b>	<b>Cu</b>	<b>Zn</b>	<b>Se</b>	<b>Ag</b>	<b>Sb</b>	<b>Te</b>	<b>Au</b>	<b>Hg</b>	<b>Tl</b>	<b>Pb</b>	<b>Bi</b>
DM30py1	657	0.17	9.1	<0.06	322	11	3.6	4.3	0.54	17	<0.35	<b>0.26</b>	<0.14	2.5	48	0.30
DM30py2	48	<0.11	3.0	1.5	277	3.3	<1.7	4.4	<0.04	2.5	<0.36	<b>0.07</b>	<0.14	0.14	26	0.27
DM30py3	378	0.18	2.0	0.33	618	6.5	<0.96	4.1	0.06	17	<0.28	<b>0.08</b>	<0.14	0.09	6.6	0.60
DM30py4	2513	<0.12	8.8	14	839	14	<1.00	6.4	0.08	18	<0.32	<b>0.37</b>	<0.15	0.49	74	0.46
DM30py5	938	0.13	2.4	6.9	2104	89	1.6	6.2	0.05	19	<0.33	<b>0.06</b>	<0.15	0.08	10	0.98
DM30py6	650	0.14	8.2	2.4	1142	3.0	<0.94	6.2	0.04	0.33	<0.33	<b>&lt;0.05</b>	<0.14	0.02	0.35	0.02
DM30py7	1416	<0.11	33	6.6	411	11	2.5	5.8	0.09	6.5	<0.29	<b>0.78</b>	0.15	0.22	16	0.34
DM30py8	310	0.15	546	0.19	399	31	<0.95	5.0	0.23	21	<0.32	<b>0.35</b>	0.31	0.25	22	1.7
DM30py9	3730	1.1	10	50	1763	80	445	5.6	2.8	89	<0.28	<b>4.6</b>	0.26	9.1	255	3.1
DM30py10	6789	2.4	79	162	4589	109	15	8.5	4.0	60	<0.26	<b>2.2</b>	0.33	2.3	453	12
DM30py11	5791	1.3	25	164	5374	120	7.2	11	6.2	37	<0.33	<b>1.4</b>	0.46	5.7	277	11
DM30py12	3760	6.0	30	102	3455	87	7.4	16	3.8	35	<0.25	<b>1.3</b>	0.43	6.4	259	6.2
DM30py13	6011	5.0	90	138	4962	144	15	12	7.7	85	<0.22	<b>2.1</b>	0.48	6.1	779	29
<b>mean n=13</b>	<b>2538</b>	<b>1.6</b>	<b>65</b>	<b>54</b>	<b>2020</b>	<b>55</b>	<b>62</b>	<b>7.3</b>	<b>2.1</b>	<b>31</b>	<b>-</b>	<b>1.1</b>	<b>0.34</b>	<b>2.6</b>	<b>171</b>	<b>5.0</b>

**Table 8:** LA-ICPMS trace element data for arsenopyrite

Element	As	V	Mn	Co	Ni	Cu	Zn	Se	Ag	Sb	Te	Au	Hg	Tl	Pb	Bi
<b>689m</b>																
DM13asp1	106752	0.29	2.33	0.13	16	31	<1.01	24	<0.06	125	0.66	<b>0.72</b>	<0.18	<0.02	5.0	2.6
DM13asp2	92636	0.16	2.41	25.7	58	6.1	3.4	25	0.25	123	17	<b>2.02</b>	0.23	0.03	50	9.9
DM13asp3	110569	<0.10	1.84	15.5	190	13	4.9	36	0.70	198	48	<b>12.2</b>	0.32	0.03	126	38
DM13asp4	96356	0.17	0.78	22.1	28	1.2	1.1	31	<0.03	102	213	<b>0.13</b>	0.23	<0.01	0.86	1.10
DM13asp5	113003	2.8	13.6	16.2	177	66	26	65	1.5	140	227	<b>20</b>	<0.35	0.17	141	31
DM13asp6	108603	<0.10	2.54	9.22	176	14	4.6	48	0.96	127	27	<b>21</b>	0.17	0.06	52	19
DM13asp7	98672	0.21	474	23	195	9.3	11	37	0.80	121	101	<b>13</b>	0.26	0.07	136	20
DM13asp8	117410	0.29	240	4	78	12	10	37	0.58	154	61	<b>5.8</b>	0.30	0.08	77	18
DM13asp9	99836	2.9	182	26.1	564	55	118	41	10	290	64	<b>114</b>	0.34	0.41	342	77
DM13asp10	93468	0.13	31.3	7.6	21	3.3	2.1	14	0.13	96	3.7	<b>1.9</b>	0.19	<0.01	21	5.1
DM13asp11	31275	1.4	4.44	58.4	183	3.3	536	11	0.09	26	2.5	<b>0.94</b>	0.20	0.02	16	2.8
DM13asp12	98609	2.6	11.4	9.2	35	6.2	3.6	12	0.47	101	7.3	<b>6.9</b>	0.28	0.02	41	8.4
DM13asp13	104493	2.0	19.2	16.6	229	12	19	27	1.14	118	68	<b>8</b>	0.27	0.13	82	20
DM13asp14	97705	19	5.67	24.9	138	3.3	2.9	22	0.14	50	12	<b>1.5</b>	0.29	0.03	19	5.7
DM13asp15	104342	0.12	1.12	60.5	285	6.4	1.3	5.3	0.05	61	2.8	<b>0.25</b>	0.25	<0.02	6.8	1.5
DM13asp16	120529	2.9	51.8	272	700	43	23	12	0.55	127	9.4	<b>2.6</b>	<0.20	0.05	72	7.8
<b>mean n=16</b>	<b>99641</b>	<b>3</b>	<b>65</b>	<b>37</b>	<b>192</b>	<b>18</b>	<b>51</b>	<b>28</b>	<b>1</b>	<b>122</b>	<b>54</b>	<b>13</b>	<b>0</b>	<b>0</b>	<b>74</b>	
<b>715m</b>																
DM16aspy1	336913	0.57	3.17	246	281	18	<2.18	52	4.8	110	50	<b>75</b>	<0.14	0.14	162	27
DM16aspy2	310680	0.14	2.77	44.4	44	7.5	12	50	6.7	81	9.6	<b>124</b>	0.46	0.14	65	29
DM16aspy3	414	0.16	3.22	16.3	7640	55	1.5	7	0.04	4.1	<0.25	<b>0.12</b>	<0.11	0.02	18	2.6
DM16aspy4	260747	0.10	1.02	42.8	39	5.8	<2.02	37	<0.04	50	0.99	<b>0.63</b>	0.19	<0.01	8.5	3.2
DM16aspy5	212829	3.0	25.2	140	385	20	42	7.6	1.5	193	17	<b>13</b>	0.40	0.84	250	51
DM16aspy6	65043	3.2	7.73	1734	133	55	10	12	0.36	88	2.9	<b>8.4</b>	0.18	0.68	1006	14
DM16aspy7	14832	0.17	2.1	502	227	4.6	1.4	8.4	18	11	0.99	<b>1200</b>	0.18	0.05	29	2.4
DM16aspy8	99266	0.44	2.65	3160	969	41	2.0	15	4.1	140	19	<b>256</b>	0.53	0.18	349	33
DM16aspy9	148720	1.3	4.11	749	224	5.9	1.5	55	5.7	129	41	<b>104</b>	0.40	0.07	164	34
DM16aspy10	136800	8.0	14.6	201	171	6.2	6.5	31	0.32	78	7.9	<b>6.4</b>	0.30	0.16	110	18
DM16aspy11	122136	3.0	9.52	237	36	6.5	3.0	19	0.09	60	2.8	<b>3.3</b>	0.25	0.05	49	6.4
DM16aspy12	134328	0.54	3.97	495	349	18	3.2	27	10	234	24	<b>169</b>	0.49	0.30	186	76
<b>mean n=12</b>	<b>153559</b>	<b>2</b>	<b>7</b>	<b>631</b>	<b>875</b>	<b>20</b>	<b>8</b>	<b>27</b>	<b>5</b>	<b>98</b>	<b>16</b>	<b>163</b>	<b>0</b>	<b>0</b>	<b>200</b>	<b>25</b>

**Table 8:** LA-ICPMS trace element data for arsenopyrite (continued)

<b>739m</b>	<b>As</b>	<b>V</b>	<b>Mn</b>	<b>Co</b>	<b>Ni</b>	<b>Cu</b>	<b>Zn</b>	<b>Se</b>	<b>Ag</b>	<b>Sb</b>	<b>Te</b>	<b>Au</b>	<b>Hg</b>	<b>Tl</b>	<b>Pb</b>	<b>Bi</b>
DM18asp1	353764	65	105	77	1031	15	2.9	3.3	0.26	118	<0.150	<b>2.2</b>	0.24	0.10	60	5.3
DM18asp2	278051	179	14	16	301	62	9.5	4.7	0.32	91	<0.225	<b>2.2</b>	0.35	0.24	69	8.6
DM18asp3	317995	77	20	74	1462	4.8	1.5	3.9	0.28	121	0.20	<b>2.6</b>	0.27	0.08	61	6.5
DM18asp4	300804	63	6.6	27	362	131	3.0	6.1	3.4	218	<0.175	<b>34</b>	0.30	0.31	84	21
DM18asp5	271607	169	11	11	251	3.4	7.1	4.9	<0.03	151	0.22	<b>0.2</b>	0.35	0.11	34	7.8
DM18asp6	259190	24	6.9	16	47	5.5	3.7	3.9	0.55	117	<0.156	<b>10</b>	0.25	0.015	25	3.9
DM18asp7	193189	131	10	2869	1056	533	18	6.2	0.25	137	<0.174	<b>1.2</b>	0.30	0.28	132	7.0
DM18asp8	217268	36	20	163	962	1277	4.6	4.4	1.1	134	<0.157	<b>11</b>	0.24	0.22	122	9.3
DM18asp9	226760	6.24	6.8	854	1639	3097	11	2.6	1.8	121	<0.177	<b>18</b>	0.32	0.42	259	11
DM18asp10	177940	106	21	41	369	9.4	8.7	5.4	0.93	96	0.23	<b>12</b>	0.29	0.12	60	11
DM18asp11	217137	0.17	1.1	37	22	1.4	0.75	6.2	0.10	91	<0.150	<b>1.7</b>	0.32	<0.01	3.4	0.61
DM18asp12	197805	1.98	245	22	40	37	6.5	6.0	0.29	116	0.18	<b>3.0</b>	0.40	0.42	132	6.1
DM18asp13	193696	11	150	39	93	15	16	8.0	0.51	159	<0.179	<b>2.8</b>	0.51	0.48	239	6.0
DM18asp14	202609	16	163	362	345	148	40	14	2.6	333	1.3	<b>33</b>	0.43	0.89	341	25
DM18asp15	184028	25	21	4450	1333	650	24	25	0.26	149	7.7	<b>1.4</b>	0.29	0.17	85	4.2
DM18asp16	196679	0.11	0.92	62	8.1	1.4	<0.48	20	0.06	121	1.1	<b>0.52</b>	0.34	<0.01	1.1	0.80
DM18asp17	152296	53	51	381	104	196	41	12	1.2	178	0.38	<b>13</b>	0.34	0.46	184	9.0
DM18asp18	157112	49	28	350	221	205	22	11	1.7	256	0.49	<b>19</b>	0.41	0.49	289	17
DM18asp19	170439	0.07	1.4	336	41	14	<0.44	7.5	0.03	94	0.56	<b>1.9</b>	0.22	<0.01	2.3	0.64
DM18asp20	161416	10.0	115	55	35	35	2.7	11	0.37	154	0.46	<b>5.6</b>	0.32	0.23	155	9.3
DM18asp21	137149	21	172	111	85	108	3.3	11	0.82	251	0.68	<b>9.4</b>	0.36	0.31	157	14
DM18asp22	155551	8.9	9.5	129	56	11	5.5	10	0.11	154	0.49	<b>3.3</b>	0.28	0.05	29	4.6
DM18asp23	123708	55	53	65	86	225	29	7.8	0.60	188	0.46	<b>13.2</b>	0.34	0.16	98	12
DM18asp24	156732	0.12	1.7	27	13	2.5	<0.53	12	0.08	123	0.47	<b>2.7</b>	0.36	<0.01	5.3	1.6
<b>mean n=24</b>	<b>208455</b>	<b>46</b>	<b>51</b>	<b>441</b>	<b>415</b>	<b>283</b>	<b>12</b>	<b>9</b>	<b>1</b>	<b>153</b>	<b>1</b>	<b>8</b>	<b>0</b>	<b>0</b>	<b>109</b>	<b>8</b>
<b>740m</b>																
DM19asp1	309132	14	222	60	144	14	24	25	0.58	165	3.5	<b>14</b>	0.27	0.29	143	19
DM19asp2	252596	3.1	651	35	39	2.5	12	10	0.18	118	0.47	<b>0.81</b>	0.35	0.12	62	5.4
DM19asp3	174459	35	170	212	319	12	33	32	1.5	175	12	<b>18</b>	0.36	0.76	196	22
DM19asp4	177208	2.0	141	56	131	13	17	4.6	0.96	153	0.28	<b>15</b>	0.25	0.20	83	8.5
DM19asp5	178921	<0.10	23	31	71	17	<1.62	22	0.06	159	0.34	<b>2.2</b>	0.27	0.05	32	2.2
DM19asp6	161188	5.6	10	46	39	11	4.2	46	0.10	103	7	<b>0.92</b>	0.37	0.15	65	5.5
DM19asp7	141052	4.6	13	455	1261	21	<1.56	14	7.4	308	1.5	<b>111</b>	0.48	1.2	295	39
DM19asp8	130920	0.92	113	114	198	1.8	<1.36	13	0.14	79	1.1	<b>2.1</b>	0.30	0.04	43	5.0
DM19asp9	112315	0.19	35	32	92	6.0	3.9	12	0.70	263	<0.24	<b>19</b>	0.28	0.04	1770	14
DM19asp10	108441	0.86	18	68	153	4.7	1.7	19	0.08	146	0.77	<b>4.4</b>	0.22	0.05	192	2.1
DM19asp11	97678	1.4	231	304	412	5.7	4.4	15	0.42	164	1.1	<b>6.6</b>	0.25	0.05	78	14
<b>mean n=11</b>	<b>167628</b>	<b>7</b>	<b>148</b>	<b>129</b>	<b>260</b>	<b>10</b>	<b>12</b>	<b>19</b>	<b>1</b>	<b>167</b>	<b>3</b>	<b>18</b>	<b>0</b>	<b>0</b>	<b>269</b>	<b>12</b>

**Table 8:** LA-ICPMS trace element data for arsenopyrite (continued)

<b>780m</b>	<b>As</b>	<b>V</b>	<b>Mn</b>	<b>Co</b>	<b>Ni</b>	<b>Cu</b>	<b>Zn</b>	<b>Se</b>	<b>Ag</b>	<b>Sb</b>	<b>Te</b>	<b>Au</b>	<b>Hg</b>	<b>Tl</b>	<b>Pb</b>	<b>Bi</b>
DM23asp1	201734	3.5	6.6	4.2	41	18	31	24	0.24	123	5.4	<b>6.3</b>	0.28	0.06	63	15
DM23asp2	162095	0.34	4.4	4.9	65	23	5.5	22	0.23	99	3.6	<b>17.2</b>	0.57	0.06	95	19
DM23asp3	152635	7.5	7.7	31	25	6.6	9.6	14	0.41	109	1.98	<b>7.3</b>	0.36	0.10	48	8.3
DM23asp4	142101	0.15	1.5	162	298	13	1.3	20	0.16	122	29	<b>2.9</b>	0.26	0.04	13	7.1
DM23asp5	121696	<0.09	1.7	0.9	18	11	11	22	0.11	66	2.1	<b>13</b>	0.22	<0.01	26	6.6
DM23asp6	135542	21.8	9.1	88	1269	49	3.2	11	4.5	259	5.0	<b>111</b>	0.31	0.32	51	28
DM23asp7	33754	2.0	8.2	730	187	14	7.9	7.8	0.34	42	1.2	<b>10</b>	0.14	0.07	16	6.3
DM23asp8	113246	5.6	13	10	71	7.0	3.6	14	0.36	140	3.2	<b>7.2</b>	0.24	0.07	28	14
DM23asp9	116123	8.6	17	6.0	33	11	12	16	0.75	145	0.69	<b>13</b>	<0.18	0.11	19	5.8
DM23asp10	96343	7.4	18	70	83	14	15	7.4	2.7	145	3.2	<b>71</b>	0.22	0.25	48	9.4
DM23asp11	90922	15	16	35	92	10	9.5	12	0.33	149	2.4	<b>5.8</b>	0.26	0.17	70	17
DM23asp12	88381	0.09	1.1	<0.09	4.3	2.4	<0.57	12	0.07	74	<0.29	<b>1.9</b>	0.18	<0.01	4.8	1.9
DM23asp13	73751	<0.11	2.0	226	496	9.3	1.5	60	0.07	56	68	<b>2.2</b>	0.32	<0.02	10	3.2
<b>mean n=13</b>	<b>117563</b>	<b>7</b>	<b>8</b>	<b>114</b>	<b>206</b>	<b>14</b>	<b>9</b>	<b>19</b>	<b>1</b>	<b>118</b>	<b>10</b>	<b>21</b>	<b>0</b>	<b>0</b>	<b>38</b>	<b>11</b>
<b>781m</b>																
DM24Aasp1	127284	97	55	184	353	5514	134	7.4	3.5	143	0.42	<b>104</b>	0.22	0.29	76	17
DM24Aasp2	146941	5.9	18	77	306	7.5	24	5.5	0.36	84	<0.29	<b>3.5</b>	0.24	0.10	103	7.9
DM24Aasp3	126887	67	22	78	123	20	38	14	0.16	166	0.47	<b>3.1</b>	0.25	0.14	56	11
DM24Aasp4	127975	4.4	7.7	86	41	8.1	16	16	0.04	149	0.32	<b>0.47</b>	0.12	0.02	23	5.5
DM24Aasp5	103642	33	40	60	178	15	15	11	0.19	193	<0.32	<b>4.7</b>	0.21	0.04	27	8.1
DM24Aasp6	82322	24	28	96	147	8.5	36	15	0.06	129	0.59	<b>14</b>	0.37	0.06	29	5.1
DM24Aasp7	83810	168	35	73	541	61	64	12	0.50	134	0.50	<b>23</b>	0.23	0.17	67	6.7
DM24Aasp8	91624	14	84	126	450	10	24	9.2	0.53	153	0.47	<b>49</b>	0.34	0.15	77	13
DM24Aasp9	63989	93	61	162	1193	83	89	12	8.6	286	2.05	<b>198</b>	0.34	0.16	134	52
DM24Aasp10	74772	43	5.3	73	349	18.0	22	11	0.91	272	0.79	<b>26</b>	0.36	0.16	98	24
DM24Aasp11	52842	129	80	160	633	65	88	11	15	205	1.2	<b>298</b>	0.49	0.09	118	17
DM24Aasp12	57174	5.5	2321	219	318	51	64	8.8	1.8	140	0.66	<b>27</b>	0.47	0.11	144	16
DM24Aasp13	47830	107	68	104	294	11	81	10	0.14	117	0.53	<b>16</b>	<0.18	0.08	54	14
<b>mean n=13</b>	<b>91315</b>	<b>61</b>	<b>217</b>	<b>115</b>	<b>379</b>	<b>452</b>	<b>53</b>	<b>11</b>	<b>2</b>	<b>167</b>	<b>1</b>	<b>59</b>	<b>0</b>	<b>0</b>	<b>77</b>	<b>15</b>
<b>794m</b>																
DM26asp1	92265	0.18	1.8	16	20	12	9.3	<1.50	<0.02	22	<0.18	<b>23</b>	0.16	<0.01	1.9	47
DM26asp2	78898	28	55	171	511	104	24	4.2	1.3	61	<0.30	<b>90</b>	0.42	0.92	157	66
DM26asp3	93671	1.5	5.6	38	151	252	5.18	22	0.34	171	1.6	<b>7.4</b>	0.37	0.10	63	31
DM26asp4	77907	8.8	25	2.9	135	17	12	14	0.07	41	5.2	<b>0.35</b>	0.18	0.12	21	8.3
DM26asp5	75105	19	22	184	893	49	24	12	1.8	170	3.6	<b>40</b>	0.51	0.22	185	93
DM26asp6	66214	1.5	8.4	141	344	71	7.35	5.7	0.52	35	<0.21	<b>33</b>	0.26	0.27	73	19
DM26asp7	58069	0.39	5.1	37	161	75414	199	<2.02	1.0	54	<0.30	<b>25</b>	0.34	1.6	156	51
DM26asp8	53086	21	29	302	605	647	77	19	1.1	97	20	<b>20</b>	0.26	0.42	119	29
DM26asp9	52414	8.3	17	11	32	4.6	8.1	11	0.03	34	0.79	<b>0.21</b>	0.31	0.02	23	4.0
DM26asp10	44760	0.16	4.8	68	666	15100	18	17	1.0	171	8.5	<b>2.5</b>	0.43	2.23	436	23
DM26asp11	47849	4.1	15	33	315	1798	11	12	0.94	145	7.6	<b>20</b>	0.36	0.43	98	9.0
DM26asp12	44061	1.7	7.2	209	739	1533	16	7.1	0.19	131	1.8	<b>1.1</b>	0.34	0.28	46	7.3
DM26asp13	38669	0.80	4.9	158	583	24772	13	2.4	216	90	0.37	<b>4464</b>	0.66	1.5	205	74
DM26asp14	39083	0.13	1.9	8.7	76	2394	4.46	18	0.18	52	23	<b>1.2</b>	0.18	0.16	33	7.5
<b>mean n=14</b>	<b>61575</b>	<b>7</b>	<b>15</b>	<b>98</b>	<b>373</b>	<b>8726</b>	<b>31</b>	<b>12</b>	<b>17</b>	<b>91</b>	<b>7</b>	<b>338</b>	<b>0</b>	<b>1</b>	<b>115</b>	<b>33</b>

**Table 8:** LA-ICPMS trace element data for arsenopyrite (continued)

855m	As	V	Mn	Co	Ni	Cu	Zn	Se	Ag	Sb	Te	Au	Hg	Tl	Pb	Bi
DM37asp1	99115	154	38	82	857	11	18	7.2	0.34	88	0.73	<b>6.0</b>	<0.17	0.19	54	3.7
DM37asp2	142599	28	12	25	118	3.4	6.53	4.4	0.10	121	<0.28	<b>3.1</b>	0.18	0.077	34	3.4
DM37asp3	141134	0.44	1.9	15	109	5.8	26	13	0.35	162	0.57	<b>1.8</b>	0.17	0.37	60	4.1
DM37asp4	107976	104	40	174	1212	7.5	34	21	1.8	210	95	<b>27</b>	0.26	0.37	117	22
DM37asp5	130346	7.5	475	19	130	12	14	17	0.65	150	6.4	<b>4.6</b>	0.37	0.64	83	19
DM37asp6	116666	1.2	2.0	27	119	2.2	1.3	13	0.13	155	0.91	<b>1.7</b>	0.23	0.08	24	4.6
DM37asp7	79175	80	30	16	94	4.2	10	8.2	0.26	118	0.58	<b>1.9</b>	0.31	0.32	69	5.8
DM37asp8	97335	0.81	70	13	131	3.5	6.0	8.7	0.24	142	0.34	<b>3.3</b>	0.27	0.14	53	3.4
DM37asp9	86860	3.2	62	43	302	5.0	9.6	5.7	0.21	232	0.64	<b>0.92</b>	0.19	0.17	47	2.8
DM37asp10	88070	0.18	46	17	163	3.0	4.3	9.0	0.30	175	1.1	<b>2.1</b>	0.19	0.09	40	5.3
DM37asp11	87632	2.9	618	42	224	11	16	9.6	0.24	155	1.2	<b>3.5</b>	0.26	0.33	61	6.6
DM37asp12	56136	117	1712	32	206	9.9	31	11	19	153	<0.87	<b>297</b>	<0.30	0.64	78	11
DM37asp13	52752	110	61	33	198	21	43	4.8	2.3	110	1.3	<b>36</b>	0.33	0.59	63	9.7
DM37asp14	66762	1.28	31	28	285	18	18	8.0	1.3	191	1.7	<b>4.7</b>	0.55	1.6	225	13
<b>mean n=14</b>	<b>96611</b>	<b>44</b>	<b>228</b>	<b>40</b>	<b>296</b>	<b>8</b>	<b>17</b>	<b>10</b>	<b>2</b>	<b>154</b>	<b>9</b>	<b>28</b>	<b>0</b>	<b>0</b>	<b>72</b>	<b>8</b>
<b>858m</b>																
DM38asp1	151463	116	7.0	206	252	5.9	13	28	0.20	59	1.7	<b>0.49</b>	0.35	0.15	26	5.6
DM38asp2	145320	48	15	104	870	21	14	4.7	10	134	1.0	<b>107</b>	0.46	0.34	130	9.8
DM38asp3	117929	118	45	338	854	23	46	16	5.1	96	1.2	<b>54</b>	0.46	0.10	74	5.8
DM38asp4	104265	150	31	75	741	17	49	6.8	9.6	291	14	<b>67</b>	0.43	0.35	165	25
DM38asp5	98993	76	28	45	141	9.8	6.8	26	0.47	90	1.3	<b>5.4</b>	0.33	0.12	95	5.9
DM38asp6	99959	81	26	170	2500	41	16	9.3	41	435	4.6	<b>339</b>	0.77	1.7	442	37
DM38asp7	94089	0.19	1.8	2.7	432	2.2	<0.57	16	0.09	48	25	<b>0.55</b>	0.32	<0.01	7.6	2.2
DM38asp8	104579	7.8	8.5	38	487	8.1	6.5	7.5	0.23	69	1.2	<b>0.53</b>	0.33	0.40	81	4.9
DM38asp9	61429	126	40	75	559	8.3	33.7	7.6	6.7	131	9.9	<b>67</b>	0.33	0.14	80	8.5
DM38asp10	44238	42	69	313	2679	76	59.0	5.7	37	155	1.4	<b>227</b>	0.28	0.16	389	10.0
DM38asp11	70829	27	15	52	260	5.4	7	9.9	2.4	97	0.74	<b>31</b>	0.46	0.16	99	7.9
DM38asp12	59894	30	9.5	92	501	3.8	7	15	0.24	45	0.20	<b>0.73</b>	0.28	0.07	45	2.4
<b>mean n=12</b>	<b>96082</b>	<b>68</b>	<b>25</b>	<b>126</b>	<b>856</b>	<b>18</b>	<b>23</b>	<b>13</b>	<b>9</b>	<b>138</b>	<b>5</b>	<b>75</b>	<b>0</b>	<b>0</b>	<b>136</b>	<b>10</b>
<b>864m</b>																
DM41asp1	104404	16	27	91	336	14	10	6.2	1.3	216	0.49	<b>4.7</b>	0.47	1.0	134	10
DM41asp2	104839	4.2	11	8.6	34	7.6	5.5	7.4	0.15	89	0.52	<b>1.8</b>	0.25	0.21	29	3.8
DM41asp3	120155	36	38	231	183	6.7	25.8	9.6	1.4	171	0.66	<b>101</b>	0.4	0.42	76	11
DM41asp4	106762	39	37	167	432	19	52.7	13	2.9	316	2.8	<b>23</b>	0.47	1.0	204	21
DM41asp5	112682	0.16	1.7	5.5	12	5.5	3.8	16	0.08	76	1.4	<b>1.25</b>	0.27	-	12	3.6
DM41asp6	111551	22	26	48	127	8.3	10	7.9	0.15	142	<0.25	<b>1.7</b>	0.34	0.11	26	2.5
DM41asp7	85580	89	69	33	109	14	37	5.1	0.40	128	0.49	<b>3.0</b>	0.32	0.31	50	4.3
DM41asp8	112282	14	32	32	103	11	16	8.5	0.76	142	0.72	<b>5.1</b>	0.17	0.22	88	12
DM41asp9	131167	1.6	21	87	245	17	33	10	0.98	176	0.74	<b>6.1</b>	0.29	0.43	75	13
DM41asp10	134491	11	10	72	23	2.6	7.6	17	0.05	47	<0.242	<b>0.49</b>	0.40	-	11	3.7
DM41asp11	109500	0.32	4.7	8.9	68	6.9	19	7.2	0.09	210	<0.25	<b>0.52</b>	0.36	0.12	15	3.0
DM41asp12	103973	25	21	82	174	6.5	181	6.9	0.77	158	0.50	<b>16</b>	0.43	0.21	74	15
<b>mean n=12</b>	<b>111449</b>	<b>21</b>	<b>25</b>	<b>72</b>	<b>154</b>	<b>10</b>	<b>33</b>	<b>10</b>	<b>1</b>	<b>156</b>	<b>1</b>	<b>14</b>	<b>0</b>	<b>0</b>	<b>66</b>	<b>9</b>